MASTER

# Magnetically-induced deflections of flexible magnetic thin films a novel technique for magnetic field sensing

van Hoorn, K.

*Award date:*
2020

Department of Applied Physics
Physics of Nanostructures

# Magnetically-induced deflections of flexible magnetic thin films

*A novel technique for magnetic field sensing*

Kelvin van Hoorn

Master Thesis

**Supervisors:**
dr. ir. R. Lavrijsen
dr. ir. C. van der Avoort

Eindhoven, January 2020

# Abstract

The continuous miniaturisation of devices by the semiconductor industry challenges modern system control, which, together with the augmented sensing capabilities of the automotive and mobile sectors, has lead to an increased demand for smaller and better sensors. Magnetic field sensors in specific are crucial to the improvement of system control, as they can e.g. indirectly measure electric currents in a control circuit. A new approach in magnetic field sensing is investigated in the form of flexible magnetic thin films, which is an underused and rarely studied topic.

This work describes exploratory research on how flexible magnetic thin films deflect in the presence of a uniform magnetic field, for later use as magnetic field sensors. The magnetically-induced deflections of the film are modelled using both numerical torque simulations and finite-element models based on the Stoner–Wohlfarth model and Maxwell stress. The quality of these models is confirmed through measurements of a magnetic $Co_{80\%}B_{20\%}$ thin film deposited on a flexible membrane sensor, as provided by AMS Netherlands. The state of the art capacitive pressure sensor of AMS is used as the foundation on which magnetic films are investigated. The sensor provides both a suspended flexible membrane, which is used as substrate for the magnetic film, and a digital readout, which is used to measure effective deflections of the membrane and magnetic film. It is found that flexible magnetic films are well described by the torque and finite-element models, and magnetically-induced deflections up to 4.5 nm are measured on 175 nm thick $Co_{80\%}B_{20\%}$ films.

The potential of flexible magnetic films as magnetic field sensors is gauged by measuring the smallest resolvable magnetic field change, which was found to be 0.6 mT. This is an impressive result, for commercial sensors of a similar size and price obtain magnetic resolutions between 0.2 $\mu$T and 0.5 mT [1–5]. This indicates that, with further optimisation, flexible magnetic thin films can be brought to a commercial level. Moreover, flexible magnetic films would have the advantage that they can operate on a range of hundreds of mT, while the cited sensors only operate on a range of tens of mT at best.

# Contents

# 1
# Introduction

The increasing demand for device miniaturisation of the semiconductor industry goes hand in hand with an increasing demand for better system control of manufacturing machines. An important part of system control is the wide array of employed sensors, which give necessary feedback on the processes of the machine. High quality current sensors in specific, are crucial to the improvement of manufacturing machines. It is imperative to come up with new sensors that are non-intrusive, exhibit better resolution, operate on a wider dynamic range, have faster response times, and work at higher frequencies.

This work investigates the innovative use of flexible magnetic thin films as magnetic field sensors, a preliminary step into non-intrusive current sensing. Non-intrusive current sensors measure the current indirectly, utilising the magnetic Oersted fields that are generated by current wires. It is thus important for the creation of high quality current sensors, to first create high quality magnetic field sensors, also known as magnetometers. The use of flexible magnetic thin films is mostly unexplored territory [6, 7], for magnetic films are usually fabricated on rigid substrates. As such, this work will focus on how suspended flexible magnetic thin films are deformed in external magnetic fields, for later use as a magnetic field sensor.

The project is in collaboration with AMS Netherlands, who create state of the art sensors for the mobile and automotive industry [8]. The flexible magnetic thin films are deposited on the capacitive pressure sensor of AMS, in order to measure magnetically-induced deflections of the thin film. As a result, the capacitive pressure sensor is functionalised to be a magnetic field sensor. A short introduction is given on the flexible magnetic thin film, the capacitive pressure sensor and how it operates as magnetic field sensor, and what was previously known for flexible magnetic thin films. Finally, a short section is dedicated to the structure of this thesis.

## 1.1 Suspended flexible magnetic thin films

The aim of this work is to investigate flexible magnetic thin films, for the purpose of creating a new kind of magnetic field sensor. But what are flexible magnetic films exactly? And how can they be used as a magnetic field sensor? Quite simply, a flexible magnetic film, is a film with magnetic properties and is capable of bending easily without breaking. In practice, this will be realised by depositing a thin magnetic layer upon a suspended flexible membrane, provided by the capacitive pressure

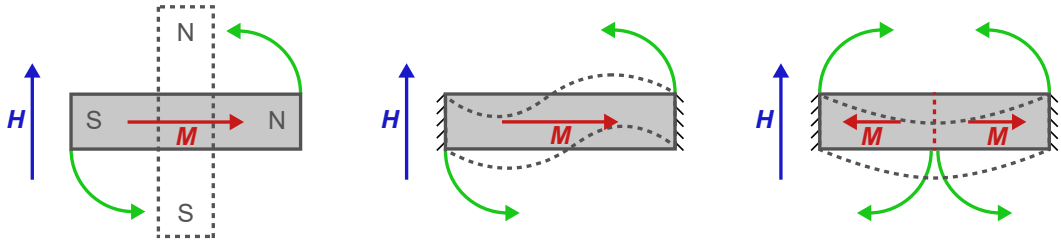


Figure 1.1: Illustrations of the effect of torque on a bar magnet or suspended flexible magnetic film. The green arrows denote the rotation due to torque, $H$ the external field, $M$ the magnetisation, and the dashed-lines denote the resulting deformation. For the bar magnet, the typical North and South pole are indicated by N and S respectively. (a) An example of how a typical bar magnet is rotated in an external field. (b) Anti-symmetric deformation of a suspended flexible magnetic thin film, with a single magnetisation direction. (c) Symmetric deformation of a suspended flexible magnetic thin film, with the magnetisation mirrored around the centre.

sensor of AMS. Because the magnetic film is relatively thin, on the order of tens of nanometers, the mechanical properties are mainly determined by the microns thick flexible membrane, which allows the study of flexible magnetic films.

The question remains, how can flexible magnetic thin films be utilised as magnetic field sensors? Despite that there has not been much research on flexible magnetic films, it is known that the magnetisation of a magnetic material experiences a torque in the presence of an external magnetic field. The torque, in combination with magnetic anisotropy, leads to mechanical rotations and deformations of a magnetic material [9]. This is demonstrated in Figure 1.1, where the first figure shows a typical bar magnet rotating due to torque, such that the magnetisation $M$ and external field $H$ are aligned. The other figures depict how the torque could deform a suspended flexible magnetic film. Figure 1.1b shows the simple case of a single magnetisation direction, which results in an anti-symmetric deformation of the suspended film. The maximum deflection of the film is weakened by the anti-symmetric deformation. For the purposes of a magnetic field sensor, the symmetric deformation of Figure 1.1c is more interesting, because the deflection is larger. To gain this symmetric deflection, the magnetisation direction needs to be mirrored around the centre of the film, which will be achieved by exploiting the shape-induced magnetic anisotropy of a bent film. It will be these deformations, as function of magnetic field, that are measured by the sensor. Note that a magnetic film also experiences a force from gradients in the external magnetic field. However, theoretical calculations presented in sections 2.3.1 and 2.3.2 show that the expected deflection from a torque is much greater, which is why torque is the preferred interaction to investigate in this work.

It is thus proposed, that flexible magnetic films can be used as indirect magnetic field sensors, where the deflection of the magnetic film as function of the external magnetic field is measured. This work focusses on how flexible magnetic thin films are deflected in the presence of external magnetic fields, and how this can be optimised for the purpose of an indirect magnetic field sensor. To this end, the

magnetically-induced deflection is measured and compared to numerical and finite-element models, based on the torque, Stoner–Wohlfarth model, and Maxwell stress.

In this thesis a ferromagnetic alloy of cobalt (Co) and boron (B) is used for the magnetic thin film. The composition of the alloy is $Co_{80\%}B_{20\%}$, from now on simply referred to as CoB. This alloy is chosen for its high magnetic saturation, lack of crystalline anisotropy and availability for sputter deposition in the lab. These are favourable properties for the magnetically-induced deflections, as will become clear in Chapter 2, with further motivation for the material given in Section 3.1.2.

## 1.2 Measuring deflection with capacitive pressure sensors

The magnetically-induced deflections of the previous section are estimated to be on the order of a few picometers up to a few nanometers, which are minuscule deflections. For comparison, the average distance between atoms is on the order of 100 picometers. The deflections are in fact so small, that it is hard to measure it with common profilometer methods, like atomic force microscopy or reflected light interferometry. This is where the capacitive pressure sensor of AMS comes in, for it provides a flexible substrate to deposit on, as well as a method to indirectly measure effective deflections of a few picometers.

Capacitive pressure sensors are pressure sensors, which output a pressure by measuring a capacitance. The basic principle behind capacitive pressure sensors is the well known parallel plate capacitor. However, instead of having two "plates" one of them is a flexible membrane. Figure 1.2 shows a 3D model and microscope image of the used capacitive pressure sensor, which consists of two parallel "plate" capacitors of which the membranes are shown in grey. The parallel "plate" capacitor is shown in the cross-section of figures 1.2c and 1.2d. It consists of two electrodes, shown in red and blue, where the top electrode is a membrane. The membrane is deformed due to a pressure difference between the ambient pressure and the cavity pressure, resulting in a change of capacitance. Through calibration this capacitance change is translated back into a pressure change, which is the output of the sensor. Similarly, changes in the pressure can be calibrated to changes of the effective deflection of the membrane. It is called the "effective" deflection because it is derived from the capacitance, which is integrated over the entire membrane, and calibrated by a mid-point deflection measurement. Through these conversions the sensor can measure an astounding minimal effective deflection change on the order of a few picometers. It should thus be possible to measure magnetically-induced deflections on a capacitive pressure sensor with a magnetic thin film.

The membranes used in this work are $700 \times 175$ $\mu m^2$, with added magnetic CoB films that are on the order of 100 nanometers thick. The size of the sensor is thus similar to that of MEMS. The quality of the sensor as a magnetic field sensor will be quantified by the magnetic resolution, which is defined as the smallest resolvable magnetic field change. For this specific kind of sensor this would be determined by the minimum magnetic field change that results in a resolvable effective deflection

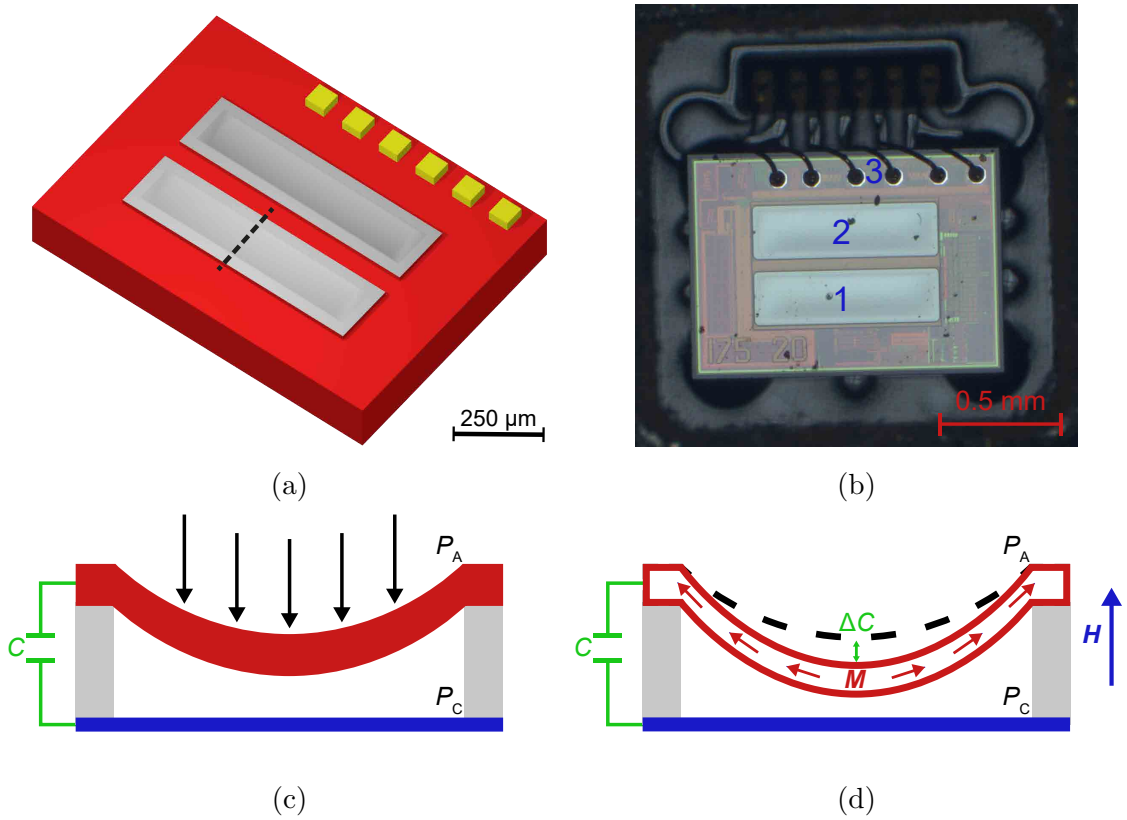


Figure 1.2: (a) 3D model of the capacitive pressure sensor, with two membranes in grey and six gold bond pads. (b) Microscope image of the capacitive pressure sensor from above, with two membranes (1, 2) and six gold bond pads (3). (c) Cross-section of the sensor along the dashed line of (a). The red line denotes the flexible membrane, which together with the blue bottom forms a parallel plate capacitor. Due to the pressure difference between the ambient pressure ($P_A$) and cavity pressure ($P_C$) the membrane is pushed inwards, increasing the capacitance. (d) Cross-section of the sensor, where the magnetically-induced deflection is measured as an additional capacitance change $\Delta C$. Note that the deflection due to the magnetic field $\boldsymbol{H}$ is strongly exaggerated.

change. The optimal sensor of this work is able to achieve sub-milliTesla resolutions, which is of the same order as commercially available sensor within the same size and price categories [1–5].

## 1.3 Exploratory research on flexible magnetic films

In the previous sections it was introduced that flexible magnetic thin films can be deflected through external magnetic fields and that these deflections can be measured on the capacitive pressure sensor of AMS Netherlands. However, only few studies are done on flexible magnetic films, moreover these are studies using patterned micrometer sized magnets, not full-sheet films as discussed in Section 1.1 and used in this study. The few studies that were found [6, 7] use a design of a few micron thick polydimethylsiloxane (PDMS) membrane, in which they embed

Permalloy flaps that can be up to 22 $\mu$m thick. The design of M. Khoo and C. Liu is illustrated in Figure 1.3. This design is not only used as a magnetic field sensor but also for the purpose of creating a microfluidic pump.

Unfortunately both reports are predominantly phenomenological, with only really stating that a magnetic membrane deflects in the presence of a permanent magnet. H. Chang et al. report deflections up to 140 $\mu$m, which are much greater than the nanometer deflections that are measured in this project due to the large volume of magnetic material used, increasing the total torque which can be applied. It is, however, hard to compare these deflections because the membrane materials and overall design are very different. Besides, it is hard to attribute what part of the magnetic field causes the deflection, because permanent magnets do not really produce a uniform magnetic field. The reports leave a lot of questions open that are important when you want to use a flexible magnet as a magnetic field sensor. The most important question which is not discussed is, what the relation is between the deflection and the magnetic field. M. Khoo and C. Liu state that the deflection increases with the magnetic field strength and that it is caused by torque, but it is not argued how the deflection increases or if the deflection increases indefinitely with the magnetic field strength. What follows is a set of follow-up questions that will be treated in this work.

**How does the deflection depend on the angle of the magnetic field?**
Both reports make no statements about how the deflection depends on the field angle, nor is it stated under what angle the field is applied, though Figure 1.3 suggests that M. Khoo and C. Liu apply the magnetic field under a slight angle with respect to the flat membrane. In the theory chapter it will become clear that the angle between the magnetization of the magnet and the applied magnetic field, (note that this is not per definition the angle between the physical orientation of the magnet and the applied magnetic field) is of great importance to the torque and deflection of full-sheet flexible magnetic films. Most importantly, it is hypothesised that the deflection is greatly enhanced for perpendicular magnetic fields, which is later acknowledged in modelling and measurements of the flexible magnetic film.

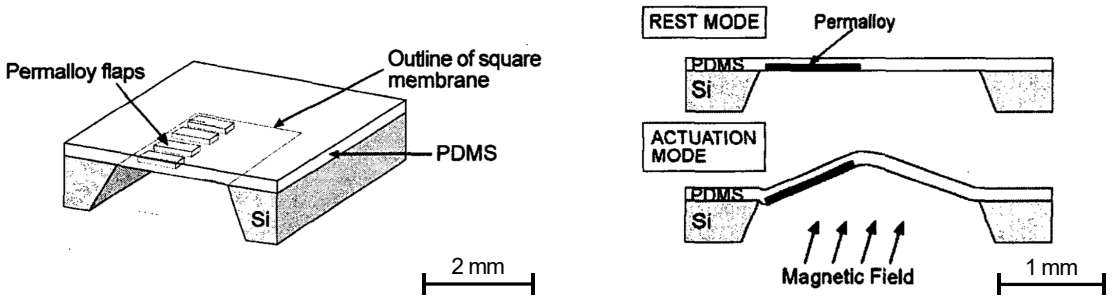


(a) (b)

Figure 1.3: Images of the membranes with patterned micrometer sized magnets, adapted from M. Khoo and C. Liu [6]. (a) Overview of the PDMS membrane with Permalloy flaps. (b) Schematic of the membrane in the absence of a magnetic field (rest mode) and with an applied magnetic field (actuation mode).

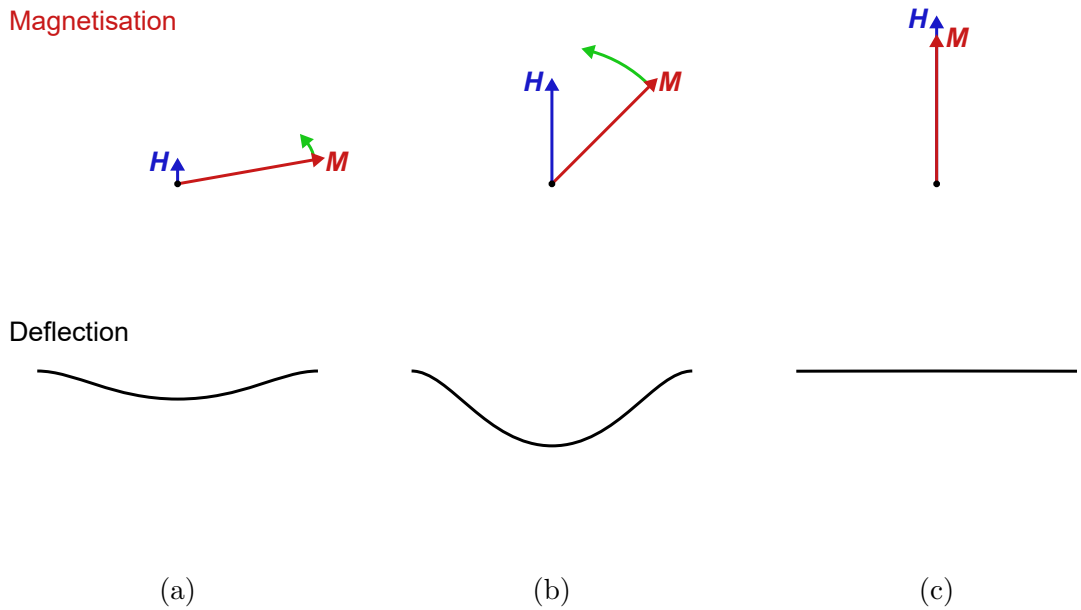


(a) (b) (c)

Figure 1.4: Depiction of the magnetisation ($\boldsymbol{M}$) aligning with an increasing external magnetic field ($\boldsymbol{H}$) through torque. The black lines denote the corresponding induced deflection of the flexible magnetic film. (a) Low magnetic field, only slightly rotating $\boldsymbol{M}$ and generating a small torque, resulting in a small deflection. (b) Medium magnetic field, generating a large rotation and torque, resulting in a strong deflection. (c) The magnetic field has surpassed the anisotropy field, causing $\boldsymbol{M}$ to be completely aligned with $\boldsymbol{H}$ and no longer generating any torque or deflection.

**What is the relation between the deflection and the magnetic field strength?**
M. Khoo and C. Liu only state that the deflection increases with the magnetic field strength, due to the generated torque. However, theory suggests that the torque drops when the magnetic field strength surpasses the anisotropy field, as the magnetisation of the material will simply align along the magnetic field and thus no torque would be exerted. Figure 1.4 illustrates this behaviour. This relation is confirmed in the models and measurements, which indeed show a drop of the deflection when the magnetisation aligns. This inherently limits the field strengths that can be measured by a flexible magnetic film to the anisotropy field, which in this study is strongly related to the saturation magnetisation that is on the order of 1 T for the investigated CoB film.

**How does the magnetic layer thickness influence the deflection?**
The magnetic layer thickness can influence the deflection in multiple ways. On the one hand, from theory it is known that torque grows linearly with the volume of the magnetic material, increasing the deflection. On the other hand, the stiffness of the flexible membrane will increase as a thicker stiff magnetic layer is added, decreasing the deflection per torque. The resulting relation is investigated in a systematic study of the stiffness and deflection for varying CoB layer thicknesses.

**What is the best configuration, in order to use the flexible magnetic film as a magnetic field sensor?**
The original purpose of this project was to create a magnetic field sensor, and thus this work does not only describe the flexible magnetic films, but also gives an approximation of the magnetic resolution that is achieved with the fabricated sensors. Moreover, the best configuration of the magnetic field and magnetic layer thickness are discussed, which is the result of the previous three questions.

By the end of this section it should be clear that, prior to this work, there was nearly no literature on flexible magnetic films. The focus of this thesis will thus be on expanding the knowledge of flexible magnetic films. This is done through modelling flexible magnetic films, based on the theory for magnetic torque, the Stoner–Wohlfarth model and the Maxwell stress. The quality of the model is verified through measurements of the effective deflection, which are done on the capacitive pressure sensor with a magnetic CoB layer. Finally, this knowledge is used to determine the optimal magnetic resolution of the fabricated devices.

## 1.4 This thesis

In this thesis, an extensive study on how flexible magnetic thin films deflect in magnetic fields is presented. The purpose of this is to both understand the deformations of flexible magnetic thin films and explore new techniques for magnetic field sensing.

A complete and easy to understand overview of the relevant theoretical concepts is presented in Chapter 2. Chapter 3 outlines the methods used in fabricating the flexible magnetic film, and the different measurement set-ups that are used in this work. The flexible magnetic thin film is modelled in Chapter 4, using both numerical and finite-element models. The measurement and modelling results are compared and discussed in Chapter 5. There the quality of the model is confirmed and the ultimately achieved effective deflection of 4.5 nm and magnetic resolution of 0.6 mT is measured. Finally, a concise conclusion of this work is given in Chapter 6, and an outlook on further studies and possible improvements is given in Chapter 7.

# 2
# Theory

The aim of this chapter is to present an easy to understand and complete overview of the theory, which is used for modelling and interpreting magnetically-induced deflections of flexible magnetic thin films. The first section describes the working principle of the capacitive pressure sensor, and how the measured capacitance is converted to pressure and into the effective deflection. The second section introduces the Stoner–Wohlfarth model, which is the basis used for modelling the magnetic state of the film on top of the flexible membrane. The third and final section will address how the magnetic state will induce mechanical forces on the film, that result in an effective deflection of the film, the key-observable in this study.

## 2.1 Working principle of the capacitive pressure sensor

Capacitive pressure sensors are pressure sensors, that as the name suggests measure a capacitance, which is converted to a pressure reading. They are commonly used for mobile devices because of their small size, low power consumption and relatively low temperature dependence compared to other methods [10]. The sensor is illustrated in Figure 2.1 and is based on the common parallel plate capacitor, where the capacitance is dependent on the area of the plates and the distance between them. Two alterations are made to utilise this principle as a pressure sensor. First of all the two electrodes are encased by walls, making an airtight cavity in between the two plates. Because of this, the cavity pressure and the ambient pressure can be different, such that a force is exerted on one of the electrodes. The second change is that one of the electrodes is a flexible membrane that can deform by mechanical forces. Together this means that one of the electrodes is pushed inwards when the ambient pressure is higher than the cavity pressure, which results in a pressure-dependent capacitance. Because the pressure sensor was meant for measuring pressures near atmospheric pressure, the cavity pressure is lowered to a slight vacuum of approximately 10 mbar. As such the membrane is pushed inwards at atmospheric pressures. Note that the membrane along the long-axis has a large flat part, as illustrated in Figure 2.1c. This is expected because the deflection is hampered by the short-axis of the membrane. The result of this is a bathtub-like deflection profile of the membrane due to the ambient pressure.

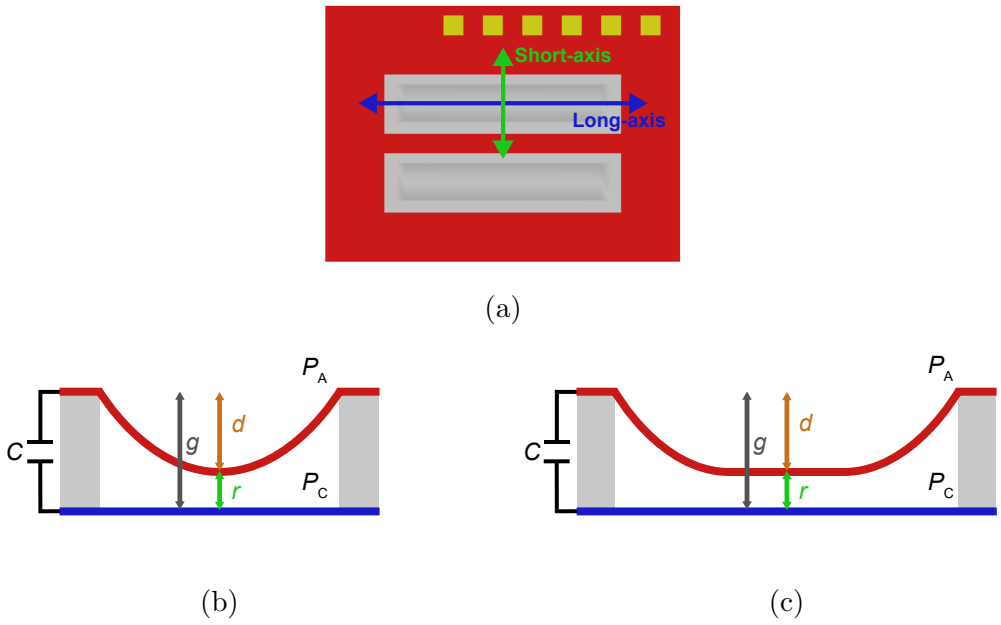


Figure 2.1: Cross-sections of the cavity, with $C$ the capacitance, $g$ the cavity gap, $r$ the distance between the electrodes, $d$ the deflection, $P_A$ the ambient pressure and $P_C$ the cavity pressure. The top electrodes are deflected under the condition $P_A > P_C$. (a) Definition of the short- and long-axis of the membranes. (b) Cross-section along the short-axis of the membrane. (c) Cross-section along the long-axis of the membrane. Note that the deflection along the long-axis is hampered by the short-axis, resulting in a bathtub-like shape.

Due to the fact that one electrode is flexible, the distance between the two electrodes is no longer uniform. To determine the capacitance between the electrodes the integral form for capacitance is used,

$$C = \epsilon \int \frac{1}{r(x,y)} dA. \tag{2.1}$$

In this description $\epsilon$ is the permittivity, $r(x,y)$ the distance between the electrodes as function of position, and the integration is done over the surface area $A$ of the electrodes. Note that the capacitance scales as $1/r$. Hence, the capacitance is dominated by the areas where the gap is the smallest. This is important, for anti-symmetric deflections can still contribute to a net capacitance change. Anti-symmetric deflections are expected for certain magnetic field angles, as was introduced in Section 1.1 and is detailed in Section 2.3.1.

The sensor outputs a pressure value, which is derived from the capacitance by calibration of the sensor. Figure 2.2 displays the relations between the capacitance, the distance $r$ and the ambient pressure. The relation between $r$ and pressure can be summarised as Hooke's law, where the membrane is generalised as a spring. The spring is pushed inwards by the force from the pressure load. This results in the expected linear behaviour between distance $r$ and pressure, when the pressure increases the gap decreases. The calibration is done by measuring the output capacitance while controlling the ambient pressure. The ambient pressure is set out against an actual measurement of capacitance in Figure 2.2d. The data is fitted

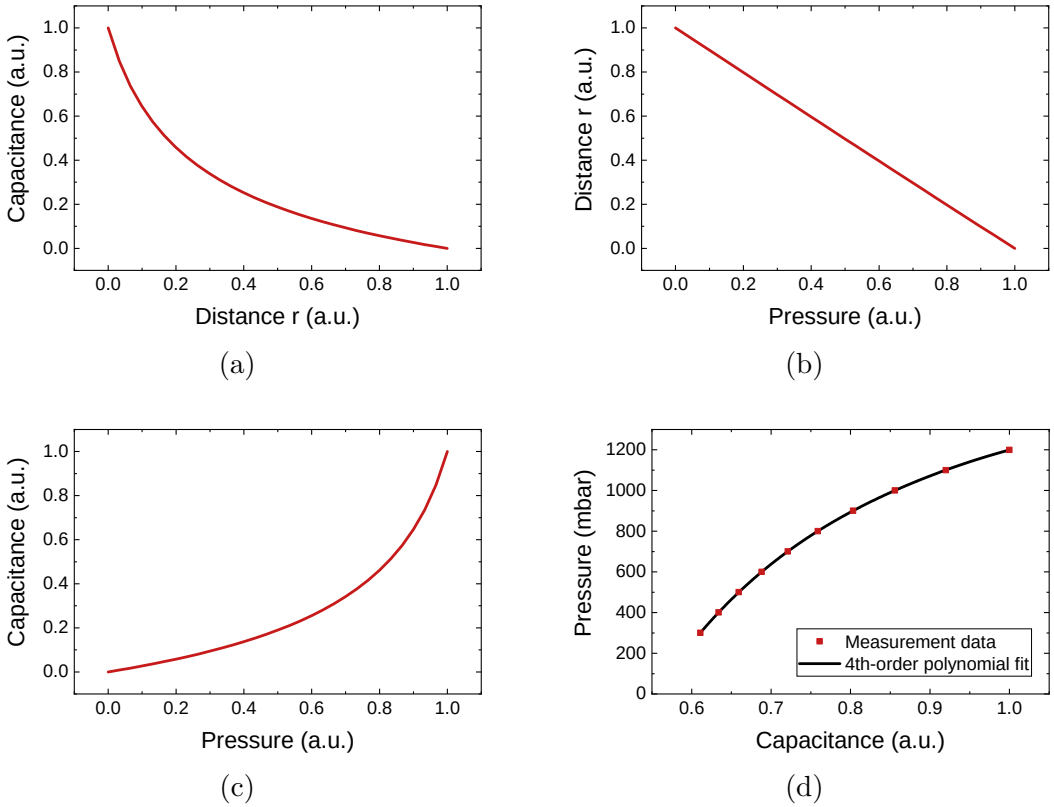


Figure 2.2: (a) Graph showing the reciprocal relation between the capacitance and the distance between the midpoint of the two electrodes. (b) The linear relation between pressure and the distance $r$. (c) Capacitance readout as function of pressure. (d) Measurement data of the set pressure as function of capacitance, and a fourth-order polynomial fit which is used to convert the capacitance readout to pressure.

by a fourth-order polynomial, which is used to convert the capacitance readout to pressure. A fourth-order polynomial is sufficient, as the unexplained variance of the model fit, at atmospheric pressure, is lower than the sensor's smallest resolvable pressure change of approximately 1 Pa.

In the end, the pressure sensor is used to measure magnetically-induced deflections of the membrane. Similar to the linear relation between distance r and the pressure, the relation between the deflection $d$ and the pressure is linear. The deflection can simply be expressed as $d = g - r$, where $g$ is the cavity gap. When the pressure increases, the deflection increases linearly as denoted by Hooke's law. The linear relation can be expressed by a single conversion factor, which converts the output pressure to the effective deflection. This conversion factor will be determined by measuring the deflection profile of the membrane at atmospheric pressure, as will be further discussed in sections 3.2.3 and 5.1.1. With this conversion the effective deflection can be measured, which can originate from both the pressure and the magnetically-induced forces on the membrane. In the analysis of the measurements, the effective deflection due to pressure will be subtracted from the data, such that only the magnetically-induced effective deflection is shown.

## 2.2 Magnetisation orientation in magnetic thin films

In this work, a magnetic thin film is deposited on top of the capacitive pressure sensor to investigate magnetically-induced deflections, for use as a magnetic field sensor. This section introduces the theory of the magnetisation behaviour of the thin film on top of the membrane, which is modelled by a discretised Stoner–Wohlfarth model, based on the Zeeman effect and magnetic anisotropy. This specific model is chosen for its ability to model the coherent rotations of magnetisation on a macro-spin level. In the end, the magnetic state will determine the magnetically-induced deflections that are described in Section 2.3. The Zeeman effect and magnetic anisotropy are introduced in the first two subsections, culminating in the total magnetic energy density of the system that is described by the Stoner–Wohlfarth model in the final subsection.

Note that, to improve the readability, the values of the external field $H$ and magnetisation $M$ are always given in units of Tesla. This is simply a conversion from the proper values in units of A/m to T, by multiplying it by the vacuum permeability $\mu_0$. This is done consistently throughout this work.

### 2.2.1 Zeeman effect

The Zeeman energy density is derived from the Zeeman effect, which was originally discovered in 1896 by Pieter Zeeman [11, 12]. The effect states that a magnetic entity prefers to align itself parallel to an externally applied magnetic field. For ferromagnets, that are investigated in this work, this can be extended to the statement that the magnetisation $\boldsymbol{M}$ prefers to align itself to the external field $\boldsymbol{H}$. This can be expressed in terms of an energy density, the Zeeman energy density:

$$E_Z = -\mu_0 \boldsymbol{H} \cdot \boldsymbol{M}. \tag{2.2}$$

In this description $\mu_0$ is the permeability of vacuum. The equation states that, when the magnetisation and an external field are parallel the energy will be its negative maximum. This is the lowest, and thus most preferable, energy state in which the magnetisation state is bound to the external field. In other words, work must be done to rotate the magnetisation away from the external field. In the model, the Zeeman energy will try to align the magnetisation of the film along the externally applied magnetic field, but needs to compete with the anisotropy energy that is discussed in the next part.

### 2.2.2 Magnetic anisotropy

Anisotropy is the phenomenon of having a spatial direction preference. Magnetised materials can be anisotropic, which means that the magnetisation prefers to align itself along a specific direction. For a simple uniaxial magnet this direction is called the easy-axis, for it is easy to align the magnetisation along this axis. The connection between the magnetisation and a spatial direction is essential to deform the film through magnetic effects, which are discussed later in this chapter.

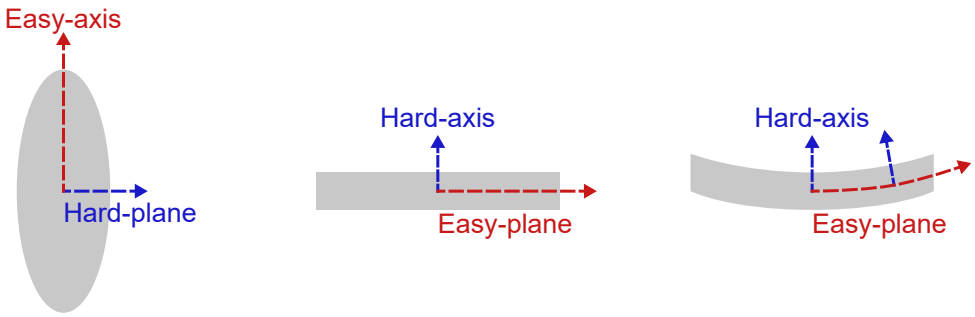


(a) (b) (c)

Figure 2.3: Illustrations depicting the anisotropic easy- and hard-axis, or -plane, for common shapes. (a) Ellipsoid with an easy-axis and hard-plane. (b) A thin film with an easy-plane and hard-axis. (c) Example of the membrane, which is a bent thin film. It still has an easy-plane and hard-axis, however these change with the bending of the film.

In most cases a magnetic material exhibits a single easy-axis, also called uniaxial anisotropy. Alongside an easy-axis there is often a hard-axis, which is unfavourable to align with and is usually perpendicular to the easy-axis. The energy density associated with uniaxial anisotropy is expressed by the angle $\theta$ between the magnetisation and the easy-axis, and the anisotropy constant $K$:

$$E_a = K \sin^2(\theta). \tag{2.3}$$

With $K$ being positive, it is clear that the energy is minimised when $\theta = 0°$, where the magnetisation is aligned with the easy-axis. It is also clear that at $\theta = 90°$ the energy cost is the highest, i.e. a hard-axis.

In magnetic materials anisotropy can originate from different properties, such as the physical shape of the magnet, the crystalline structure of the material or from interfaces where symmetries are broken. This work will purely focus on the shape-induced anisotropy, where the investigated shape is that of a thin rectangular film, as is the case for the magnetic thin film on top of the pressure sensor's membrane. Figure 2.3 illustrates the easy- and hard-axis of an ellipsoid, a thin film and a bent thin film, due to shape anisotropy. When a material is magnetised, it generates a stray field outside the magnetic material and a so-called demagnetising field inside the magnetic material. It is this demagnetising field that gives rise to shape anisotropy, for it works against the magnetisation. This means that the easy-axis is the one where the demagnetising field is minimal. It is thus important to know the demagnetising field. The demagnetising field can be expressed as $\boldsymbol{H}_d = -\bar{\boldsymbol{N}} \cdot \boldsymbol{M}$, where $\bar{\boldsymbol{N}}$ is the demagnetisation tensor which is dependent on the material shape. The tensor elements can analytically be determined for ellipsoid shapes [13], however, it is difficult to determine for arbitrary shapes. The demagnetisation tensor of a thin film can be approximated by approaching the thin film as a wide but thin ellipsoid, i.e. an ellipsoid with low aspect ratio. This results in a demagnetisation field that is strongest in the out-of-plane direction and weakest in the plane. As a rule of thumb the demagnetising field is smallest along the longest axis of a material,

making that the easy-axis. Note that there are also easy- and hard-planes, which occur when the axis lies in a plane where no distinction can be made of direction, such as a disc. In reality the rectangular shape has an energy difference between the long- and short-axis in the plane, however this energy difference is small compared to the out-of-plane hard-axis and thus often neglected. As such a thin film is approximated to have an out-of-plane hard-axis and an in-plane easy-plane.

The bent thin film of Figure 2.3c is investigated in this work, where the assumption is made that the easy-plane is always parallel to the thin film at every point. Note that the bending in the illustration is greatly exaggerated and that in reality the slope of the top membrane, and thus of the magnetic thin film, is approximately 0.2° at atmospheric pressure. The anisotropic constant of a thin film is approximated as $K = \frac{1}{2}\mu_0 M_S^2$, where $M_S$ is the saturation magnetisation. This leads to a shape anisotropy energy density of:

$$E_a = \frac{1}{2}\mu_0 M_S^2 \sin^2(\theta). \tag{2.4}$$

The equation clearly demonstrates that there is an energy cost when $\theta$ is not zero, and as such the magnetisation would want to lie in the easy-plane. This energy density is used in the Stoner–Wohlfarth model, where it competes with the Zeeman energy density for determining the magnetisation rotation $\theta$. From this equation it is clear that the shape-induced anisotropy scales with the saturation magnetisation $M_S$. This means that the typical field strength necessary to overcome the anisotropy is on the order of 1 T, the typical saturation magnetisation of strong ferromagnets.

### 2.2.3 Stoner–Wohlfarth model for coherent rotations

The Stoner–Wohlfarth model is used to describe the orientation of the magnetisation, with respect to an easy-axis and an external magnetic field. This is important as the mechanical responses of the next section are derived from the magnetisation orientation, which result in a deflection of the magnetic thin film. The Stoner–Wohlfarth model describes the magnetisation of a uniformly magnetised material under externally applied magnetic fields and is the easiest model to describe magnetic hysteresis [14]. The model incorporates the Zeeman energy density and a uniaxial anisotropy energy density. For a generic anisotropy the total energy density is given by:

$$E = K_u \sin^2(\theta) - \mu_0 M H \cos(\alpha - \theta), \tag{2.5}$$

where $K_u$ is the uniaxial anisotropy constant and $\theta$ and $\alpha$ are defined with respect to the easy-axis, as is shown in Figure 2.4. By minimising the energy density with respect to $\theta$, either one or two energy minima are found. Hysteresis is present in the region of two energy minima, where switching between minima occurs at the inflection point. The magnetic field strength that is necessary to switch the magnetisation along the easy-axis is referred to as the coercive field. Figure 2.5 shows typical hysteresis loops that are described by the Stoner–Wohlfarth model, where the external field is swept along the easy- or hard-axis. For the easy-axis a sharp transition is seen at the coercive field $H_C$, as the magnetisation switches from one energy minima to the other. The hard-axis sweep does not show hysteresis, as there is no non-zero stable energy state at zero field. The magnetisation does saturate

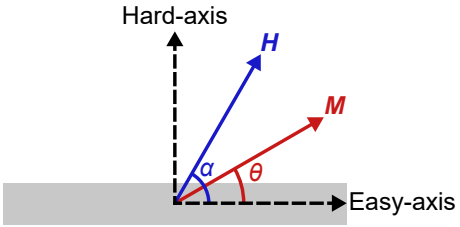


Figure 2.4: Schematic of the Stoner–Wohlfarth model, denoting the angles $\alpha$ and $\theta$ as the angles between the anisotropic easy-axis and the external magnetic field $\boldsymbol{H}$ and magnetisation $\boldsymbol{M}$ respectively.

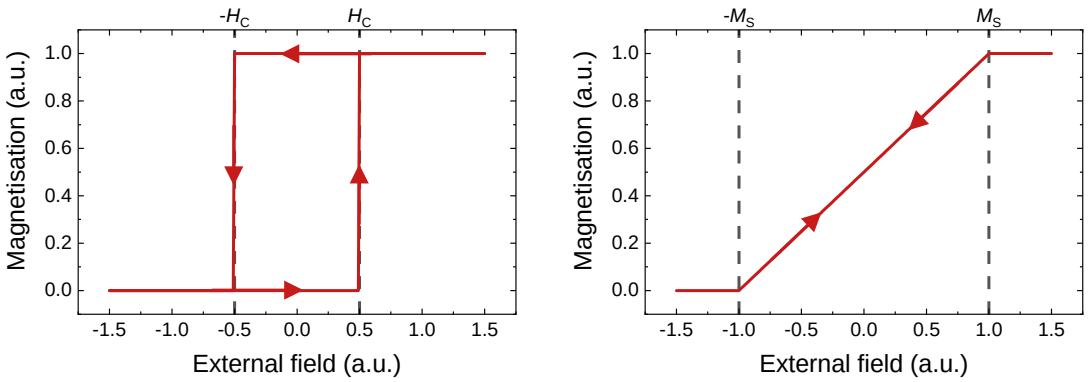


(a) (b)

Figure 2.5: Example hysteresis loops, where the external field is swept along an easy- or hard-axis. (a) Easy-axis sweep, showing a hysteresis loop. The magnetisation switches at the coercive field $H_C$. (b) Hard-axis sweep. The magnetisation follows the external field, saturating when the external field reaches the saturation magnetisation $M_S$.

when the external field is larger than or equal to the saturation magnetisation field $\mu_0 M_S$.

Although usually the Stoner–Wohlfarth model is used to describe hysteresis, this work is focused on the rotation of the magnetisation. As such the Stoner–Wohlfarth model is used with the assumption that the magnetisation is always saturated and hysteresis is negligible, this is also called a macrospin approach as the magnetization of the system is assumed to be homogenous. The materials used in this project have small coercive fields along the easy-axis, on the order of a few mT or less, as such the effects of hysteresis are expected to be small and clearly distinguishable in the measurements.

For the Stoner–Wohlfarth model, equations 2.2 and 2.4 are combined, which results in the total energy density:

$$E = \mu_0[\frac{1}{2}M_S^2 \sin^2(\theta) - HM_S \cos(\alpha - \theta)]. \tag{2.6}$$

The direction of magnetisation $\theta$ can be determined from this equation by finding

the minimal energy density for a specified external field. Note that $\theta$ lies between 0°, fully aligned with the easy-axis, and the external field angle $\alpha$. Because of this, the total energy density decreases as $\alpha$ approaches the easy-axis, where $\theta$ becomes zero and the $\sin^2(\theta)$ term vanishes.

The solutions of $\theta$ can be determined numerically, or analytically for the specific case of a perpendicular field, i.e. the field applied along the hard-axis $\alpha = 90°$. The analytical solution can be derived as follows:

$$\begin{aligned} \frac{dE}{d\theta} &= 0, \\ HM_S \sin(\alpha - \theta) &= M_S^2 \sin\theta\cos\theta, \\ \sin(\alpha - \theta) &= \frac{M_S}{H}\sin\theta\cos\theta. \end{aligned} \tag{2.7}$$

By putting in $\alpha = 90°$ and reordering the equation, the angle $\theta$ is given by:

$$\sin(\theta) = \frac{H}{M_S}, \tag{2.8}$$

under the condition that $H \leq M_S$. If $H \geq M_S$ the angle $\theta$ equals $\alpha$. Figure 2.6 illustrates the analytical solution of $\theta$ as function of the external field $H$. For this calculation $\mu_0 M_S = 1.36$ T, which is the saturation magnetisation of the material used in this project, CoB [15]. This solution is only for the case of $\alpha = 90°$, where numerical solutions are necessary for other angles. The numerical solutions are determined by solving equation 2.7 in MATLAB [16], which is presented in Section 4.1. This results in the magnetisation angle $\theta$ with respect to the easy-axis, as function of the external field strength $H$ and angle $\alpha$.

In reality the magnetisation of the film is not always uniform. Magnetic domains can form that split the film into areas of different magnetisation direction, where the transition area between domains is defined as a domain wall. This would mean that the Stoner–Wohlfarth model cannot be used, as one of the requirements of the model is a uniform magnetisation. However, the magnetisation within a domain

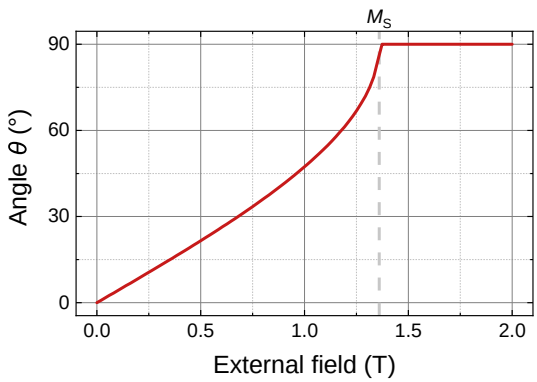


Figure 2.6: Analytical solution of the magnetisation angle $\theta$, as function of the externally applied field $H$ at an angle $\alpha = 90°$. The angle $\theta$ approaches $\alpha$ and fully aligns above the saturation magnetisation $M_S$, which for CoB equals 1.36 T [15].

can be considered as uniform. In order to use the Stoner–Wohlfarth model, the film is discretised such that each discretisation is a single magnetic domain with a uniform magnetisation. The magnetic films that are studied in this project are relatively thick and have a magnetic easy-plane. Because of this the magnetisation can change easily, resulting in fewer and smaller domain walls. It is thus assumed that the domain walls are insignificant compared to the actual domains, and thus are neglected in this work.

## 2.3 Mechanical responses in magnetic films

In the end, the goal is to deflect the magnetic film due to interactions with an external magnetic field. The previous section introduced the magnetic orientation of the film as function of external magnetic field. This section will expand on this and describe how the magnetic orientation can produce a mechanical force on the film, that results in a deflection of the film. Firstly the effects of magnetic torque are introduced, which is followed up by the force related to a magnetic field gradient. Finally, the Maxwell stress formalism is introduced, which takes into account both the torque and gradient forces. The Maxwell stress is used in modelling the magnetically-induced deflection in Chapter 4.

### 2.3.1 Magnetic torque & deformation of the film

In the previous section it was discussed that the magnetisation wants to align itself along a certain direction, which is determined by the anisotropy and external magnetic field. This tendency is mediated by the magnetic torque, that rotates a magnetisation. Figure 2.7a illustrates the torque working on a magnetisation that wants to align with the external field according to the Zeeman effect. The torque $\boldsymbol{\tau}$ is expressed in terms of $\boldsymbol{M}$ and $\boldsymbol{H}$ as:

$$\boldsymbol{\tau} = V\boldsymbol{M} \times \mu_0 \boldsymbol{H}, \tag{2.9}$$

with $V$ the volume of the magnet. The volume has to be taken into account as the torque acts on a magnetic moment, where the magnetisation is the density of the magnetic moment.

The magnetic torque rotates the magnetisation, but not the film. In order to deform the film a relation between the magnetisation and the shape of the object is necessary. This is provided by the anisotropy of the material, that relates the magnetisation direction to the easy-axis of the material [9]. The Stoner–Wohlfarth model, from Section 2.2.3, is used to determine the stable magnetisation orientation from which the torque is derived. This is formulated as:

$$\tau = \mu_0 V M H \sin(\alpha - \theta). \tag{2.10}$$

Here $(\alpha - \theta)$ represents the angle between $\boldsymbol{M}$ and $\boldsymbol{H}$. Figure 2.7b illustrates the torque, determined by the analytical solutions of $\theta$ from Section 2.2.3, with $\alpha = 90°$. Here the volume is set to $V = 1.12{\cdot}10^{-14}$ m$^3$, the volume of a full $700{\times}175$ $\mu$m$^2$ membrane with 100 nm CoB, and the saturation magnetisation is set to $\mu_0 M_S = 1.36$ T, the saturation magnetisation of CoB. Notice that the torque drops after $M_S$, as

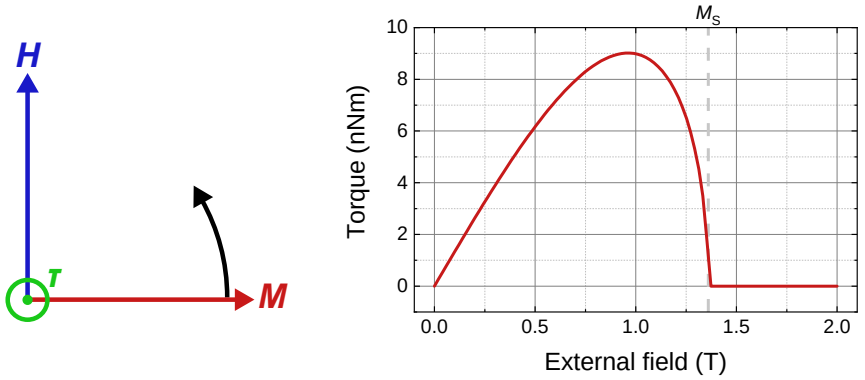


(a) (b)

Figure 2.7: (a) Illustration of the magnetic torque $\boldsymbol{\tau}$ pointing out of the paper, rotating the magnetisation $\boldsymbol{M}$ towards the external field $\boldsymbol{H}$. (b) Analytical solution of the torque as function of the external field, using the solutions of $\theta$ as illustrated in Figure 2.6. The torque drops to zero after the saturation magnetisation $\mu_0 M_S = 1.36$ T, because the magnetisation is fully aligned with the external field and thus no torque is exerted.

the magnetisation fully aligns with the external field and $\theta = \alpha$. The behaviour of the torque at arbitrary angles $\alpha$ is investigated in Chapter 4, where the numerical solutions of $\theta$ and $\tau$ are determined.

A hypothesis for the deformation profile of the thin magnetic film is sketched in Figure 2.8. It illustrates the deflections for a perpendicular and non-perpendicular magnetic field. The illustrations are split into the following three parts: determining the local easy-axis, the direction of the torque, and the magnetically-induced deflection. The first part sketches the initial magnetisation $\boldsymbol{M_i}$ that is aligned with the local easy-axis. The local easy-axis is established from the projection of the external field $\boldsymbol{H}$ onto the easy-plane, which coincides with the shape of the deformed film. The magnetisation $\boldsymbol{M}$ will cant from the local easy-axis towards the external field due to the torque. The second part shows how the torque will try to deform the film such that the local easy-axis is more aligned with the external field, lowering the total energy of the Stoner–Wohlfarth model. Finally, the third part illustrates the additional deflection that is induced through the torque. What follows will elaborate on the magnetically-induced deflections of Figure 2.8, from which it will become clear why this work primarily focusses on perpendicular magnetic fields.

For the non-perpendicular field of Figure 2.8a there is a clear in-plane component of the external field, which determines the initial direction of $\boldsymbol{M_i}$ that will cant towards $\boldsymbol{H}$. This results in the sloped left end of the film being pushed upwards, while the right end is pushed downwards, an anti-symmetric deformation. For the perpendicular field of Figure 2.8b, the initial direction of $\boldsymbol{M_i}$ is split, as the projection of $\boldsymbol{H}$ results in a left pointing $\boldsymbol{M}$ on the left, and a right pointing $\boldsymbol{M}$ on the right. The torques on these ends result in them both being pushed downwards to increase the alignment of the local easy-axes with the external field. The end result is a symmetric deformation, which has greater deflection than the anti-symmetric

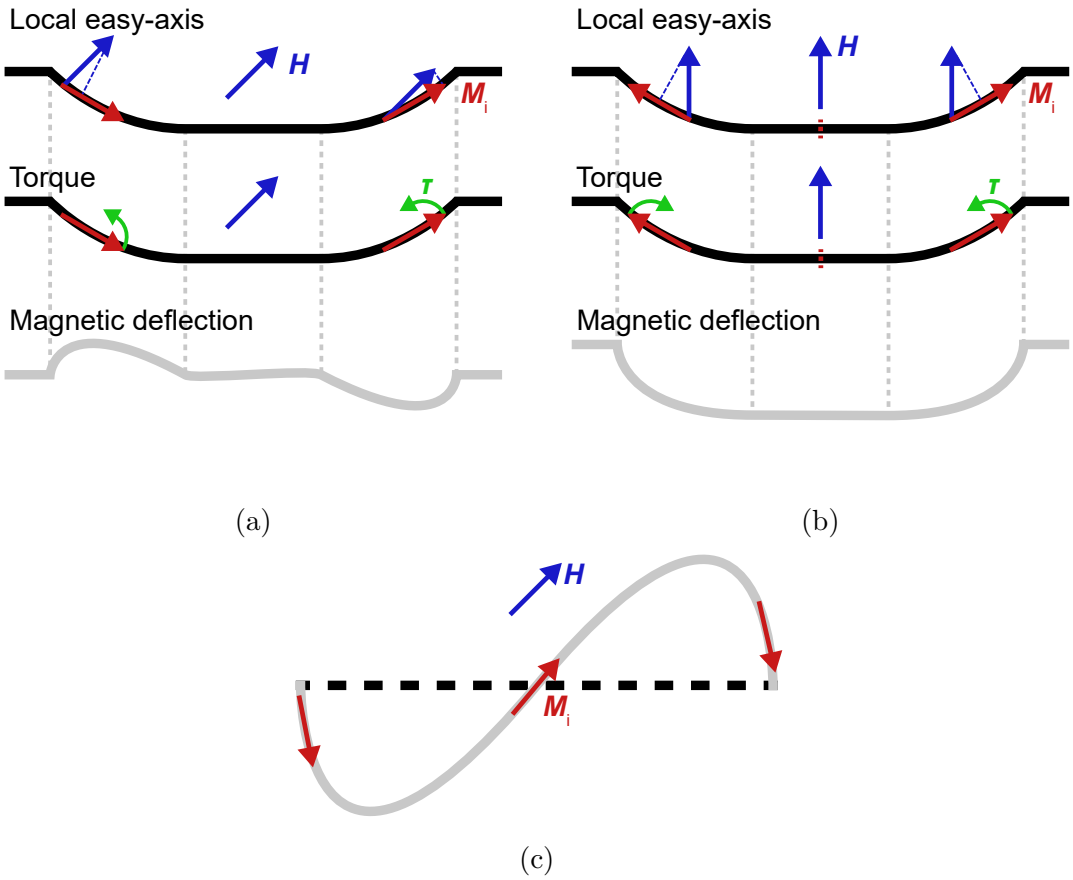


Figure 2.8: Illustrations of the magnetic deflection that is derived from the torque. The local easy-axis is defined by the projection of the external field $\boldsymbol{H}$ onto the film. The magnetisation $\boldsymbol{M}$ cants from the local easy-axis towards $\boldsymbol{H}$, resulting in a torque $\boldsymbol{\tau}$. (a) For non-perpendicular $\boldsymbol{H}$ the torque creates an anti-symmetric deflection. (b) Perpendicular $\boldsymbol{H}$ results in a symmetric deflection. The dashed red line denotes a domain wall, where the magnetisation switches direction. (c) Depiction of the deflection of a flat film. The magnetisation is aligned in the centre, but anti-aligned at the edges. This deflection is unlikely as the total energy of the system would not be changed compared to a flat film.

deformation. Perpendicular fields are thus preferable and will be the focus of this work.

Note that the initial bathtub-like shape due to pressure, as introduced in Section 2.1, is necessary to get any magnetic deformation at all, because rotations of a flat film do not reduce the total energy. As illustrated in Figure 2.8c, the continuous deformation of the film would cause any part of a flat film that is more aligned with $\boldsymbol{H}$, to be compensated by a part that becomes anti-aligned.

To get a feel of the effective deflection, that can be induced through torque, a rough estimation is made of the force from a perpendicular magnetic field using the geometry of the magnetic film. In this estimation it is assumed that the torque works

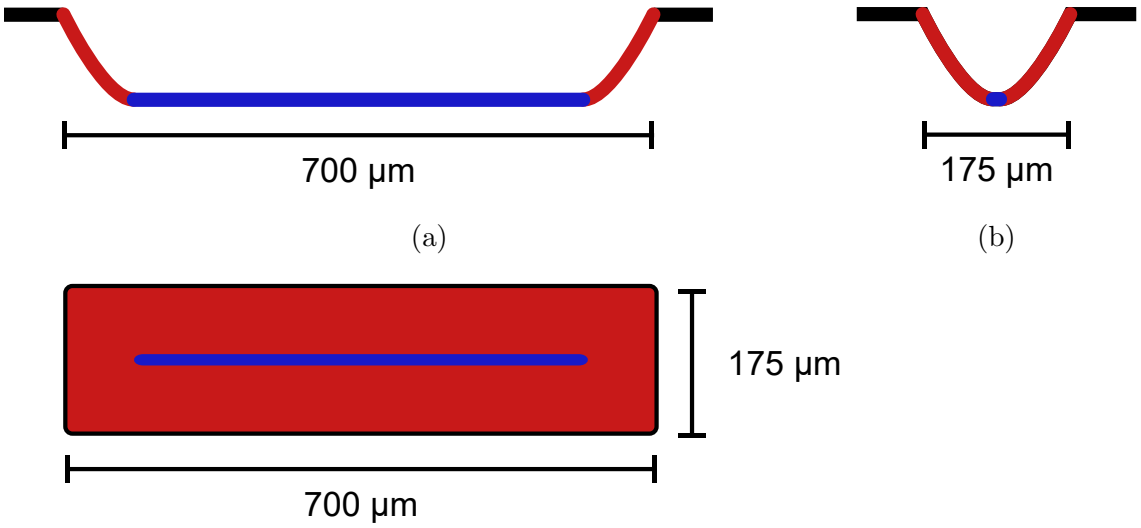


Figure 2.9: Illustrations showing the sloped (red) and flat (blue) parts of the membrane. (a) Side-view of the long-axis of the membrane. It has the distinct bathtub-like shape with a long flat area. (b) Side-view of the short-axis of the membrane. Most of the membrane along the short-axis is sloped. (c) Top-view of the membrane, showing that only a small area of the membrane is truly flat.

on the entire membrane and that an average force can be used as a lower bound of the total applied force. In the previous paragraph it was noted that the torque does not work on flat membranes, however, the stated assumption is reasonable because in the bathtub-like shape only small parts of the membrane are considered to be flat as is illustrated in Figure 2.9. The maximum torque for perpendicular fields is retrieved from Figure 2.7b, which results in a torque of 9.0 nNm. The average force is estimated to be equal to the torque applied at 350 $\mu$m, half the length of the film, which results in a force of 26 $\mu$N. This is an underestimation of the actual force, as most of the torque contribution is in the short-axis of membrane, not the long-axis. If this force were to be applied over the entire film it is equal to a pressure of 210 Pa. This would be easily measured as the device has a pressure resolution of 1 Pa. Notice that an additional pressure of 210 Pa is small compared to the atmospheric pressure of $10^5$ Pa. This means that the local easy-axis of Figure 2.8 is likely not perturbed by the magnetic deflection.

### 2.3.2 Magnetic field gradient reaction force

The magnetic field gradient is discussed here for completeness and simulation possibilities. However, the expected deflection due to field gradients is rather small, as will be discussed here. Because of this no measurements have been done on magnetic field gradients within the time frame of this project. As such, in measurements the magnetic gradient is controlled to be minimal, such that only magnetic torques are investigated. The rest of this section will briefly introduce the mechanical force that is derived from the magnetic field gradient, and give an example on how a current could be measured using the field gradient.

The magnetic field gradient leads to a mechanical interaction, that pulls the magnetisation along the field gradient. The easiest example of this is the attraction between two bar magnets. These are attracted to each other by the gradient of the stray fields that they generate. For a uniform magnetisation the force from the gradient field is given by:

$$\boldsymbol{F} = \nabla(V\boldsymbol{M} \cdot \boldsymbol{B}), \tag{2.11}$$

where $\boldsymbol{B}$ is the magnetic flux density from one magnet on the other.

What follows is an example of the force on a magnetic film that can be expected from the field gradient, that is generated by a current wire. An illustration of the magnetic field generated by a current wire is shown in Figure 2.10. The current wire generates a magnetic field according to Ampères law, which for an infinite wire results in the field:

$$B = \mu_0 \frac{I}{2\pi r_w}, \tag{2.12}$$

where $I$ is the current and $r_w$ the distance from the wire. The field curls around the wire and diminishes with the distance to the wire as $1/r_w$, which results in a field gradient. A magnetic film with a magnetisation component aligned with the field gradient will be pulled towards the region with the highest flux density, i.e. along the gradient towards the wire. Note that to get a deflection of the film, the magnetisation thus needs to be aligned with the external magnetic field and the gradient needs to be perpendicular to the film, as is the case for this example.

For the situation that is illustrated in Figure 2.10, the force is given by:

$$F = -VM\mu_0 I/(2\pi r_w^2). \tag{2.13}$$

For comparison with the torque, the force is calculated for a set current of 1 A at $r_w = 1$ mm. Using the same values for $V$ and $M = M_S$ as in the previous section,

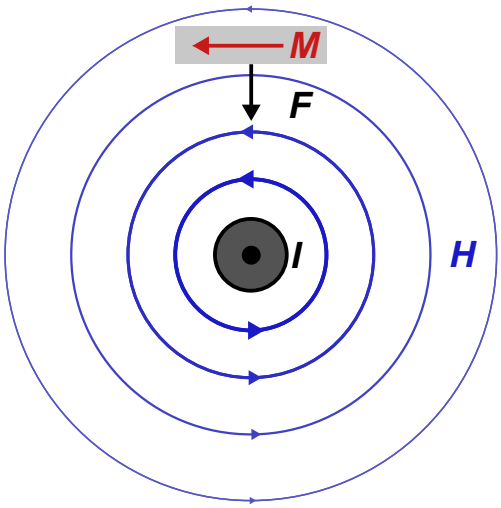


Figure 2.10: Illustration of the magnetic field $\boldsymbol{H}$, of a current wire $\boldsymbol{I}$ that points out of the paper. The magnetic field acts on a permanent magnet $\boldsymbol{M}$ through the gradient force $\boldsymbol{F}$.

results in a force equal to 2.65 nN. This force is applied on the entire film and thus equal to a pressure of 0.02 Pa. This is minuscule compared to the pressure achieved with a torque from a uniform field, as in the previous section. A current of 10 kA, at a distance of 1 mm, is needed to achieve the same pressure of 210 Pa, as was the case for maximum torque. It is thus easier to investigate the magnetic torque by generating strong uniform magnetic fields, than to investigate the field gradient of a current wire. Because of this difference in estimated pressure, the effects of magnetic torque are measured in this thesis, before considering field gradient measurements.

### 2.3.3 Maxwell stress formalism

The advantage of the Maxwell stress formalism is the ability to calculate the magnetic mechanical forces on the film as a stress on the surface, instead of force densities or cumbersome torques. The Maxwell stress is a mathematical construct that incorporates the mechanical responses from magnetic fields on magnetised objects, including both the magnetic torque and magnetic gradient. The main result of this is the force equation:

$$\boldsymbol{F} = \oint \boldsymbol{T}\, dA, \tag{2.14}$$

where $\boldsymbol{T}$ is the Maxwell stress tensor and the integral is over the surface area of the magnetic film. The tensor is given by:

$$\boldsymbol{T}_{ij} \equiv \epsilon_0(E_i E_j - \frac{1}{2}\delta_{ij}E^2) + \frac{1}{\mu_0}(B_i B_j - \frac{1}{2}\delta_{ij}B^2), \tag{2.15}$$

where $\boldsymbol{E}$ is the electric field, $\epsilon_0$ the permittivity of vacuum and $\delta_{ij}$ is the Kronecker delta. Note that, while the tensor depends on the electric field, $E = 0$ for all considerations in this work. The Maxwell stress is utilised in the finite-element modelling that is presented in Chapter 4. In the model $\boldsymbol{T}$ is resolved for each element, from which the force on the magnetic film is determined. It is good to note that this is only a mathematical construct, and that the underlying principle is still the torque that induces deflections of the magnetic film. From the equations it can be seen that a force is only exerted when the contour integral is not zero, i.e. the magnetic flux components $B_i$ should change over the contour. This is the case for permanent magnets in uniform external magnetic fields, like the ones investigated in this project, when the magnetisation and external magnetic field are not fully aligned. This is the same behaviour as the torque, which vanishes when the magnetisation and external magnetic field are aligned.

Because the Maxwell stress tensor is a more exotic mathematical object, a complete derivation is given in Appendix A.1, following the book of Griffiths [17].

# 3
# Methods

In this chapter the fabrication of the flexible magnetic film is discussed, as well as the different measurement set-ups. The first section details the magnetron sputter deposition method, which is used to fabricate the magnetic layer. In addition, the rationale for the chosen magnetic material is given and the capacitive pressure sensor, as a platform, is discussed. In the second section the measurement set-ups are described, including the uniform magnetic field, pressure tank, Dektak profilometer, and MOKE set-ups. The uniform magnetic field set-up is used in several different measurements, where the external magnetic field and field angle are varied. The pressure tank set-up is used to measure the error in the measured pressure per device compared to a set pressure. This error is expected due to the added stiffness of the magnetic layer, for which the device is not calibrated. The Dektak is used in height profile measurements of the membrane, for verification of the bathtub-like deflection profile and comparison to the COMSOL models. Finally, the MOKE set-up is used to measure the magnetic hysteresis of the film. The results from these measurements are shown in Chapter 5, where they are compared to the theory and modelling results, with the goal to understand and optimise the magnetically-induced deflection as function of the external magnetic field and magnetic layer thickness.

## 3.1 Sample fabrication

The measurement and fabrication foundation of this project is the fully assembled pressure sensor of AMS Netherlands. Because it is a complete device it has the benefit of being reliable, but this also brings limitations for adding additional layers to the membrane. The first section introduces the general method of magnetron sputter deposition, which is used to add the magnetic layer to the existing devices. The second section discusses the choice of magnetic material and elaborates on the other components of the material layer stack. Finally, in the third section, the device as a platform and the required deposition mask are examined.

### 3.1.1 Magnetron sputter deposition

Magnetron sputtering is chosen as the deposition method, due to its capability to produce thin films in the range of a few nanometers to hundreds of nanometers thick. This is the desired layer thickness range for investigation, such that the magnetic layer only plays a minor role in the stiffness of the membrane, which is a few microns

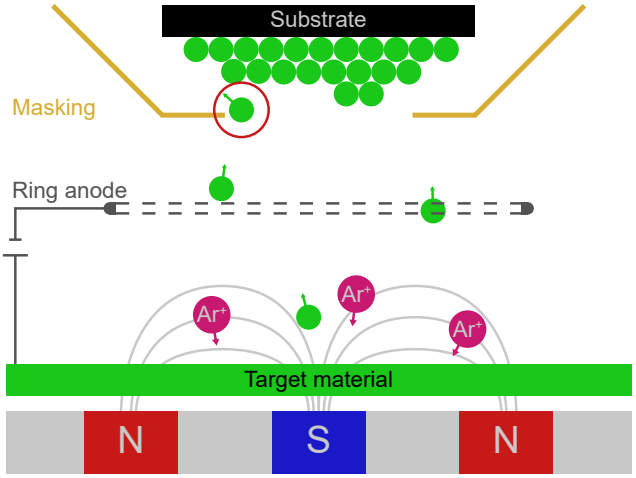


Figure 3.1: Schematic of the working principle for magnetron sputtering. $Ar^+$ ions bombard the target material, which releases target atoms in a ballistic way. Because the target atoms are launched into all directions, a mask is used to confine the deposition. However, the mask is not ideal and shadowing effects can occur, as indicated by the red circle. This results in partial depositions close to the edges of the masked area. The letters N and S denote the polarity of the magnet, creating a confining magnetic field for the $Ar^+$ plasma. This image is adapted from [22].

thick. The material that is deposited in magnetron sputtering is referred to as the target material. The chosen target materials are detailed in the next section. To prevent contamination of the target material, the entire sputter deposition chamber is put under an ultra high vacuum, with pressures below $10^{-8}$ mbar. Only direct current (DC) sputtering is considered in this section, as all used target materials are metallic.

Figure 3.1 shows a schematic of the sputter chamber. The principle of magnetron sputter deposition is the bombardment of a target material with ions, such that the target atoms are released and reach the substrate by ballistic transport. To this end argon (Ar) gas is led into the chamber, increasing the pressure to $10^{-2}$ mbar. Ultra pure Ar gas is used because it is an inert gas, and thus does not contaminate the target material. The Ar gas is ionised by a strong potential difference between the ring anode and the target material, that acts as cathode. This forms an $Ar^+$ plasma that is confined in proximity of the target material by a magnetic field, denoted by the grey lines. The positive $Ar^+$ ions are accelerated towards the negatively charged target material and on impact they release atoms of the target material. The atoms are released into the chamber, where they impact onto the substrate material. In this project the substrate is the membrane of the pressure sensor, where the top-layer consists of silicon nitride ($Si_3N_4$). The typical deposition rate of magnetron sputtering is close to 1 Å/s, or 0.1 nm/s. This rate is sufficient for this project, as all magnetic layers are deposited with a thickness greater than 10 nm.

The deposition is done by ballistic transport of the target atoms, which are launched into all directions. To restrict the deposition to the membranes a deposition-mask is added, as shown in Figure 3.1 in dark orange. The masking is put on top of the device to prevent deposition on other areas of the device, as there is circuitry exposed

on the device that will short-circuit when covered by a metallic layer. However, the non-directional release of target atoms means that some arrive under an angle and can impact on the substrate below the mask, as indicated by the red circle in the schematic. The result is a Gaussian-like deposition distribution, that reaches below the mask. This shadowing effect can be reduced by bringing the mask closer to the substrate. The specifics of the used mask will be further discussed in Section 3.1.3

In short, magnetron sputtering is based on the principle of bombarding a target material with inert ions, such that atoms of the target condense onto a substrate. This can create thin film layers, that in this project have a thickness on the order of tens of nanometers. Non-ideal masking can lead to shadowing effects, where partial depositions occur near the edge of the mask.

### 3.1.2 Magnetic material choice

The layer stack, consisting of the membrane and the deposition, is shown in Figure 3.2. The membrane, as delivered, is composed of a 500 nm tungsten (W) layer and a 1900 nm silicon nitride ($Si_3N_4$) layer. The other layers are deposited according to the previous section. The W layer acts as an electrode for the capacitive pressure sensor, which is chosen for its flexibility and mechanical strength. The $Si_3N_4$ layer acts as cover for the W layer, protecting and insulating it from external sources. Although the substrate membrane is suspended, it is not expected to cause problems with the deposition, as the membrane experiences tension.

The chosen magnetic layer is an alloy of cobalt (Co) and boron (B) with the ratio $Co_{80\%}B_{20\%}$, from now on simply referred to as CoB. The material choice is mainly dependent on the material's intrinsic anisotropy and saturation magnetisation. To reduce the complexity of this study, only shape anisotropy is considered. However, to do this the material must have no intrinsic anisotropy. Intrinsic anisotropy comes in the form of crystalline anisotropy, where the magnetisation wants to align with a specific crystalline axis of the material. CoB is an amorphous alloy, which means that it does not have a crystalline structure and thus no crystalline anisotropy. In the Theory chapter it was made clear, that the strength of the torque depends on

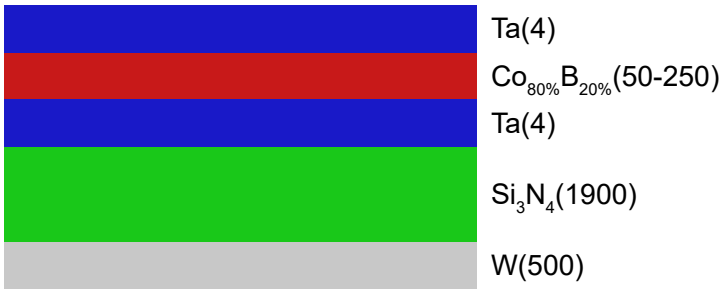


Figure 3.2: Schematic of the used material stack. The membrane that acts as substrate consists of W(500 nm) and $Si_3N_4$(1900 nm). On top of this Ta(4 nm)/$Co_{80\%}B_{20\%}$(50-250 nm)/Ta(4 nm) is deposited using magnetron sputtering.

the magnetisation and the magnetic field. The maximum magnetisation achievable in a material is denoted as the saturation magnetisation. CoB is chosen for its relatively large saturation magnetisation of $\mu_0 M_S = 1.36$ T [15]. The CoB thickness range of 50 nm to 250 nm is chosen for modelling dictates that the resulting magnetically-induced deflections are large enough to be measured by the sensor. The layer thickness is limited by the sensor, where thicker layers might cause electrical shorts of the device, as will be discussed further in Section 3.1.3.

The CoB layer does experience magnetostriction, which relates the direction of magnetisation to strains in the magnetic film. This means that a strain on the magnetic film can induce an extra anisotropy field on top off the shape-induced anisotropy. In order to check the significance of magnetostriction, the maximum anisotropy field due to magnetostriction can be calculated with the following equation [13]:

$$\mu_0 H_{ms} = \sqrt{\frac{3}{2}\mu_0 \lambda_s^2 E_Y}, \tag{3.1}$$

with $\mu_0$ the vacuum permeability, $H_{ms}$ the magnetostriction anisotropy field, $\lambda_s$ the saturation magnetostriction and $E_Y$ the Young's modulus. Using the properties of pure Co [13, 20], which has stronger magnetostriction than CoB [23], results in a magnetostriction anisotropy field of $\mu_0 H_{ms} = 38$ mT. This anisotropy field is much smaller than the shape-induced anisotropy, which is on the order of 1 T. The magnetostriction effects in CoB should thus be negligible in the measurements and are ignored in modelling.

Another magnetic material that is well suited for this project is the nickel (Ni) iron (Fe) alloy $Ni_{80\%}Fe_{20\%}$, that is better known as Permalloy. Permalloy has no crystalline anisotropy and has a saturation magnetisation of $\mu_0 M_S = 1.04$ T [13]. Furthermore, Permalloy is well known for having nearly no magnetostriction. There are materials with an even higher saturation magnetisation, like pure Fe with 2.1 T, but these often experience crystalline anisotropy and have much greater magnetostrictive effects than the amorphous alloys. This could be resolved by looking at amorphous alloys consisting of Fe, like CoFeB or FeB. In the end CoB was used because of its relatively high saturation magnetisation, its unnoticeable magnetostriction, and moreover because it was readily available for deposition.

The schematic of the layer stack shows tantalum (Ta) layers between the membrane and the magnetic layer, and on top of the magnetic layer. The separation layer on top of the $Si_3N_4$ acts as an adhesion layer for the CoB. In general deposited materials don't grow well on different materials, such as CoB on $Si_3N_4$. However, Ta is well known for easily adhering to other materials. As such Ta is first deposited onto the membrane to create a good adhesion layer for the magnetic deposition. The other Ta layer covers the magnetic CoB layer. This is necessary to prevent oxidation of the magnetic layer. Oxidation would be detrimental to the device, as the oxidised CoB layer would no longer be magnetic. Now only parts of the Ta layer are oxidised, instead of the magnetic layer.

In short, CoB is used because it has no intrinsic anisotropy, has a high saturation magnetisation at 1.36 T, shows no magnetostriction, and was easily available for

deposition. Extra Ta layers are added as adhesion layer and cover to protect against oxidation of the magnetic layer.

### 3.1.3 The device as a platform & deposition masking

In this section details and complications of the pressure sensor, as it is delivered by AMS Netherlands, are discussed. The pressure sensor is a product and comes with packaging and circuitry to be used by a customer. Figures 3.3 and 3.4 show the device and an approximate scale 3D model of it. Note that it not only consists of the sensor, but also a printed circuit board (PCB) and gold coated connector pins. The PCB and connector allow the device to be easily connected to a computer for readout.

The sensor consists of two membranes, which can be seen as the light grey coloured strips on the sensor, as highlighted by the red box in Figure 3.3. Both membranes have the same dimensions and result in a single pressure value readout. Because of this the magnetic layer deposition needs to cover both membranes equally for proper measurement. The width of the membrane can change between devices, however, all devices measured in this project have membranes that measure 175 $\mu$m by 700 $\mu$m each. The sensor can reliably achieve a resolution of 1 Pa on a range of $10^5$ Pa, which, for its size, energy consumption and fast readout time on the order of milliseconds, is the current state of the art. The sensor's accuracy and fast response make it ideal to investigate magnetically-induced deflections of the membrane. The changes in deflection, and thus pressure, are expected to be as small as several picometers up to a few nanometers. Moreover, the magnetic response is dominated by the Landau–Lifshitz–Gilbert (LLG) equation, resulting in magnetic responses on the order of GHz. As such, a highly accurate and fast readout is important to measure the details of the magnetically-induced deflection.

While the sensor outputs a pressure value, discussing magnetically-induced deflections as a pressure is not intuitive. As such, the magnetically-induced pressure changes are reported in terms of an effective deflection, which was already introduced in Chapter 1. The effective deflection is simply a re-scaling of the pressure,

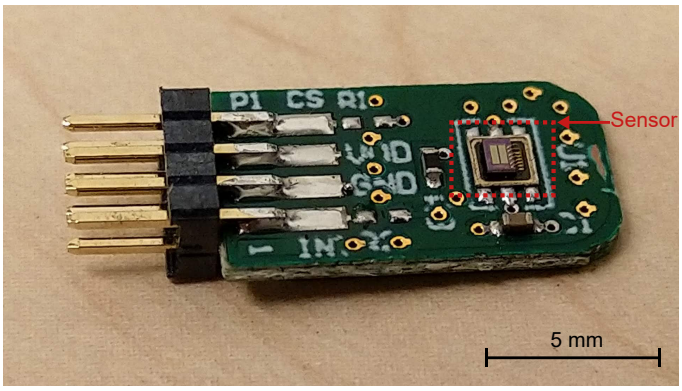


Figure 3.3: Photo of the device, including the PCB connector. The sensor can be seen on the right, where the light grey strips are the membranes. The sensor is approximately $2 \times 2$ mm$^2$, and each membrane is $700 \times 175$ $\mu$m$^2$.

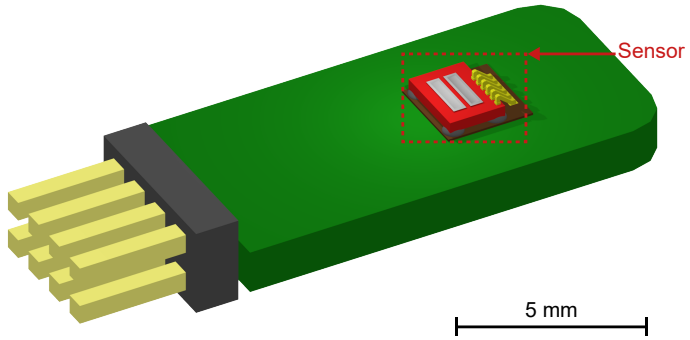


(a)

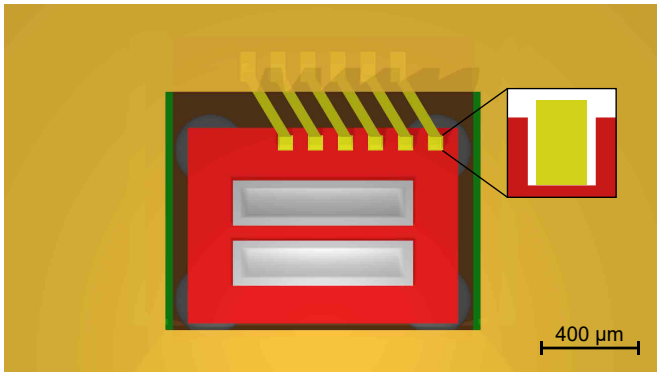


(b)

Figure 3.4: (a) Approximate scale 3D model of the device including the PCB (green) and connector pins (yellow). (b) Illustration of the area masked by Kapton tape in orange. The region ensures full coverage of the membranes without short-circuiting the lower bond pads. The inset depicts the upper bond pads, where the gap between the bond pad and the walls prevents electrical shorts up to a deposition thickness of approximately 325 nm.

by the amount of deflection per applied pressure. It is referred to as the effective deflection because it is not necessarily the actual deflection, but is derived from the pressure, which is integrated over the entire membrane. The typical deflection per unit pressure is measured in Chapter 5, where the deflection profile at atmospheric pressure is investigated. From measuring a sensor with 100 nm CoB a conversion factor 3.5 pm/Pa is determined. It is good to note that the sensor's resolution of 1 Pa, thus equals an effective deflection resolution of 3.5 pm. To bring the quality of the sensor into perspective, the average distance between atoms is 1 Å, i.e. 100 pm. While the effective deflection is integrated over a surface, it manages to differentiate changes in the effective deflection that are about 30 times smaller than the distance between atoms. In turn the magnetic resolution is defined as the necessary magnetic field change to induce a resolvable 3.5 pm deflection.

In the illustrations of Figure 3.4 the bond pads and bond wires can be seen, with a set of pads on the sensor and a set on the brown plate that is attached to the PCB. Besides the bond pads, the PCB also has exposed circuits and connections. This is a problem, as the magnetic layer depositions are metallic and would cover the entire device. The metallic layer would cause electrical shorts and render the device

unusable. To resolve this, masking methods are used during the deposition, such that only the area around the membranes is covered by metals. Conventionally a solid plate mask is brought very close to the deposition substrate, such that the rest is protected and shadowing effects are minimal. This could unfortunately not be used, as the device has protrusions, like the bond pads on the sensor, and thus the mask cannot be brought close enough. The bond wires could be removed, however, attempts at manually rewiring them had failed. Instead the masking was done manually with Kapton tape. The tape was applied by hand using a set of tweezers, in such a manner that mainly the membranes are open to the deposition. Figure 3.4b depicts the masking area. A larger area than the membranes is left open to ensure full deposition on the membranes. The top bond pads are safe from electrical shorts due to their placement on the sensor, as shown in the inset of Figure 3.4b. The pit, in which the bond pad is connected, is deep enough to safely deposit magnetic layers up to 250 nm, where at 325 nm electrical shorts start to occur. The precision of the mask placement needs to be on the order of tens of micrometers, which by hand takes several attempts. This greatly increased the time necessary to fabricate new devices.

In short, the sensor comes delivered on a PCB that can be connected to a computer, where a pressure resolution of 1 Pa is achieved. In magnetically-induced deflection measurements the sensor's pressure output is converted into the more intuitive effective deflection, where effective deflection changes of 3.5 pm can be distinguished. A Kapton tape mask is applied by hand, to prevent electrical shorts that could arise from depositing metals on the device.

## 3.2 Measurement set-ups

This section examines the measurement set-ups that are used in this project. The most prevalent set-up is the uniform magnetic field set-up, which is used in all magnetic field related measurements. These consist of the magnetically-induced deflection measurements, where the magnetic field strength and angle are varied. Other measurement set-ups include the pressure tank, Dektak stylus profilometer and MOKE set-ups.

### 3.2.1 Uniform magnetic field set-up

The uniform magnetic field set-up is used to investigate the effect of torques on the membrane, which is measured as an effective deflection of the membrane. The set-up is able to vary a magnetic field from $-2$ T to 2 T, and has one free rotation axis that can be used to rotate the measured device with respect to the magnet. In this manner the field $\boldsymbol{H}$ and angle $\alpha$ can be varied, similar to the theory and modelling of Chapter 2 and Chapter 4.

An electromagnet is used to precisely control the magnetic field, which is shown in Figure 3.5. The photo displays two electromagnetic coils, encased in black, with two additional flat-cone shaped magnetic-pole pieces in dark brown. A sample holder rod is also present, which is inserted from above. Figure 3.5b shows a schematic of the electromagnet configuration. It consists of two electromagnetic coils, through

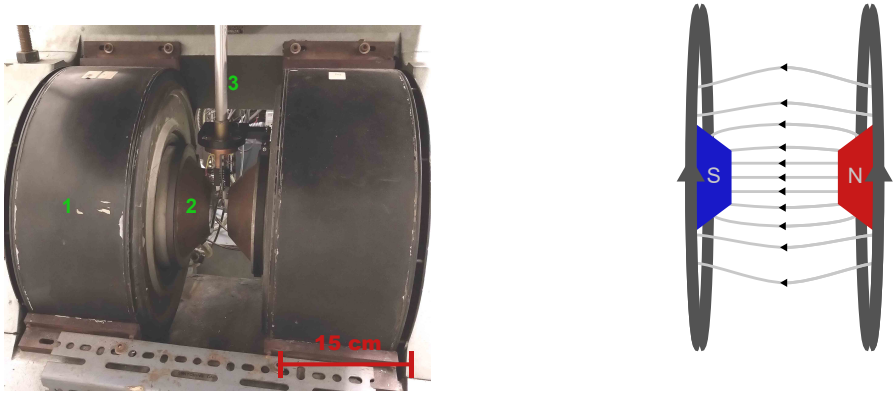


(a) (b)

Figure 3.5: (a) Photo of the electromagnet (1,2), including the rotation rod (3). The electromagnetic coils are encased in black (1), with the pole pieces shown in dark brown (2). (b) Schematic of the electromagnet. It includes the coils in dark grey, the pole pieces in red and blue, and the generated magnetic field is denoted by light grey lines.

which current is led, to generate a parallelly aligned magnetic field. The two pole pieces, with high permeability, are added to guide the magnetic field, creating a relatively large area where the magnetic field is uniform. The letters N and S denote if the pole piece acts as magnetic north or south pole, which switches with the magnetic field from the coils. During measurements the magnetic field is measured with a hall probe, that is attached to one of the pole pieces. While the magnetic field is close to uniform, the field strength is slightly lower at the centre, where the measured device is, compared to the poles where the hall probe measures the field. In order to measure the magnetic field at the measured device, a correction factor is taken into account.

The device is inserted between the magnetic pole pieces on a sample holder rod, which is shown up close in Figure 3.6. The sample holder consists of a rod, a wire connection from the device to the computer, and an extra hinge to which the device is connected. Figure 3.7 is a schematic of the sample holder illustrating its orientation between the magnetic pole pieces. The sample holder is attached to a rotation piece, which can rotate around its own axis, and thus change the angle between the device and the magnetic field. This rotation controls the angle $\alpha$ between the magnetic film's easy-plane and the external magnetic field $\boldsymbol{H}$. It should be noted that the rotation of the rod gains a small random offset when inserting it between the pole pieces. The connection of the rod and the rotation piece is not tight enough, which means that handling of the rod can introduce offsets on the order of a degree. These small offsets are corrected for in the results of Chapter 5, by setting the maximum deflection at the expected 90°, which at the worst are shifts of 2°. This correction remains the same for all measurements of the same device, as the rotation rod is not removed in between measurements.

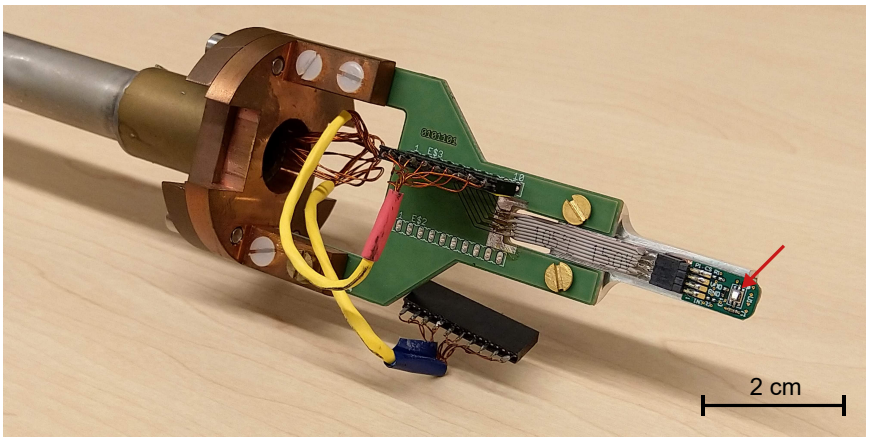


Figure 3.6: Photo of the sample holder, including a device. Note that the sensor on the device, as denoted by the red arrow, is shiny due to the metallic deposition layer.

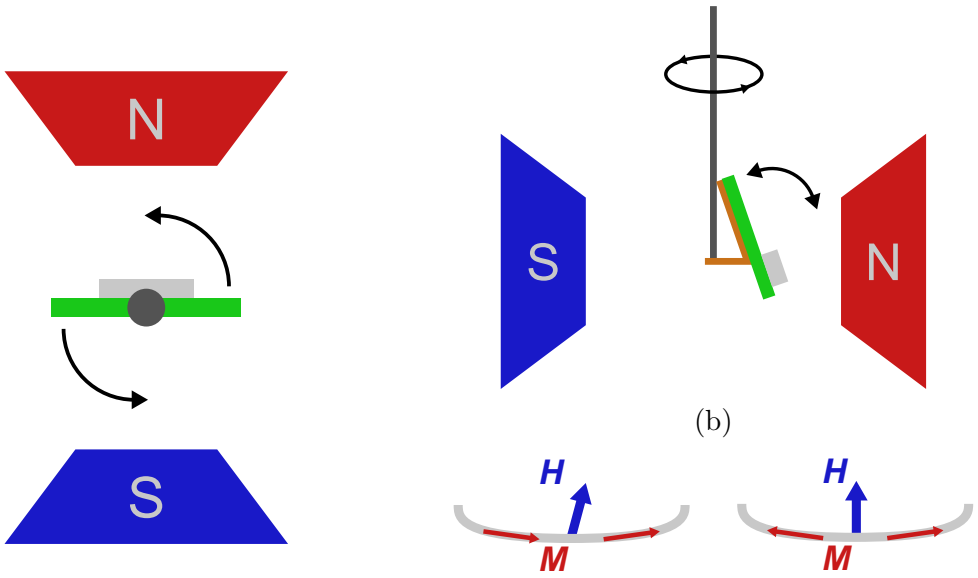


Figure 3.7: (a) Top down illustration of the measurement set-up, where the rotation rod is inserted between the two pole pieces. (b) Side view of the set-up, where the dark orange hinge can be adjusted to reduce tilting. (c) Magnetisation orientation for a tilted device. (d) Magnetisation orientation for a perpendicular device.

The connection of the sample holder to the device PCB is not perfect, and as such there can be a slight tilt of the device. The hinge, as illustrated in Figure 3.7b, is added to compensate for tilting of the device. It is important to reduce this tilting when measuring, especially when investigating perpendicular magnetic fields. In Section 2.2 and Section 4.2.2, the proposition is made that the magnetisation orients itself along the projection of the external field onto the easy-plane. Figures 3.7c and 3.7d illustrate the magnetic orientation for a tilted and perpendicular device. If a tilt is present, the external field is simply projected along this tilt. This is not the intended measurement and as such the tilt should be limited. In order to measure perpendicular magnetic field states, like shown in Figure 2.8b, the tilt should be confined to angles smaller than the slope of film. The hinge is used to correct the tilt with an accuracy of approximately 0.2°. This is just enough, as the pressure-induced deformation slope of the film is of a similar order, which is shown in the measurements of Section 5.1.1.

It should be noted that the entire set-up is in an air-conditioned room. This means that the pressure can fluctuate on the order of several hundreds of Pa over a day. The device is still a pressure sensor, and as such this fluctuation is measured, adding an unwanted pattern to the measurements. In addition, sharp peaks in the measurement are seen when doors are opened or closed, as the pressure temporarily spikes. This is a testament to the resolution of the device, as closing/opening doors that are several tens of meters away are clearly visible as spikes in the pressure. To resolve these unwanted signals, a reference pressure sensor is added to the set-up, away from the magnetic field. This reference pressure is subtracted from the intended measurement, removing any spikes or slow changes of the ambient pressure.

All components are connected to the same computer, from which a custom LabVIEW program controls them and retrieves measurement data. These components include the electromagnet, the rotation rod, the reference pressure sensor and the device on which the magnetically-induced deflections are measured.

### 3.2.2 Pressure tank set-up

The pressure tank set-up is normally used to calibrate the capacitive pressure sensor. However, in this work it is used to investigate the increase of the membrane stiffness caused by the added magnetic layer.

The pressure tank set-up consists of a closed vessel, within which the pressure and temperature are regulated. Multiple capacitive pressure sensors can be put into the vessel and measured at the same time, where they are compared to a high precision pressure sensor reference. Calibration measurements, as shown in Figure 3.8, can be done by sweeping the pressure inside the vessel, and comparing the output capacitance to the pressure reference. Similarly temperature dependent calibrations can be done as the capacitive pressure sensor includes a temperature sensor. These calibrations are necessary because the temperature influences the stress in the membrane. The temperature calibration brings the pressure error, due to fluctuations of the temperature, down from approximately 20 Pa/°C to 1 Pa/°C. In terms of the effective deflection this reduces the fluctuation from 70 pm/°C to 3.5 pm/°C.

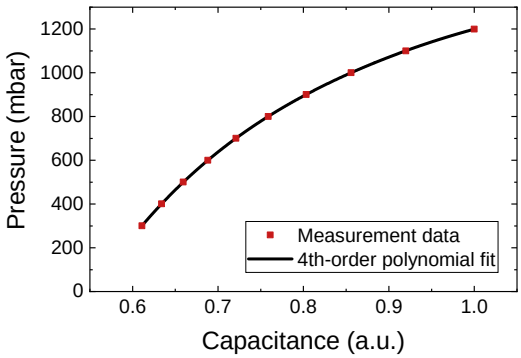


Figure 3.8: Graph of the pressure, as measured by the reference sensor, set out against the capacitance, as measured by the capacitive pressure sensor. The calibration is done by a fourth-order polynomial fit, used to convert the sensor's capacitance output into pressure output. This is a repetition of Figure 2.2d.

In this work the pressure tank set-up is used to measure the deviation in pressure output after magnetic deposition. The added magnetic layer changes the stiffness of the membrane. Because the sensors were calibrated before deposition, the pressure output is no longer correct, as the new stiffness is not taken into account. By repeating the calibration measurements, the deviation in output pressure compared to the reference sensor can be investigated. This give insight into how the stiffness and sensitivity of the membrane have changed, and are investigated in Section 5.3.1. Note that an increase in stiffness does not change the effective deflection calibration, as the deflection is directly coupled to the capacitance. However, the amount of deflection per applied pressure does decrease.

### 3.2.3 Dektak stylus profilometer set-up

The Dektak stylus profilometer set-up is used to measure the pressure-induced deformation of the membrane. The deformation profile along the short- and long-axis can be verified and the maximum deflection and slope can be measured at ambient pressure.

The Dektak stylus profilometer is, as the name suggests, a profilometer that utilises a stylus or needle. The working principle is illustrated in Figure 3.9. It shows a stylus moving in a single direction along the surface. The stylus is kept in contact with the surface during scans, where a constant force is applied to the surface. This applied force is held constant with the help of a feedback loop. While in contact, the stylus is dragged along the surface to measure the profile. The actual height measurement is determined from the feedback loop, as it needs to compensate for changes in the profile. The Dektak profilometer measures the height profile along a single line, which it can measure repeatedly to average the profile. It must be noted that the measurement has some artefacts, which are caused by the feedback loop. In the illustration this is seen where the stylus encounters a sudden large change in height, a step. At this step the feedback loop will have to respond quickly, which results in an overcompensation of the stylus. Consequently, the measured height

will first overshoot its intended value, after which the feedback loop stabilises again. These artefacts can be reduced by slowing down the scanning speed of the stylus along the surface, giving more time for the feedback loop to react. The force with which the stylus presses onto the membrane is minimal, compared to the force due to atmospheric pressure. As such, the deformation profile is not significantly disturbed by the measurement.

In the measurements, the profilometer will be used to measure the height profile along the short- and long-axis of the membrane, as illustrated in Figure 3.9a. The deformation profile is measured at atmospheric pressure. From this data the pressure-induced bathtub-like deformation profile can be verified. Moreover, the maximum deflection and slope can be determined for atmospheric pressure. The maximum deflection is used to determine the calibration factor for the effective deflection, as was described in Section 2.1. The profilometer performs line-scans, which are not perfectly aligned with the membrane axes. Because of this, a measurement always includes parts of both the short- and long-axis profile. For short-axis measurements this is negligible, as the long-axis profile remains the same for a wide part of the membrane. However, it is hard to do proper long-axis scans, as the line-scan does not align perfectly with the membrane and does not go exactly through the middle of the membrane. It is thus better to look at the short-axis scans when determining the maximum deflection. The slope plays an important role in investigating perpendicular magnetic fields, as was discussed in Section 2.3.1 and will be further discussed in Section 4.2.2.

Unfortunately the resolution of the profilometer is too low to investigate the magnetically-induced deflections, and thus only the atmospheric pressure deformation profile is investigated. In Chapter 5 the resulting profiles are compared to the deformation profiles of the COMSOL model.

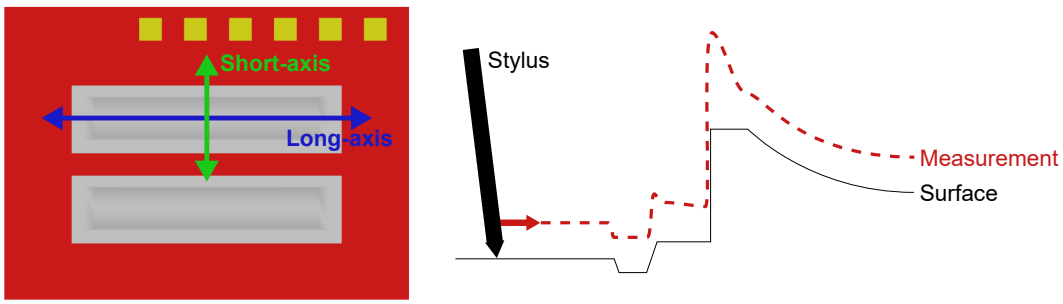


(a) (b)

Figure 3.9: (a) Top view of the sensor, with the two membranes drawn in grey. The short- and long-axis are denoted by the green and blue arrow respectively. (b) Working principle of a stylus profilometer. The stylus, in black, is dragged along the surface. The surface is measured through the feedback of the stylus, resulting in the dashed red line profile. The measurement has artefacts near steep or sharp changes in height.

### 3.2.4 MOKE set-up

The MOKE set-up is used to measure magnetic hysteresis loops of the magnetic film. MOKE stands for the magneto-optic Kerr effect. This effect describes how the polarisation of light changes, when it reflects off the surface of a magnetic material. When polarised light reflects off a magnetic surface, it's polarisation can rotate and change in ellipticity. This can be used to qualitatively probe changes of the magnetisation, as the polarisation is proportional to the magnetisation direction.

In the set-up, the magnetisation is changed by an external magnetic field, that is generated by an electromagnet. The magnetisation change is measured as a MOKE signal as function of external field, where the MOKE signal is either a rotation or ellipticity change. This results in hysteresis graphs, like the ones shown in Figure 3.10. These are examples of an easy- and hard-axis loop, as were introduced in

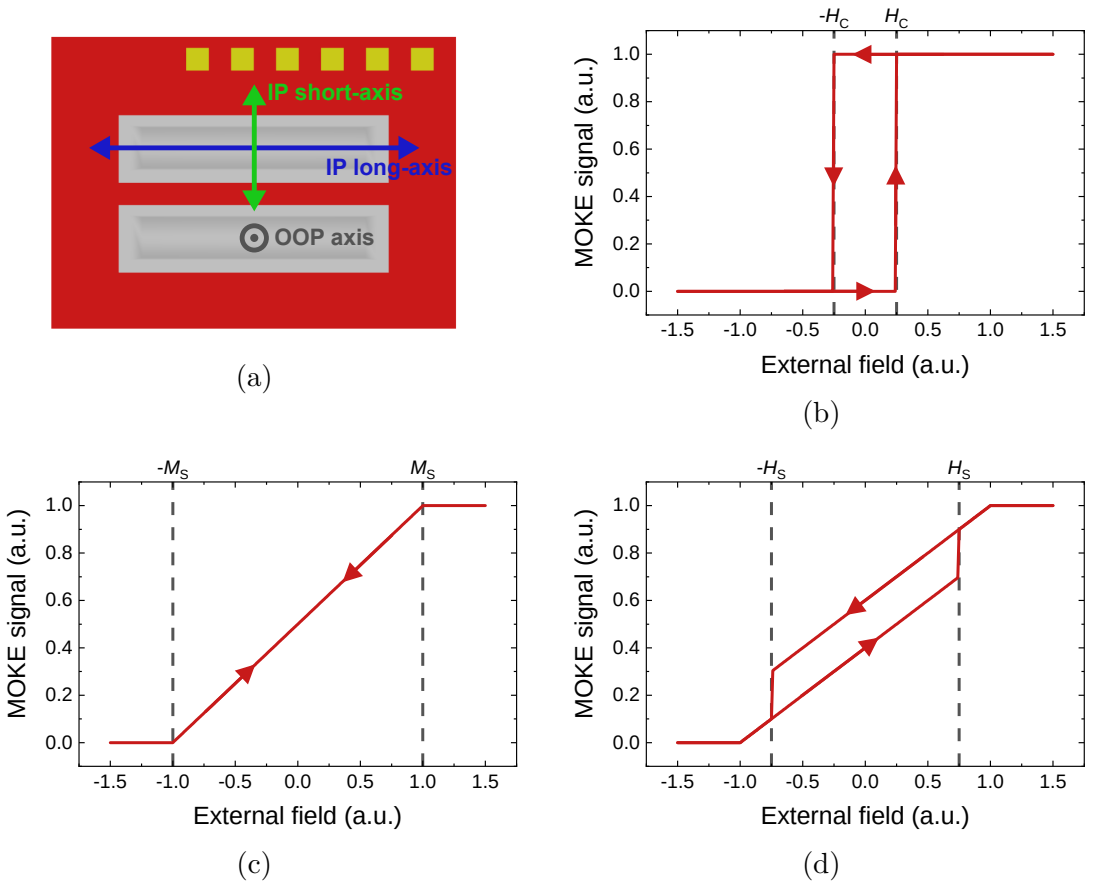


Figure 3.10: Example hysteresis loops, where the external field is swept along an easy- or hard-axis. (a) Overview of the in-plane (IP) short-axis, IP long-axis and out-of-plane (OOP) axis. (b) Easy-axis sweep, showing a sharp hysteresis loop. The magnetisation switches at the coercive field $H_C$. (c) Hard-axis sweep. The magnetisation follows the external field, saturating when the external field reaches the saturation magnetisation. (d) Hard-axis sweep with easy-axis component. The easy-axis is probed by a projection of the external field onto the easy-axis. As such, there is a partial switch of the magnetisation at a switching field, denoted by $H_S$, which is larger than the coercive field of (b).

Section 2.2.3. Note that the y-axis shows the MOKE signal in arbitrary units, for without calibration the signal only gives qualitative information about the magnetisation.

The MOKE set-up is used in order to confirm the magnetic easy-plane and quantify the coercivity of the magnetic film. This is done with the help of three hysteresis measurements, where the external field is swept along a specific axis of the membrane. The first sweep is along the in-plane (IP) short-axis of the membrane, which should be an easy-axis loop with a small coercivity. Similarly, a measurement is done along the IP long-axis that should be an easy-axis loop as well. If both the short- and long-axis are magnetic easy-axes with small coercivity, it can be concluded that it is an easy-plane, for the magnetisation can easily switch from one axis to the other. Lastly, an out-of-plane (OOP) hysteresis loop is measured, which should be a hard-axis loop. In Section 5.1.2, the results of these measurements are shown and discussed.

Figure 3.10 shows ideal easy- and hard-axis loops. However, in measurements the external field, with which you change the magnetisation, is never perfectly aligned with the sample. This means that you never probe purely one axis, but others as well to a lesser extent. For the OOP hard-axis measurement this means that there is also a, relatively, small IP projection of the external field. Because only a small part of the total field is projected in the plane, the field at which hysteresic effects are seen is greatly increased. As such, the typical easy-axis hysteresis loop switch is seen in hard-axis measurements at much higher magnetic fields, as illustrated in Figure 3.10d. The projection of the field is not a problem for the easy-axis measurements, as the projected hard-axis has no switching.

# 4
# Modelling

In this chapter the numerical and finite-element models are presented. The goal is to provide insight and investigate the qualitative behaviour of the magnetic film under influence of a uniform external magnetic field. The first section is an extension of the theory, where numerical solutions of the magnetisation angle $\theta$ and the torque are determined according to the Stoner–Wohlfarth model. The torque is an indication of the force applied to the magnetic film, which results in a magnetically-induced deflection. The second section introduces the finite-element model, that describes the deformation profile of the membrane under influence of a pressure load and the Maxwell stress. The developed model combines the pressure deformation, Stoner–Wohlfarth model and the Maxwell stress to determine the magnetically-induced deformation profile. Finally, the model imitates the measurements of Chapter 5 by determining the effective deflection. This is done by measuring the capacitance of the model and doing the right calibrations, similar to real devices, to get the effective deflection. In this manner a direct comparison can be made between the finite-element model and the measurements. The numerical models are made with MATLAB [16], of which the scripts can be found in Appendix B. The finite-element models are made with COMSOL Multiphysics [18].

## 4.1 Numerical simulations of the magnetisation & torque

The magnetisation angle $\theta$ is an important parameter for determining the forces on the magnetic film, such as the magnetic torque and the Maxwell stress, that result in an effective deflection of the magnetic film. In the Theory chapter, the angle $\theta$ was determined by solving equation 2.7 analytically for the specific case $\alpha = 90°$. In this section the results of solving the equation numerically are presented for arbitrary $\alpha$. The angle $\theta$ is then used to calculate the torque, using equation 2.10, which presents insight into the qualitative behaviour of the force and magnetically-induced deflections. The equations 2.7 and 2.10 are repeated here for ease of use:

$$\sin(\alpha - \theta) = \frac{M_S}{H} \sin\theta \cos\theta, \tag{4.1}$$

$$\tau = \mu_0 V M_S H \sin(\alpha - \theta). \tag{4.2}$$

Figures 4.2b and 4.2c show the numerical results for $\theta$ and $\tau$ respectively.

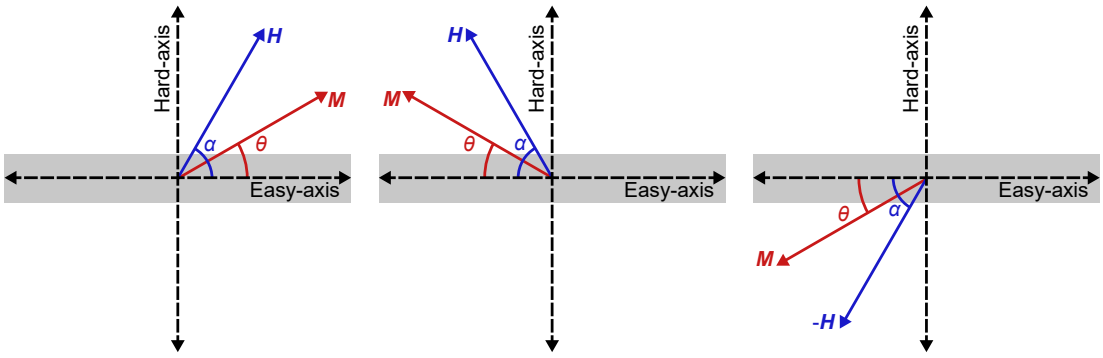


(a) (b) (c)

Figure 4.1: The magnetisation angle $\theta$ and external field angle $\alpha$, with respect to the magnetic easy-axis. The range of $0° < \alpha < 90°$ gives a complete overview of the behaviour of $\theta$. (a) $0° < \alpha < 90°$. (b) $90° < \alpha < 180°$. (c) $0° < \alpha < 90°$, with negative field $-H$.

In order to solve equations 4.1 and 4.2, the unsolved parameters $\mu_0$, $M_S$, and $V$ must be known, where the variables $H$ and $\alpha$ are varied. The parameters are chosen such that they are comparable to the devices used in the measurements of Chapter 5. Here $\mu_0$ is simply the vacuum permeability. The saturation magnetisation $M_S$ is set to 1.36 T, the saturation magnetisation of the magnetic CoB film [15]. The volume $V$ is determined by the membrane area and magnetic film thickness. The membranes in this project are 175 $\mu$m by 700 $\mu$m, with a typical magnetic film thickness of 100 nm. The external field $H$ is varied from 0 T to 2 T and the angle $\alpha$ is varied from 0°, in-plane, to 90°, out-of-plane. Only positive fields between 0° and 90° are modelled because the overall behaviour of the magnetisation angle $\theta$ and torque is the same for negative fields or larger angles. This is illustrated in Figure 4.1, where the angle $\theta$ repeats itself for larger angles and negative fields.

Figure 4.2b shows the results of numerically solving $\theta$ using the described parameters, for a set of angles $\alpha$ as function of the external field $\boldsymbol{H}$. Looking at the graph, it is clear that for $\alpha = 0°$ the angle $\theta$ is 0° for all fields. This angle $\alpha$ aligns with the easy-axis and thus the magnetisation follows it exactly. For non-zero external field angles $\alpha$, an asymptotic behaviour is seen where the magnetisation angle $\theta$ approaches $\alpha$. Note that, except for $\alpha = 90°$, the angle $\theta$ has not reached $\alpha$ yet at the saturation field of 1.36 T. The reason for this is the demagnetisation field $\boldsymbol{H_d}$, which tries to counteract the hard-axis component of the magnetisation. This results in the projected effective field $\boldsymbol{H_e} = \boldsymbol{H} + \boldsymbol{H_d}$, which is illustrated in Figure 4.2a. The magnetisation aligns parallel to the field $\boldsymbol{H_e}$, which implies the asymptotic behaviour of $\theta$. For the specific case that $\alpha = 90°$, $\boldsymbol{H_d}$ is parallel to $\boldsymbol{H}$ and thus the effective field $\boldsymbol{H_e}$ is aligned with the external field $\boldsymbol{H}$. The magnetisation then fully aligns with $\boldsymbol{H}$ when $H > H_d$, i.e. $H > 1.36$ T.

Substituting equation 4.1 into equation 4.2 results in the following torque that only depends on $\theta$:

$$\tau = \mu_0 V M_S^2 \sin(\theta)\cos(\theta). \tag{4.3}$$

Figure 4.2c shows the results from plugging the solutions of $\theta$ from Figure 4.2b into

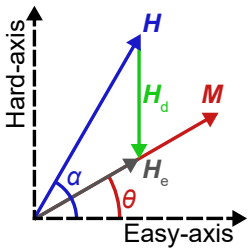


(a)

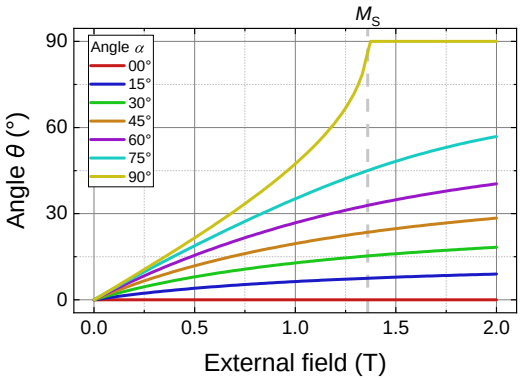


(b)

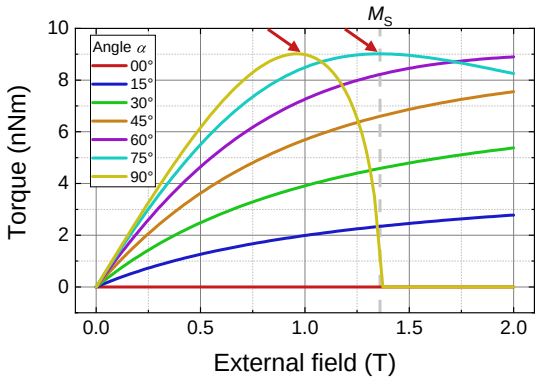


(c)

Figure 4.2: (a) Illustration of the effective field $H_e$ resulting from the external field $H$ and the demagnetisation field $H_d$. The magnetisation aligns with the effective field, resulting in a $\theta$ that is lower than $\alpha$. (b) Numerical solutions of $\theta$ as function of field $H$ for different $\alpha$. The angle $\theta$ approaches $\alpha$ asymptotically, except for $\alpha = 90°$ where it fully aligns above the saturation magnetisation $H > M_S = 1.36$ T. (c) Numerical solutions of the torque, determined by entering the value of $\theta$ into equation 4.3. The optimal torque occurs at $\theta = 45°$, which is reached for $\alpha$ equal to 75° and 90°, as emphasised by the red arrows.

equation 4.3. By maximising the equation, an optimal torque is found at the angle $\theta = 45°$. The optimal torque is an important result, as at this point the force that is applied to the membrane is the strongest, and thus the highest effective deflection should be observed. From both figures it can be concluded that the optimal torque only occurs for $\alpha$ between 75° and 90°, within the range of 2 T, as indicated by the red arrows. For angles $\alpha > 45°$ the optimal torque can be achieved, however, the field at which they do can become enormous due to the asymptotic behaviour of $\theta$. Figure 4.3 shows the field necessary to get the optimal torque, where $\theta = 45°$, as function of the angle $\alpha$. The magnetic field $H$ and angle $\alpha$ can thus be optimised to gain the highest torque, which results in the strongest force and effective deflection. For the perpendicular field $\alpha = 90°$ the torque drops to 0 when $H > M_S = 1.36$ T. This drop is caused by the fact that at this point the magnetisation and external field are completely aligned, and thus there is no longer any torque.

In Section 2.3.1 an approximate force of the maximum torque was calculated for the analytical solution, where $\alpha = 90°$. Note that the same maximum torque is achieved in the numerical solution. The numerical solutions have shown that this maximum torque is also achieved for angles $\alpha > 45°$. It is however good to note that, while

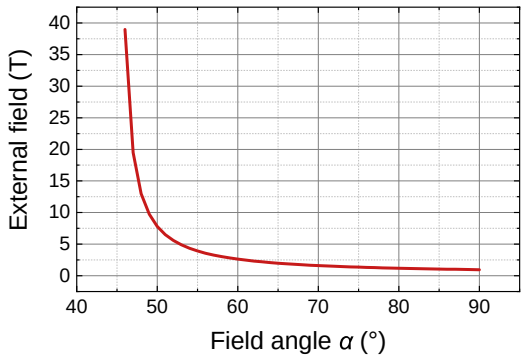


Figure 4.3: The required external field $H$ for the optimal torque, as function of the field angle $\alpha$. It diverges as the angle approaches 45°, where an infinite field is required at 45°. The required field is on the order of 1 T, for most of the range shown.

the torque is an indication of the force that is applied on the membrane, it is not an exact representation of the effective deflection readout. Section 2.3.1 already alluded to the idea that the deformation is anti-symmetric for arbitrary angles and symmetric for a perpendicular field. This means that while maximum torque is achieved at angles $\alpha$ above 45°, the resulting effective deflection will be largest for the symmetric deformation at 90°.

In short, the numerical solutions of the torque depict its qualitative behaviour, which is an indication of how the resulting effective deflection behaves. The torque is maximised when the magnetisation angle $\theta$ equals 45°, which for perpendicular external fields is expected at 0.97 T. The MATLAB script used in this section can be found in the appendix, Section B.1.

## 4.2 Finite-element models of the membrane & magnetic film

Finite-element modelling in COMSOL Multiphysics is used to simulate the magnetically-induced effective deflection measurements and visualise the deformation profile. In order to compare the model directly to measurements, the model determines the effective deflection from calibrating the sensor's capacitance output, similar to what is done for the actual devices. The first section describes the pressure and mechanical deformation part of the model, including the calibration of the capacitance output. The model requires a large selection of other parameters, e.g. the geometrical shape, which will be presented as well. The second section discusses the magnetic film model in detail, including the magnetisation orientation, the magnetically-induced deformation and the calibrated effective deflection. In the magnetic model the magnetic field strength, field angle, and magnetic layer thickness are varied, similar to the measurements. The results of the model are compared to the measurements in Chapter 5.

### 4.2.1 Pressure-induced deformations & effective deflection calibration

The model simulates a flexible membrane that is clamped on its perimeter, as is illustrated in Figure 4.4. In the model only the top membrane is simulated, without the bottom electrode or the cavity, because all information is in the deformation profile of the top membrane. Knowing the size of the cavity gap, one can calculate the capacitance simply from the deformation profile of the top membrane, as was detailed in Section 2.1. The sensor's pressure output and effective deflection are in turn derived from the capacitance by calibrating the device.

In this part of the finite-element model, referred to as the pressure model, the deformation is investigated as function of a pressure load, that is applied to the top of the membrane. The goal is to calibrate the effective deflection from calculating the capacitance of the membrane as function of the applied pressure. The deformation profile is shown in Figure 4.4, with an applied pressure of 1000 mbar, close to atmospheric pressure. The shape is similar to that of a bathtub, where the maximum deflection is hampered by the shortest axis of the membrane. Note that the deflection is scaled up by a factor 100 to be visible. In this simulation the maximum deflection is 360 nm on a 700 $\mu$m long membrane. In comparison, this deflection is similar to a 1 m long table being deflected by 0.5 mm, which would be hardly visible by eye.

In order to get to the deformation of Figure 4.4, different model parameters need to be defined. The width and length of the membrane are set to 175 $\mu$m and 700 $\mu$m respectively, similar to the numerical simulations. The layers of the membrane

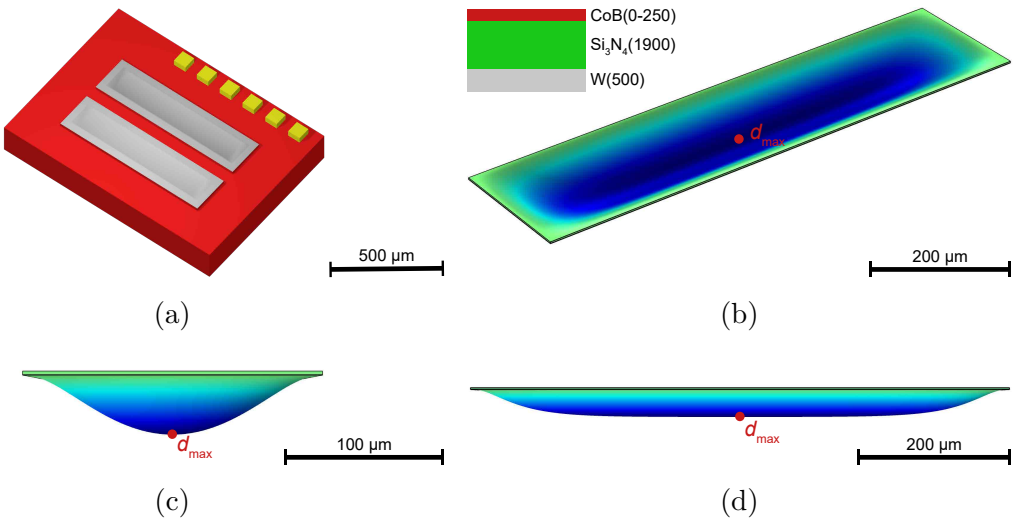


Figure 4.4: Visualisation of the model with a 1000 mbar pressure load. The deflection is increased by a factor 100 to be visible. The membrane is 175 $\mu$m by 700 $\mu$m, with a maximum deflection of 360 nm at $d_{max}$. (a) Overview of the sensor, with two membranes shown as grey rectangles. (b) Overview of the deformed membrane, with an inset of the membrane composition and layer thickness in nm between parentheses. The CoB layer is set to 0 nm for this specific simulation. (c) Front view. (d) Side view.

| Material | $\rho_m$ [kg/m$^3$] | $E_Y$ [GPa] | $\nu$ [1] |
|---|---|---|---|
| Tungsten (W) | 19,350 | 140 | 0.22 |
| Silicon nitride ($Si_3N_4$) | 3,100 | 200 | 0.23 |
| Cobalt (Co) | 8,900 | 209 | 0.31 |

Table 4.1: The mass density ($\rho_m$), Young modulus ($E_Y$) and Poisson ratio ($\nu$) of the materials used in COMSOL simulations [19, 20]. The mechanical properties of Co are used instead of CoB, for properties of Co are readily accessible, in contrary to those of CoB.

are composed of a 500 nm tungsten (W) layer, a 1900 nm silicon nitride ($Si_3N_4$) layer, and a cobalt boron (CoB) layer with thicknesses varying from no CoB to 250 nm CoB. These materials and thicknesses represent the devices that are made by AMS [19], including the added magnetic layer, and used in measurements. The W layer acts as the top electrode in the parallel plate configuration of Section 2.1, with the $Si_3N_4$ layer as cover protecting the electrode. The CoB layer acts as the magnetic layer, which in the next section is modelled in more detail. For the examples shown in this section there is no CoB layer.

The W and $Si_3N_4$ layers are very flexible, too flexible in fact for the original purpose as pressure sensor at atmospheric pressures. To reduce the flexibility the W layer is stretched out, where it experiences 1600 MPa of tensile stress, making the membrane more stiff. The $Si_3N_4$ layer partially relieves this stress, as it experiences a 100 MPa compression [19]. For capacitance calculations the cavity gap is set to 850 nm [19]. In real devices the stresses and cavity gap can deviate a bit, due to fabrication quality and precision, changing the stiffness and deflection. However, this is corrected through calibration, resulting in all devices outputting the correct pressure value and corresponding effective deflection.

To be able to solve the mechanical equations governing the deformation, three material properties are needed, the mass density ($\rho_m$), the Young modulus ($E_Y$) and the Poisson ratio ($\nu$). Table 4.1 notes the values used in this model. Note that the mechanical properties of Co are used instead of CoB. This choice is made because the properties of Co are readily available, while the mechanical properties of CoB are rarely investigated or reported [21].

Figure 4.5 shows the calibration of the sensor's output pressure and effective deflection for a model without the CoB layer. The capacitance is calculated according to equation 2.1, where the deflection is integrated over the surface. The electrode distance is determined as the cavity gap subtracted by the deflection, formulated as $r(x, y) = g - d(x, y)$. The graph of Figure 4.5b is made by sweeping the applied pressure from 0 mbar to 1500 mbar. The pressure calibration is done by regression of a 4th order polynomial, as was described in Section 2.1. This results in a pressure output function of the following form:

$$P(C) = a_4C^4 + a_3C^3 + a_2C^2 + a_1C + a_0, \tag{4.4}$$

where $C$ is the capacitance and $a_i$ the corresponding fit parameters. The effective deflection is determined by the linear regression of the maximum deflection as

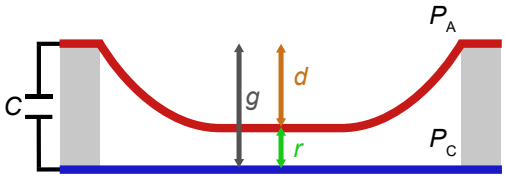


(a)

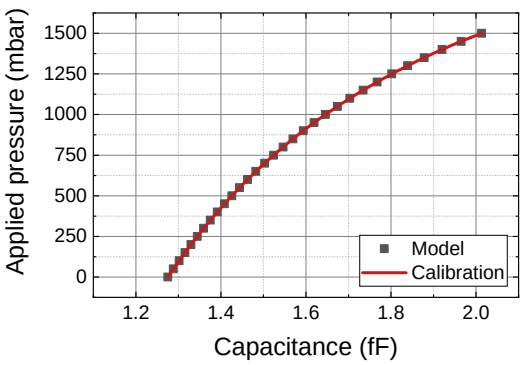


(b)

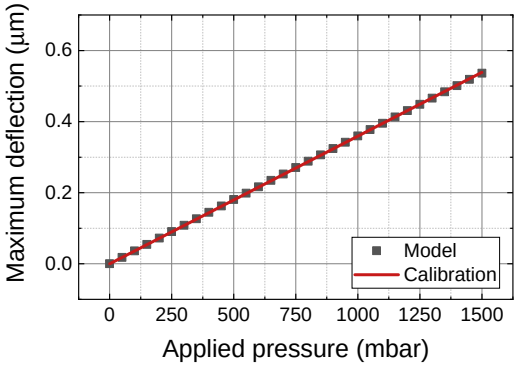


(c)

Figure 4.5: Calibration of the sensor's output pressure and effective deflection. (a) Overview of the capacitive pressure sensor, with $g$ the cavity gap, $d$ the deflection and $r$ the distance between the electrodes. (b) Graph of the applied pressure and simulated capacitance. The calibration of the sensor's output pressure is determined by a 4th order polynomial regression of the applied pressure as function of the capacitance. (c) Graph of the simulated maximum deflection as function of the pressure from (b). The calibration of the effective deflection is determined by a linear regression of the maximum deflection as function of pressure.

function of the output pressure, which is formulated as follows:

$$d(C) = \beta P(C). \tag{4.5}$$

Here $\beta$ is the linear conversion factor from the output pressure to the effective deflection, as illustrated in Figure 4.5c. This regression implies that, for bathtub-like deformations, the effective deflection is equal to the maximum deflection. This is not necessarily true for magnetically induced deflections, where the deformation can be anti-symmetric, resulting in lower capacitance (and effective deflection) outputs. It is thus good to note that the effective deflection can be lower than the actual deflection. The conversion factor, which represents the amount of effective deflection per pressure, is 3.6 pm per Pa in this model.

In short, the pressure model shows the expected bathtub-like deformation, with a maximum deflection of 360 nm near atmospheric pressure. The sensor's output pressure and effective deflection are calibrated by measuring the capacitance and maximum deflection, as function of an applied pressure.

### 4.2.2 Magnetisation orientation & deflection of the magnetic film

In this section the magnetic film model is described, with emphasis on the magnetisation orientation and magnetically-induced deformation of the film. At the end, some preliminary results are shown for the magnetically-induced effective deflection, using the calibration of the pressure model from the previous section. The magnetic film model is made in COMSOL Multiphysics, which is supported by a lookup table.

In contrast to the pressure model, the magnetic film model consists of only one layer. Instead of modelling the membrane as a 3-layer stack of $W/Si_3N_4/CoB$, the membrane is modelled as a single CoB layer. This choice is made because of the inherit problems that arise when meshing multiple flexible thin layers that can deform. In order to model the magnetic field, the area directly surrounding the membrane needs to be meshed as well. Due to the high aspect ratio of the film, there is an abrupt change in mesh quality going from the film to the surrounding area. In combination with a deforming mesh this results in a mesh of low quality, which cannot describe the magnetic field properly. These effects are reduced by modelling the membrane as a single layer, where an effective stress is used to simulate mechanical properties of the 3-layer stack. The effective stress is chosen such that the response to pressure is the same between the magnetic film model and the pressure model, including the magnetic layer. The results shown in this section are for a typical 100 nm thick CoB layer. The mechanical properties of pure Co are used instead of CoB, as was already discussed in the previous section.

An iterative process, consisting of multiple steps, is used in simulating the magnetisation orientation and deformation of the magnetic film, as is illustrated in the flow diagram of Figure 4.6. In this process, the magnetisation orientation is determined for each finite-element individually, as if it locally were a uniform magnetised domain. The Maxwell stress is derived from the magnetisation orientation, external magnetic field and demagnetisation field, resulting in the magnetically-induced deformation.

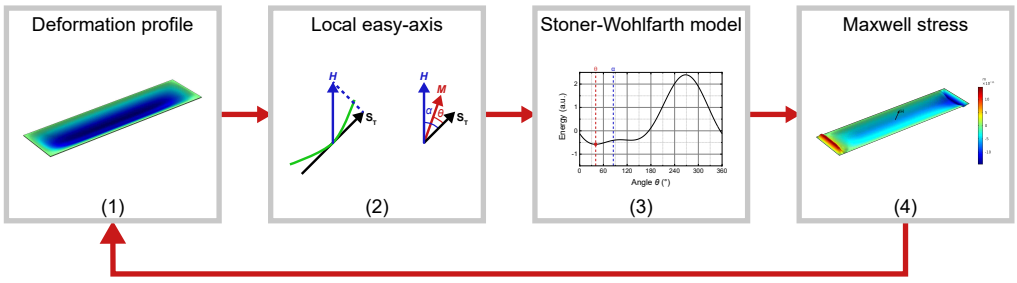


Figure 4.6: Flow diagram of the magnetic film model. The pressure-induced deformation profile (1) is used to determine the local easy-axis (2). The magnetisation angle $\theta$ is calculated with the Stoner–Wohlfarth model (3), using the external field and local easy-axis. The Maxwell stress (4) is determined from the magnetisation orientation, which alters the deformation profile (1). Only a few iterations are necessary, as the magnetically-induced deformation is only minor compared to the pressure-induced deformation.

The first step in the process is the initial, pressure-induced, deformation. The pressure-induced bathtub-like deformation profile, as was shown in Figure 4.4, is used to determine the magnetic easy-plane. As described in Section 2.2.2, the easy-plane of a bent thin film is parallel to the thin film at every point. The easy-plane is derived from the surface tangent of the deformation profile, as is illustrated in Figure 4.7a. The easy-plane can be simplified to a local easy-axis, as the magnetisation wants to align with both the external field and the easy-plane, which forms a single plane of rotation. The local easy-axis direction is determined from the projection of the external field $\boldsymbol{H}$ onto the surface tangent. The local magnetisation will be oriented to be somewhere on the plane spanned by $\boldsymbol{H}$ and the local easy-axis.

The next step is to derive the exact magnetisation angle $\theta$, which depends on the field strength and field angle $\alpha$. This is done according to the Stoner–Wohlfarth model of Section 2.2.3. The magnetisation angle $\theta$ is determined by finding the global minimum of the magnetic energy landscape. Note that this neglects hysteresis, where the angle $\theta$ can be a local minimum. An example energy landscape is illustrated in Figure 4.3. A lookup table of the optimal angle $\theta$, as function of field strength $H$ and field angle $\alpha$, is created with MATLAB and imported into the COMSOL model. The external field $\boldsymbol{H}$ and surface tangent are known in COMSOL, from which the local $H$ and $\alpha$ are determined. The lookup table is then used to determine the optimal magnetisation angle $\theta$ for each element.

The last step before iteration is calculating and applying the Maxwell stress, which results in a new deformation profile. The Maxwell stress is derived from the total magnetic field, which is determined by the magnetisation, external magnetic field,

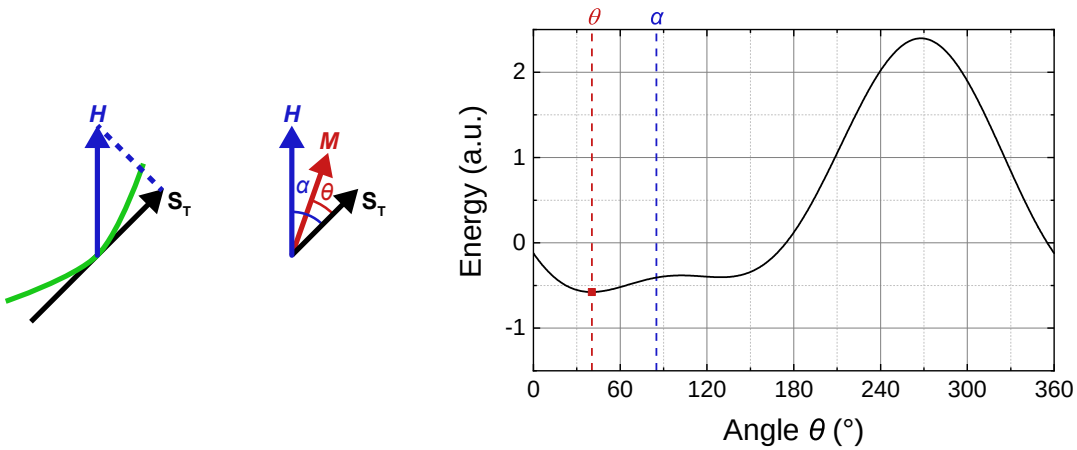


(a) (b)

Figure 4.7: (a) Schematic illustration of how the local easy-axis is determined from the projection of $\boldsymbol{H}$ onto the surface tangent $\mathbf{S}_\mathrm{T}$, the green line indicates the surface. The right image shows how the angles $\alpha$ and $\theta$ are defined in the Stoner–Wohlfarth model. (b) Example energy landscape of the Stoner–Wohlfarth model. The black line denotes the energy landscape, the red square the global minimum and the blue dashed line the external magnetic field angle $\alpha$.

demagnetising field and stray magnetic field. Out of these four only the external magnetic field is controlled. The magnetisation is derived, as explained above, and the demagnetising field and stray magnetic field are determined by COMSOL. The process of determining the local easy-axis, deriving the magnetisation and applying the Maxwell stress is repeated for each new deformation profile, until a stationary state is found. The result is a complete deformation profile, consisting of the pressure-induced deformation and magnetically-induced deformation. Only a few iterations are needed, as the magnetically-induced deformation is only minor compared to the pressure-induced deformation. The rest of this section discusses some of the results of the model, where perpendicular and non-perpendicular external fields are compared. In these examples the non-perpendicular field is always at a 60° angle with respect to the long-axis of the film.

Figure 4.8 shows the magnetisation orientation for perpendicular and non-perpendicular external fields, taking into account the pressure-induced deformation profile. The local easy-axis is determined by the projection of the external field $\boldsymbol{H}$ onto the film, where the magnetisation orientation $\boldsymbol{M}$ is determined by the Stoner–Wohlfarth model. Figure 4.8a illustrates the case for a non-perpendicular field, where there is a clear preference for the magnetisation to align along the long-axis of the film. Figure 4.8b depicts a perpendicular magnetic field. In this case the slope of the film determines the local easy-axis and magnetisation orientation, as the projection of the external field $\boldsymbol{H}$ will vary across the film. Figures 4.8c and 4.8d elaborate on this behaviour, showing the projections at different ends of the film. It also depicts that the general magnetic behaviour of a perpendicular field still holds at angles that differ from 90° within the film's slope of approximately 0.2°, as the projection of $\boldsymbol{H}$ onto the surface tangent stays similar. It is only when the field starts to deviate more than the slope, that the magnetisation will orient itself along a single direction. The insets of figures 4.8a and 4.8b depict a general picture of magnetic domains and possible domain walls of the film.

In Figure 4.9 the magnetically-induced deflections corresponding to Figure 4.8 are shown. The pressure-induced bathtub-like deformation profile has been subtracted to shown only the magnetically-induced deformation profile. The general shape of the deformation aligns well with Figure 2.8 from the theory, where the effect of torque was investigated. This gives credence to the idea that the torque only deforms areas of the film that can reduce the total energy of the system, i.e. where the local easy-axis and external field can be better aligned by the torque. For non-perpendicular fields, this only deforms the ends of the film that are sloped along the same direction as the magnetisation, in this case the long-axis. Changing the slope at these ends is favourable, where the slope of the left end needs to be reduced and the slope at the right end needs to increase. This results in the anti-symmetric behaviour, where the left part is pushed upwards and the right part pushed downwards. In the case of a perpendicular field the magnetisation also has short-axis components, depending on the position on the membrane. Most of the area of the membrane has a slope along the short-axis, and as such the membrane is deformed more strongly. In this configuration the membrane always wants to push more downwards, such that the slope increases and the local easy-axis aligns better with the external field.

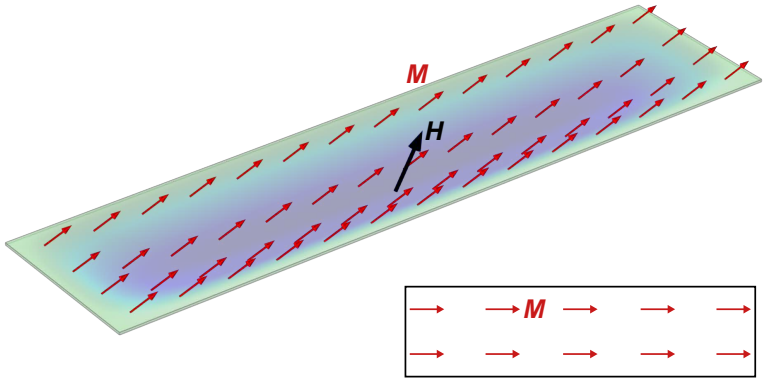


(a)

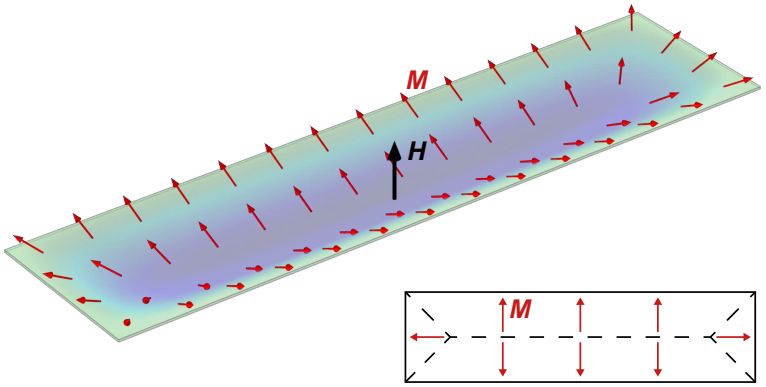


(b)

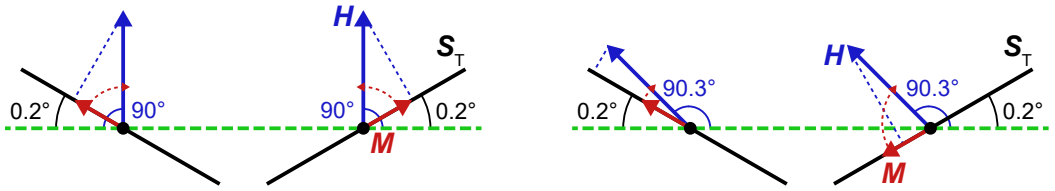


(c) (d)

Figure 4.8: Magnetisation orientation of films that are deformed by an applied pressure. The insets of (a) and (b) depict the film from above, with a schematic of possible magnetic domain walls indicated by the dashed lines. (a) Magnetisation orientation for a non-perpendicular external field at 60° with respect to the long-axis of the film. (b) Magnetisation orientation for a perpendicular external field, where the local easy-axis follows the slope of the film. (c) Depiction of how a perpendicular field results in a symmetric magnetisation. The red dashed arrows denote the rotation of the magnetisation, which would lead to a symmetric torque. (d) Depiction of how a slightly off perpendicular field already results in an asymmetric magnetisation. The red dashed arrows denote the rotation of the magnetisation, which would lead to an asymmetric torque.

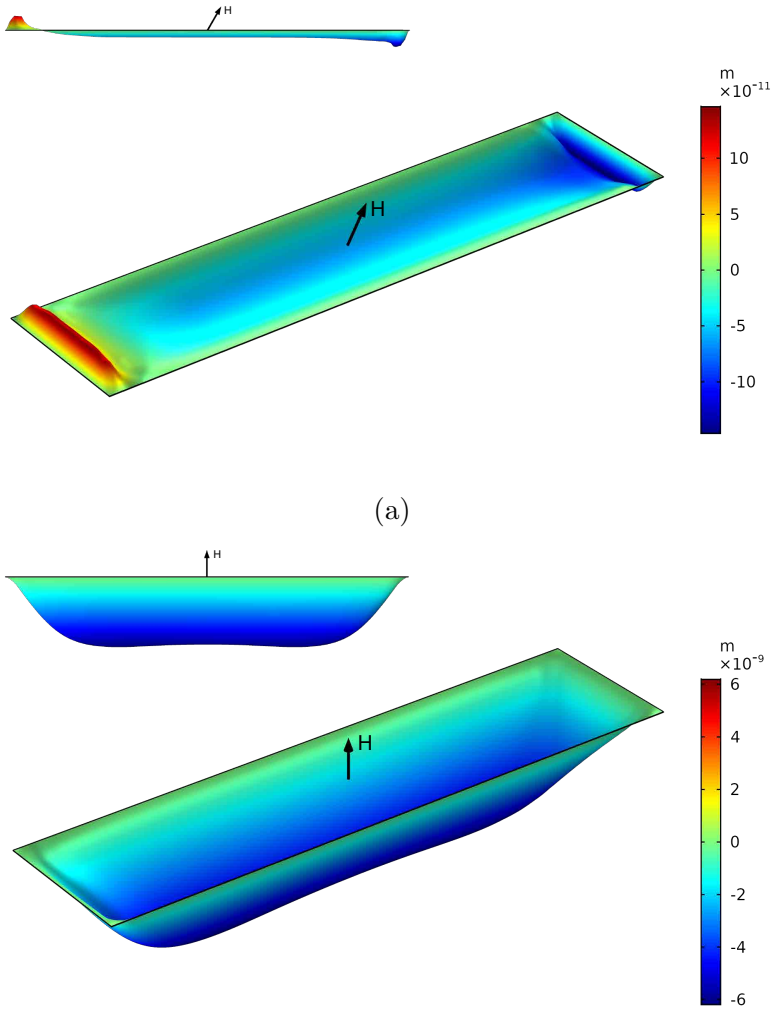


(a)

(b)

Figure 4.9: Magnetically-induced deformation profiles, with the bathtub-like pressure profile removed to shown only the magnetic deformation. The external magnetic field direction is indicated by the black arrow. The insets depict a side-view of the membrane. The unrealistic sharpness of features, primarily seen in (a), is the result from scaling the deflection to be visible. (a) Anti-symmetric deformation for a non-perpendicular magnetic field, at 60° with respect to the long-axis. Scaled by a factor $2 \cdot 10^5$. (b) Symmetric deformation in the presence of a perpendicular magnetic field. Scaled by a factor $2 \cdot 10^4$.

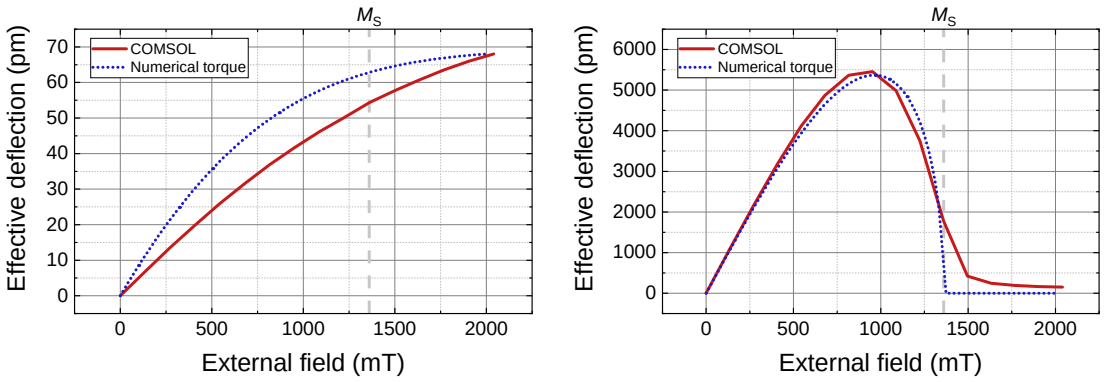


(a) (b)

Figure 4.10: Effective deflection as function of the external field strength. The corresponding numerical simulations of the torque are added for comparison. The torque has been rescaled to have the same maximum effective deflection, as such it is only a qualitative comparison. Note that the perpendicular field has a much greater effective deflection. (a) Non-perpendicular external field at 60°. (b) Perpendicular external field. There is a drop of the effective deflection after the saturation field of 1360 mT.

The effective deflection is derived by calculating the capacitance of the deformed film and using the calibration of the previous section. Figure 4.10 illustrates the effective deflection for the non-perpendicular and perpendicular fields, where the field strength is increased from 0 mT to 2000 mT. The pressure-induced deflection has been subtracted by offsetting the effective deflection to be zero at no external field. The graphs compare the effective deflection, as determined in COMSOL, to the torque from the numerical simulations. The torque has been rescaled to have the same maximum effective deflection as the COMSOL model. The qualitative behaviour of the model is very similar to the torque relation. Note that the effective deflection for the perpendicular field is much greater than the non-perpendicular field. This is to be expected as the deformation is much greater, as was shown in Figure 4.9. Overall the model is in agreement with the expectations from theory.

In short, the magnetically-induced deformations are modelled as a single CoB film with an effective stress. The model uses an iterative process to find the final deformation, using the pressure-induced deformation profile, Stoner–Wohlfarth model and Maxwell stress. The resulting magnetisation orientation, magnetically-induced deformation, and effective deflection are in agreement with theory and numerical simulations of the torque. The model is thus a good representation of how flexible magnetic thin films can deflect in uniform magnetic fields due to torque.

# 5
# Results & discussion

In this chapter, the deflection of flexible magnetic thin films in external magnetic fields is investigated, for the purpose of creating a magnetic field sensor. This investigation is guided by the following four questions that were introduced in Section 1.3:

- How does the deflection depend on the angle of the magnetic field?
- What is the relation between the deflection and the magnetic field strength?
- How does the magnetic layer thickness influence the deflection?
- What is the best configuration, in order to use the flexible magnetic film as a magnetic field sensor?

From theory and modelling it is expected that the deflection is directly coupled to the torque, with a strong reliance on the external field orientation and strength. In order to answer the first three questions, the magnetically-induced effective deflection will be measured and compared to modelling. The main variables in this work are the external magnetic field strength, field angle, and magnetic film thickness. The last question will be addressed by finding the optimal parameters for deflection, focussing on these three main variables. Most of the data shown in this chapter is for membranes with a 100 nm CoB layer, which is the median thickness of all samples grown in this project. Note that these measurements have also been performed on sensors with different CoB thicknesses, as described in Section 3.1.2, which show similar results.

The first section discusses the characteristics of the membrane and the magnetic thin film, which are crucial to the modelling and interpretation of the deflection. This involves the pressure-induced deformation profile of the membrane, the magnetic hysteresis of the thin film and the saturation magnetisation. The second section details the behaviour of the magnetically-induced effective deflection for a sensor with a 100 nm CoB layer, where the external field strength and field angle are varied. In the third section the influence of the CoB layer thickness is investigated, focussing on the added stiffness and the optimal effective deflection as function of layer thickness. Finally, the optimal magnetic resolution is discussed, defined by the optimal deflection per magnetic field strength and the deflection resolution.

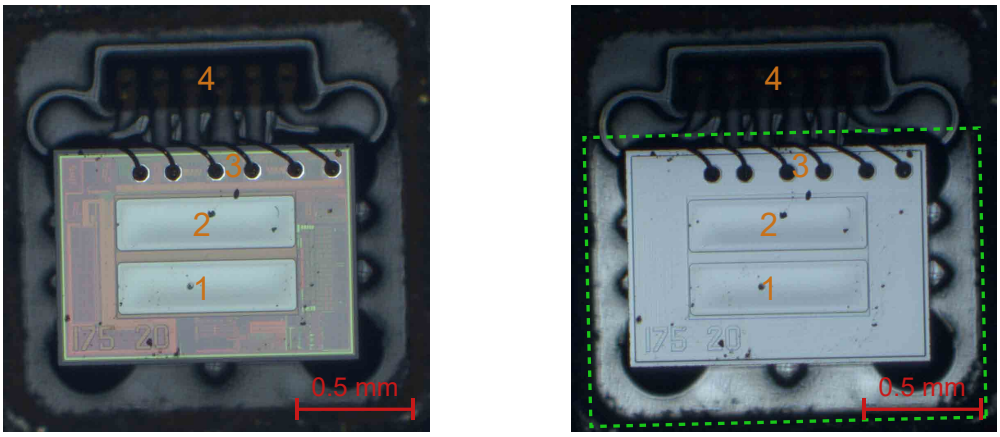


(a) (b)

Figure 5.1: Images of a sensor before and after deposition, taken with a microscope camera. In the bottom left of the sensor two numbers are shown that denote geometrical properties of the membranes. These two values are the same for all devices measured in this project. (a) Pre-deposition image of the sensor, consisting of two membranes (1, 2) and 6 bond pads (3) that connect to the bottom plate (4). (b) Post-deposition image of the sensor. The green dashed box denotes the deposition mask, which confines the deposition to the sensor and parts of the bottom plate.

## 5.1 Characterisation of the membrane & magnetic film

In this section, characteristics that are indirectly related to the effective deflection are investigated for the membrane and magnetic film. The main model assumptions are confirmed, which include the bathtub-like deformation due to pressure, the slope of the membrane at atmospheric pressures, the anisotropy of the magnetic film and the saturation magnetisation of the film. Figure 5.1 displays microscope images of a sensor before and after deposition. It displays the sensor with two grey membranes embedded (1, 2) and six bonding pads (3) on top of the sensor that connect to the bottom plate (4). The masked area is visible in the deposition image, where the green dashed lines highlight the edge of the mask. The deposition covers the entire sensor, without short-circuiting the lower bond pads (4).

### 5.1.1 Atmospheric pressure-induced deformation profile

The pressure-induced deformation profile of the membrane was shown in the modelling chapter, where a maximum deflection of 360 nm was seen at atmospheric pressures. In this section the pressure-induced deformation profile is verified and the maximum deflection and slope at atmospheric pressure are measured. The maximum deflection is used in the calibration of the effective deflection. To that end the Dektak profilometer set-up of Section 3.2.3 is used on a sensor with a 100 nm CoB layer. The results of this are shown in Figure 5.2.

The deformation line-scans have been performed along the long- and short-axis of the film, as denoted by X and Y in Figure 5.2a. The scan along the long-axis clearly

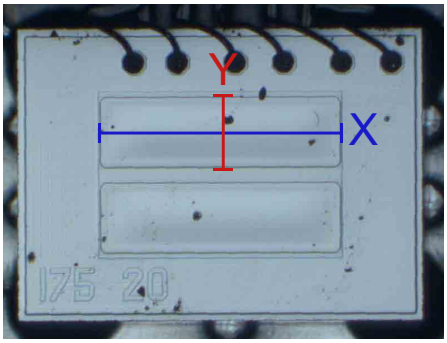


(a)

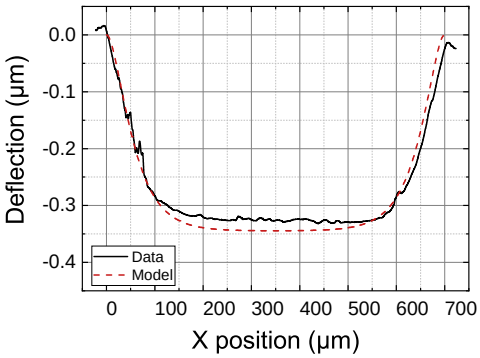


(b)

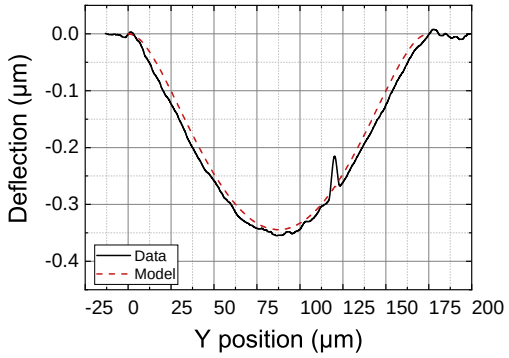


(c)

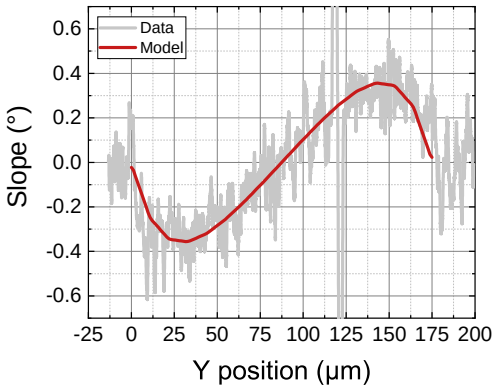


(d)

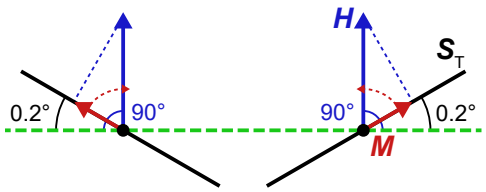


(e)

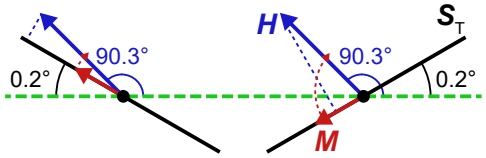


(f)

Figure 5.2: Graphs comparing the deformation profiles as measured by the Dektak and the COMSOL model. The measured device has 100 nm thick CoB layer. (a) Indication of the scan directions, with X along the long-axis and Y along the short-axis. (b) Scan along the long-axis of the membrane. (c) Scan along the short-axis of the membrane. (d) The slope of profile (c). The maximum slope of the model is 0.36°, with an average magnitude of 0.22°. (e) Repetition of Figure 4.8c, showing a symmetric magnetisation for perpendicular external fields. (f) Repetition of Figure 4.8d, showing an asymmetric magnetisation for external fields that deviate from perpendicular with an angle larger than the slope.

shows the bathtub-like deformation that is expected from modelling. Note that the bottom of the bathtub is not exactly flat, which is an expected measurement artefact of the Dektak set-up. The short-axis scan is a better indication of the maximum deflection, for the lowest point is measured even if the scan is not perfectly straight through the middle. For this sensor the maximum deflection is 350 nm.

The red dashed lines in the graph denote the deformation profile determined by the COMSOL pressure model, including a 100 nm CoB layer. It represents the measurement qualitatively very well, and for this specific case the quantitative solution aligns as well. This is not the case for all sensors, because in the model a specific stress is applied to the membrane, which can vary a bit in the actual sensors resulting in different deflection strengths.

As stated before, calibration of the effective deflection is done by converting the sensor's output pressure into an effective deflection. The conversion factor is determined from the maximum deflection measurement of 350 nm. This specific measurement is chosen, for it aligns well with the model and represents the other sensors. As a result, a conversion factor of 3.5 pm per Pa is used in all effective deflection results shown in this chapter. This is not an exact representation of each membrane's actual deflection, because the membrane stress and stiffness can vary a bit. However, it does allow for direct comparison of the different magnetic films, because the membranes (without magnetic layers) are considered to have the same stiffness.

In Figure 5.2d the slope of the membrane is determined along the short-axis. The slope has an average magnitude of 0.22°. Remember that in Section 4.2.2 it was discussed that the magnetisation orientation is symmetric for perpendicular external magnetic fields, as is drawn in Figure 5.2e. Moreover, it was hypothesised that the magnetisation orientation is symmetric, as long as the external field angle is perpendicular within the bounds of the film's slope. This transition from symmetric to asymmetric magnetisation is repeated in figures 5.2e and 5.2f. It is good to note that in the uniform magnetic field set-up, the resolution with which the external field angle can be set is 0.2°, which is approximately the same as the slope of the membrane. It is thus possible to probe symmetric magnetically-induced deflections that are expected for perpendicular fields.

In short, the measurements have shown that the pressure-induced deformation has indeed a bathtub-like shape and is well described by the COMSOL model. The maximum deflection at atmospheric pressure is measured to be 350 nm, resulting in an effective deflection conversion factor of 3.5 pm per Pa. The slope is on the order of 0.2°, which is similar to the resolution with which the field angle is set.

### 5.1.2 Magnetic hysteresis & saturation magnetisation

Magnetic hysteresis measurements are performed to confirm the magnetic easy-plane and measure the saturation magnetisation of the film. This measurement uses the MOKE set-up of Section 3.2.4, where the hysteresis is measured along three different axes. The results of the MOKE measurement are shown in Figure 5.3, where a membrane with 100 nm CoB is measured.

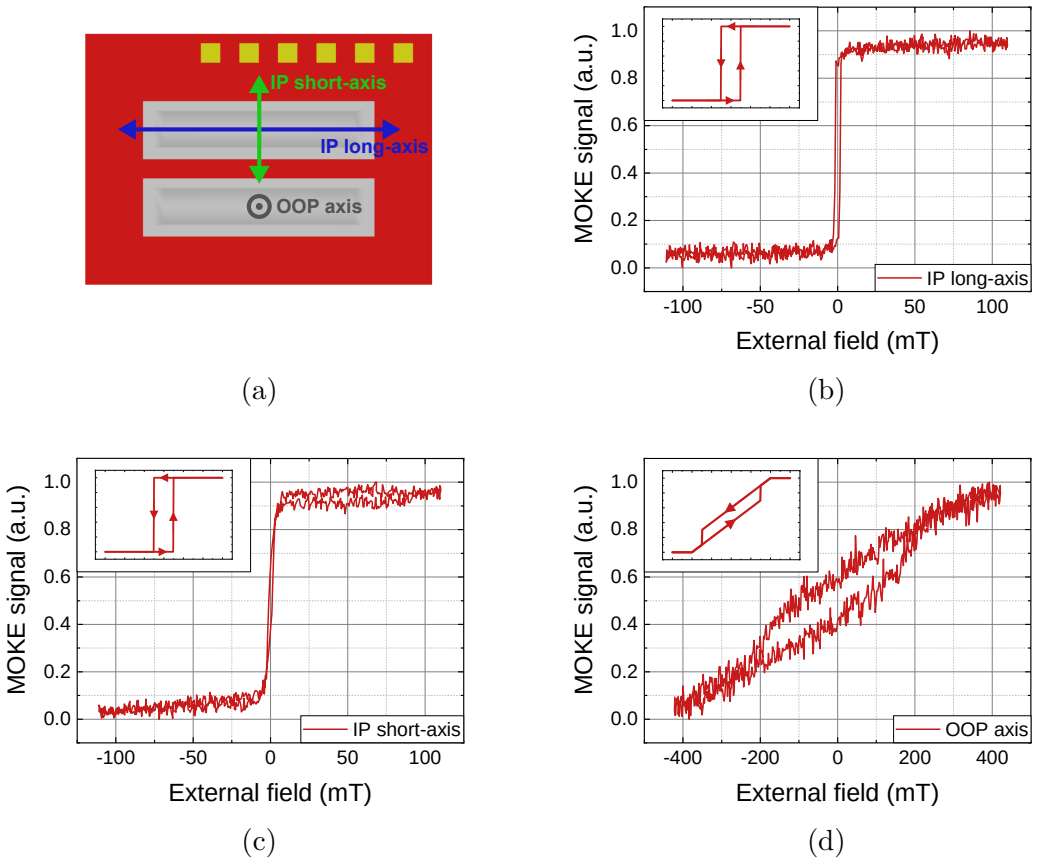


Figure 5.3: MOKE measurements along three different axes with respect to the magnetic film. The insets denote the expected hysteresis loops, that were shown in Figure 3.10. (a) Overview of the in-plane (IP) and out-of-plane (OOP) measurement axes. (b) IP long-axis, with a magnetisation switch at ±2 mT. (c) IP short-axis, with a magnetisation switch at ±2 mT. (d) OOP axis with an IP projection, as implied by the magnetisation switch at ±200 mT. The expected saturation magnetisation of 1.36 T is not reached in this measurement and the MOKE signal does not saturate.

The hysteresis loops clearly follow the expected form, as denoted in the insets. Both of the in-plane (IP) loops show sharp magnetisation switches that indicate an easy-axis and have a switching field close to 2 mT. The small switching fields indicate that the magnetisation can easily orient itself between the two easy-axes, forming a magnetic easy-plane. The coercivity of this easy-plane is on the order of 2 mT.

Measurement of the out-of-plane (OOP) axis deviates from the theoretical OOP hard-axis, which is caused by IP projections of the external magnetic field. The IP switching field is blown up to approximately ±200 mT, because the IP projection is much smaller than the total external field. This deviation from theory poses no problem for the measurements, as the IP projection is clearly distinguishable from the OOP measurement.

The OOP MOKE signal does not saturate, indicating that the saturation magnetisation is not reached with the MOKE set-up. Instead a SQUID magnetometer is used to measure the saturation magnetisation of CoB. The SQUID magnetometer

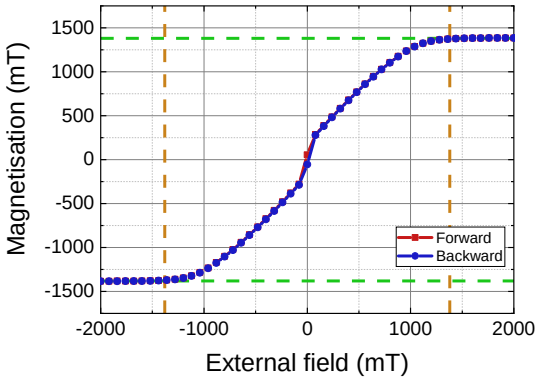


Figure 5.4: SQUID magnetometer measurement performed along the OOP hard-axis. It clearly shows a saturation magnetisation of 1380 mT, as indicated by the green and orange dashed lines. The green lines denote the direct measurement of the magnetisation, while the orange lines show the external field at which the magnetisation saturates.

measurement is done on a flat substrate with a 100 nm CoB film, similar to the sensor's used in the MOKE measurement. The result of this measurement is shown in Figure 5.4, which follows the expected OOP hard-axis hysteresis loop with a negligible IP projection. A saturation magnetisation of 1.38 T is measured, which agrees well with the literature value of 1.36 T [15].

In short, the magnetic anisotropy of the magnetic film is as expected. There is a magnetic easy-plane with a low coercivity on the order of 2 mT, with an OOP hard-axis. The saturation magnetisation of CoB is measured to be 1.38 T, which is in agreement with literature.

## 5.2 Magnetically-induced effective deflections

In order to understand flexible magnetic thin films and their potential as a magnetic field sensor, this section investigates the magnetically-induced effective deflection for different external field angles and field strengths. The measurements are performed with the uniform magnetic field set-up of Section 3.2.1 and are compared to the magnetic film model and numerical torque simulations, where the quality of the models is confirmed. Sensors with a 100 nm CoB layer are investigated in this section, with the next section discussing the effect of varying the CoB layer thickness.

In order to confirm the hypothesis that the effective deflection is greatest for perpendicular external magnetic fields, the first subsection investigates the deflection as function of field angle. The second subsection discusses the magnetically-induced deflections for perpendicular fields in more detail, examining the effective deflection as function of field strength and comparing it to the magnetic film model and torque simulations.

### 5.2.1 Magnetic field angle dependence

In the theory and modelling chapters it was suggested that the effective deflection is greatest for perpendicular external magnetic fields. The hypothesis is that the deformations are antisymmetric for non-perpendicular fields, resulting in lower deflections than the symmetric deformations in perpendicular fields. To confirm this, angle sweep measurements are done using the uniform magnetic field set-up, which is sketched in Figure 5.5a. The results of these measurements are shown in Figure 5.5.

In these measurements the external field angle $\alpha$ is swept from 0° to 180°, where the sensor is perpendicular to the magnetic field at 90°. In these sweeps a set of constant magnetic field strengths is used, ranging from 0 mT to 2000 mT. The measurements are shown in Figure 5.5b. It is directly clear that the effective deflection is enhanced at 90°, i.e. at perpendicular fields. The effective deflection quickly falls of as the angle deviates from perpendicular, where the deflection is minute for angles that differ more than 15° from 90°. Note that these miniscule deflections are still measurable, as the effective deflection has a resolution of 3.5 pm. The graph also shows that the enhancement at perpendicular fields diminishes for the larger field strengths of

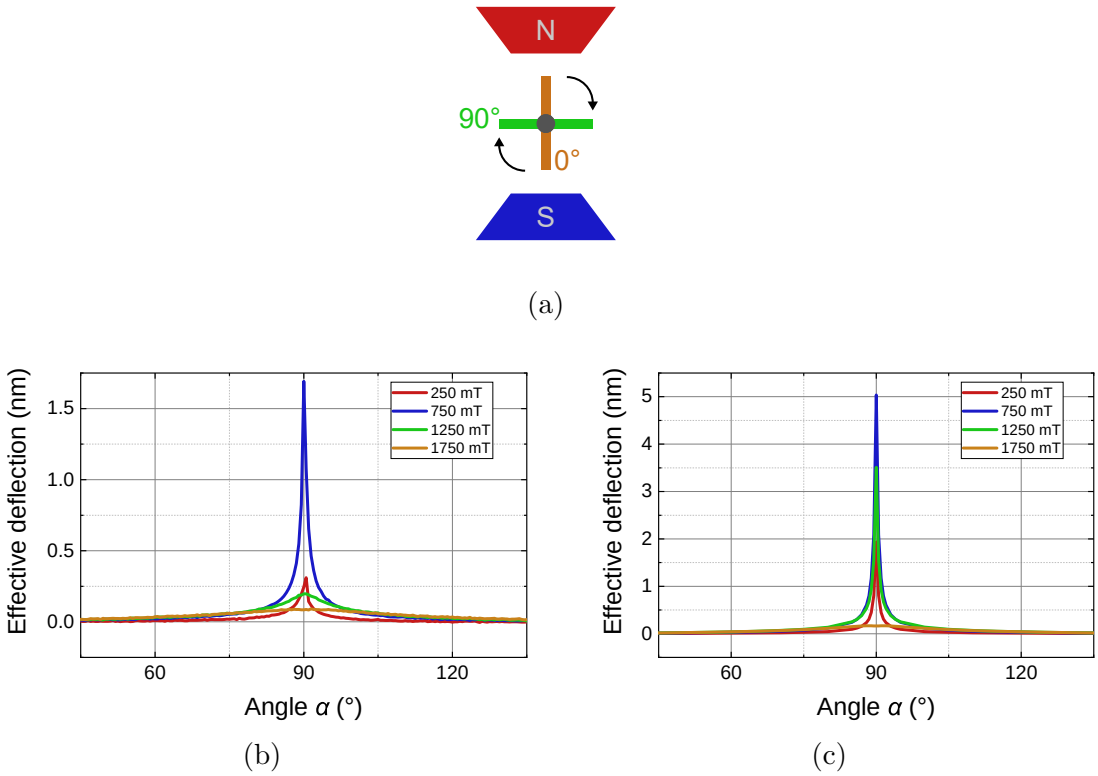


Figure 5.5: Field angle $\alpha$ sweeps for a set of external magnetic field strengths. The range is limited from 45° to 135°, because the deflection is negligible outside this range. (a) Schematic of the sensor orientation with respect to the magnetic pole pieces. The orange and green bars denote the plane of the sensor, where 90° is perpendicular to the magnetic field. (b) Measurements of the sensor with 100 nm CoB. (c) Modelling results, using the COMSOL magnetic film model with 100 nm CoB.

1250 mT and 1750 mT, which are near or above the saturation magnetisation of 1380 mT. For the 1750 mT measurement the effective deflection is still greatest at perpendicular fields, but the fall off is much weaker compared to the 250 mT and 750 mT measurements. The field strength dependence is further investigated in the next section, where the field strength is swept at constant angles.

Modelling results are presented in Figure 5.5c, where the measurements have been simulated with the magnetic film model of Section 4.2.2. There is a clear resemblance between the measurements and the model. The only differences are the magnitude of the deflection, that is much greater in the idealised model, and that the enhancement at perpendicular fields is still present for larger field strengths like 1250 mT. The increased magnitude is likely because the magnetic field angle is perfectly set in the model, resulting in stronger torques and deflections. In measurements, however, there can still be some small tilting of the sensor, as was explained in Section 3.2.1. The fact that the deflection enhancement is seen for higher fields in the model is also further discussed in the next section, where the sweeps of the field strength show similar results.

In short, it is confirmed that the effective deflection is greatly enhanced for perpendicular magnetic fields. This enhancement is predominantly visible for field strengths below 1 T. The effective deflection becomes negligible for angles that deviate more than 15° compared to the perpendicular field. The angle sweep measurements are well represented by the magnetic film model, showing only minor differences.

### 5.2.2 Perpendicular magnetic field induced deflections

From the previous section it is known that the effective deflection is greatly enhanced at perpendicular magnetic fields. However, it is not yet clear if the relation between deflection and field strength is well described by the magnetic film model and torque descriptions. This is tested by measuring the effective deflection, while sweeping the strength of the perpendicular magnetic field, and comparing it to the models. The sensor's orientation and first measurement results are shown in Figure 5.6.

The graph shows a measurement of the effective deflection, where the external magnetic field is swept in the direction of the red arrow from $-2$ T to 2 T. From the graph it is already visible that the effective deflection behaves similar to the torque relation of Section 2.3.1. As such, the magnetisation orientation can be estimated for different parts of the graph, as is shown on the right. The effective deflection is zero when there is no external field and the magnetisation lies fully in the easy-plane of the film. It then starts to increase with the external field, where the deflection peaks at a field that will be denoted as the peak-field $H_P$. It is expected that this peak is reached when the magnetisation is rotated 45° with respect to the magnetic easy-plane, which is where the maximum torque would be exerted as was explained in Section 2.3.1. Finally, the effective deflection would drop to zero when the magnetisation and external field are fully aligned, and thus no torque is exerted. This field is referred to as the drop-field $H_{Drop}$.

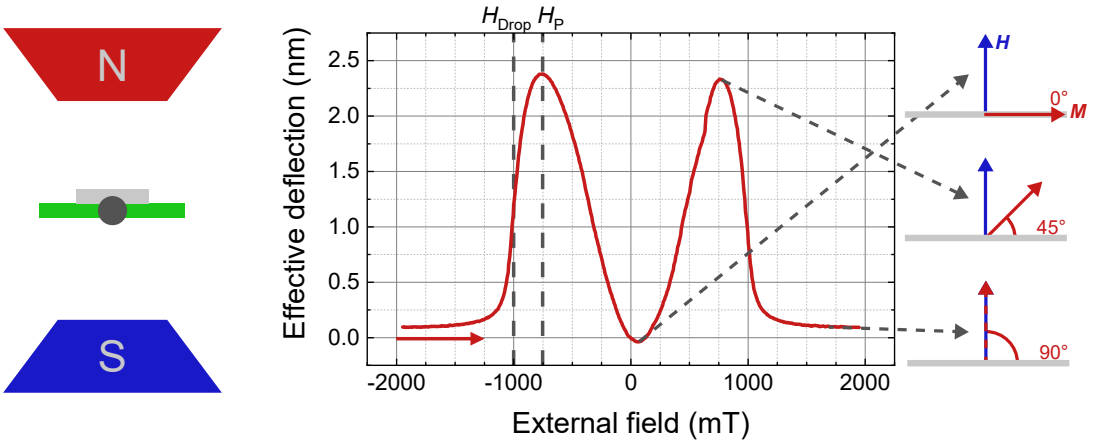


(a) (b)

Figure 5.6: (a) Schematic of the perpendicular orientation of a sensor with respect to the magnet. (b) Effective deflection measurement of a sensor with a 100 nm CoB layer, where the field is swept in the direction of the red arrow from −2 T to 2 T. The expected magnetisation orientation, with respect to the easy-plane, is denoted on the right for several key points.

On closer inspection it is seen that the minimum of the effective deflection is not exactly at 0 mT. This is likely due to magnetic hysteresis, as there is a very small in-plane projection of the external field. Similar effects were seen in the MOKE measurements, where the out-of-plane, i.e. perpendicular, measurement showed magnetisation switching that is typical for the in-plane component. This shift of the minimum deflection is better shown in Figure 5.7a, which is a perpendicular field measurement on a sensor with a 250 nm CoB layer. A thicker CoB layer is used in this example because it has a higher aspect ratio, which slightly lowers the out-of-plane demagnetisation factor and shape anisotropy that are typical to thin films. As a result the hysteresic effects in the plane are increased, as the out-of-plane hard-axis becomes slightly less hard and the easy-plane becomes slightly less easy. These are still minor effects as the out-of-plane demagnetisation factor is approximately 0.98, with a factor of 1 being the ideal thin film. In this graph the effective deflection minimum, that is expected at 0 mT, is shifted significantly. Moreover, it strongly depends on the sweep direction of the external field strength, indicating that it is due to hysteresis.

A direct comparison between effective deflection measurements and the torque and magnetic film model is made in Figure 5.7b. The torque has been scaled to have the same maximum as the measurement, and thus is no indication of the quantitative performance. The magnetic film model has been rescaled by a factor 0.45, and is thus within the same order of magnitude as the measurements. The overall qualitative behaviour of the measurement fits well to both the torque and magnetic film model.

Two major differences between modelling and measurement are the peak-field and the drop-field. From theory it is expected that the peak- and drop-field are related to the anisotropy field, which for shape-induced anisotropy in a thin film equals the

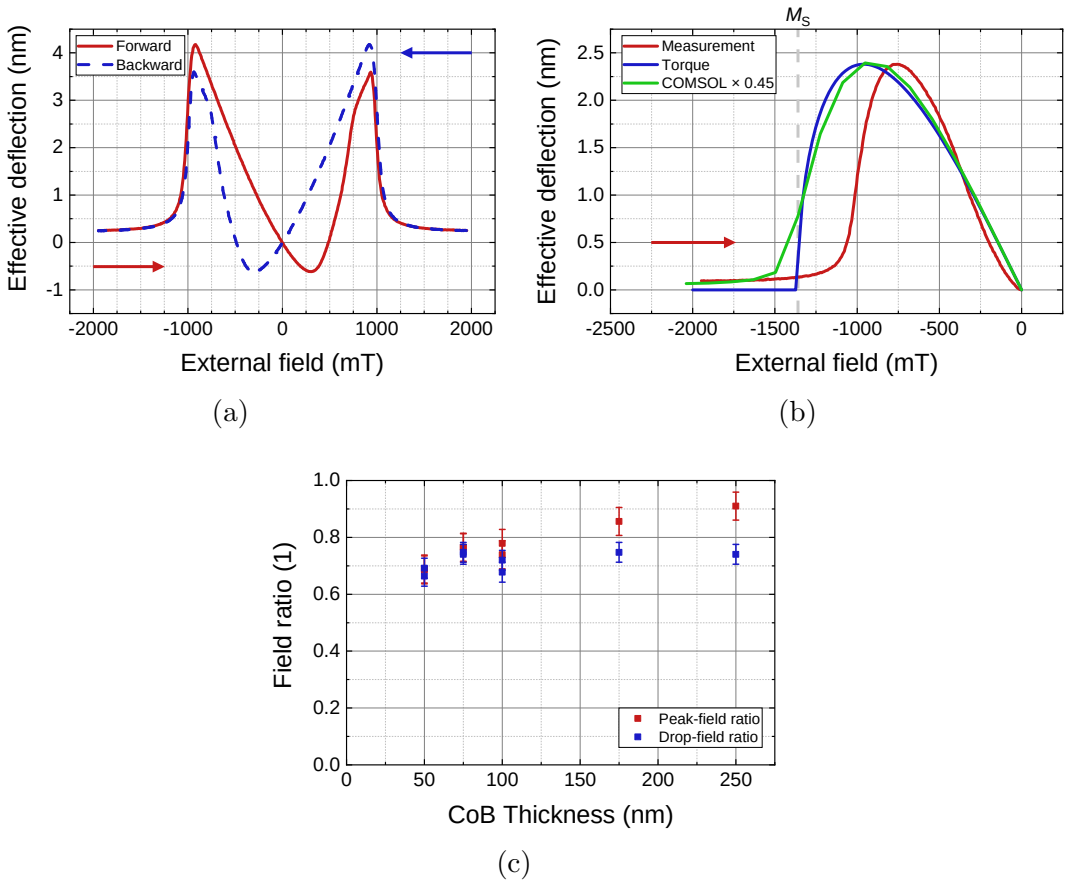


Figure 5.7: (a) Effective deflection measurement on a 250 nm CoB layer, for both external field sweep directions. The effect of magnetic hysteresis is clearly visible in the shift of the deflection minimum. (b) Comparison of the effective deflection for the 100 nm CoB measurement of Figure 5.6 and the torque and magnetic film model. Only half of the graph is shown, for it is close to symmetric around 0 mT. The line $M_S$ denotes the saturation magnetisation, that was measured in Section 5.1.2. (c) Ratios of the measured peak- and drop-field divided by the expected fields, as function of the CoB layer thickness. The drop-field is constant over the measured range, with an average ratio of 0.72. The peak-field appears to increase linearly over the measured range, ranging from 0.7 to 0.9.

saturation magnetisation $M_S$. The maximum torque for perpendicular fields would be exerted at $0.71M_S$ and the torque drops at $M_S$. The measured value of $M_S$ from Section 5.1.2 is shown in the graph, which is 1.38 T and is used in modelling. The expected peak- and drop-field would be 0.98 T and 1.38 T respectively, as is the case for the models. However, the effective deflection measurement implies a saturation magnetisation of approximately 1 T, for the effective deflection drops at that field. Figure 5.7c shows the ratio of the measured fields divided by the expected field for a set of different CoB layer thicknesses. Both the measured peak- and drop-field are approximately 0.75 times the expected values, where there appears to be a slight linear grow in the peak-field ratio. Other thickness related effects are discussed in the next section. It is not yet clear as to why the peak- and drop-field are smaller than expected, but the next parts will exclude and speculate on possible reasons for this difference.

Although no conclusive answer can be made on the difference between the model and the measurement, some reasons can be excluded. Measurements of the same sensor have been performed several months apart and still show the exact same results. This indicates that the difference is not due to some long time degradation of the magnetic film, such as the layer coming loose or partial oxidation of the film. Another effect that is unlikely to be the problem is the effect of magnetostriction. While CoB experiences some magnetostriction, similar measurements were done with a Permalloy magnetic layer, which is known for having nearly no magnetostriction. In these measurements the tilt was not completely compensated for, but the peak- and drop-field were still 0.5 times the expected value, implying that the difference is not due to magnetostriction. Because if it were due to magnetostriction Permalloy would be closer to the expected drop-field, as magnetostriction is not taken into account in the theory or models. The measurements from Figure 5.7a have also shown that the peak- and drop-field occur at the same field strengths, no matter the sweep direction. As such, the omission of hysteresis in the magnetic film model is not likely to account for this difference either, because otherwise the sweep direction would have some influence.

One possible reason could be that the model assumption, that the magnetisation orientation can rotate separately for each finite-element, is too simple and that instead a more complex domain separated magnetic state is present. In this case the slight tilting of the sensor, compared to the magnetic field, could result in a shift of the domains, which in turn could drop the effective deflection at lower magnetic fields. Note that, simply adding a tilt to the magnetic film model does not resolve the discrepancy between measurement and modelling, because proper domains are not implemented in the model. Another possible reason could be that the saturation magnetisation is different for a deposition on the membrane, compared to the flat substrate sample that was measured with the SQUID magnetometer. However, there is no clear evidence that this should be the case and as such it remains unclear as to why the measured effective deflection drops sooner than the model.

It should be noted that field sweep measurements have also been performed for non-perpendicular angles. These measurements do not result in new insights but can be found in Appendix A.2. There it is shown that the results are well in line with the magnetic film model and numerical torque simulations. However, the magnitude of the deflection is much lower, as was already seen in the angle sweeps of the previous section.

In short, the magnetic field strength sweeps show a behaviour that is well explained by the magnetic film model and torque description. A peak-field and drop-field can be distinguished in these measurements, which are also present in the models. However, the field strength at which these happen are approximately 0.75 times the values expected from modelling. The reason for this difference is not yet understood.

## 5.3 Influence of the magnetic film thickness

One of the main goals of this project is to gauge the possibility and quality of the flexible magnetic film as magnetic field sensor. From the previous sections it has become clear that magnetically-induced deflections can be measured. Moreover, it showed that the response is well described by torque and the magnetic film model. In these measurements a typical CoB layer thickness of 100 nm was presented. While the qualitative behaviour is not strongly affected by the CoB layer thickness, the quantitative behaviour definitely is. More specifically, the stiffness of the membrane is expected to increase due to the added CoB layer and the torque is expected to grow linearly with the CoB layer thickness, which would lead to an increase of the effective deflection.

The first section discusses the added stiffness caused by the CoB layer. An added stiffness does not change the calibration of the effective deflection, but it would change the sensitivity of the sensor, i.e. the amount of deflection per applied force or torque. The second section examines the effective deflection at the peak-field as function of CoB layer thickness. In addition, a rough extrapolation is done for the effective deflection as function of CoB thickness, where the changing sensitivity and estimated linear increase of torque are used.

### 5.3.1 Decline in sensitivity

The pressure sensor's membrane is originally designed to be flexible, so that it can be used to measure the ambient pressure. The magnetic layer, however, consists of the metal CoB and behaves more like a stiff plate than a flexible membrane. To get an idea of how strongly the flexibility of the membrane depends on the CoB thickness, a measurement is done on the deviation of the sensor's output pressure, compared to the actual pressure. The results are shown in Figure 5.8, where the CoB thickness is varied from no CoB to 250 nm CoB.

The devices are put in the pressure tank set-up of Section 3.2.2, where the pressure is varied from 200 mbar to 1200 mbar. The added stiffness of the CoB layer implies that the membrane deflection will be smaller than with no CoB layer, and thus should result in a lower pressure. This is measured as a deviation of the sensor's output pressure, compared to a commercial high-precision pressure measurement device. In Figure 5.8a the sensor's output deviation is set out against the set pressure, for a range of different layer thicknesses. In addition, the graph also compares the measurement to simulations from the COMSOL pressure model of Section 4.2.1. The deviation is linear with the set pressure, which is expected for a stiffer membrane because the deflection per applied force has decreased.

The model and measurements show that the slope of the output deviation becomes more negative with layer thickness, i.e. the sensor's output pressure per applied pressure decreases with thickness. In that sense the sensitivity of the sensor decreases with an increasing CoB thickness. This is illustrated in Figure 5.8b, where the sensitivity ratio is defined as one plus the slope of the output deviation, such that the ratio is one for sensors without a CoB layer. It draws a clear picture of how

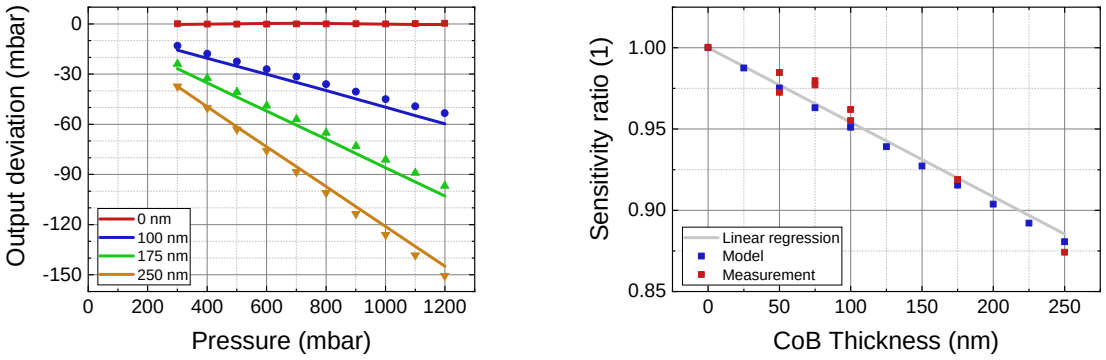


(a) (b)

Figure 5.8: (a) Pressure sensor output deviation as function of the regulated pressure. The markers denote measurements, while the lines consist of the corresponding modelling data. (b) The sensitivity ratio of the sensors, defined as one plus the slope of the output deviation from (a). The grey line denotes a linear regression of the measurement data.

the stiffness increases linearly with CoB thickness, resulting in a linear decrease of the sensitivity. For example, a membrane without CoB would deflect 3.5 pm per Pa, but a membrane with 100 nm CoB would have a sensitivity ratio of 0.95, meaning that it would deflect 3.325 pm per Pa. In terms of output pressure this means that a membrane with 100 nm CoB outputs 95% of the actual pressure, as can be seen in Figure 5.8a.

This change in sensitivity has no bearing on the sensor's effective deflection output, because the capacitance change due to deflection does not change. As such the original calibration, before layer deposition, still results in a correct deflection output. The sensitivity of course does influence the amount of deflection per (magnetically) applied force, by definition. By compensating for the sensitivity ratio, the effective deflection becomes a qualitative measure of the forces applied to the membrane, such as the magnetic torque. This is used in parts of the next section, where a rough extrapolation done for the effective deflection as function of CoB thickness.

In short, the magnetic CoB layer adds to the stiffness of the membrane, which is measured as a deviation of the sensor's output pressure compared to the actual pressure. This increased stiffness is represented as a sensitivity ratio that decreases linearly with the CoB thickness. This loss of sensitivity has no bearing on the sensor's deflection output calibration. When you compensate for this loss of sensitivity ratio, the effective deflection is proportional to the (magnetically) applied force.

### 5.3.2 Increase in torque & effective deflection

From theory it is expected that the torque is proportional to the magnetic volume that increases with the CoB thickness, as was detailed in Section 2.3.1. As such, it can be expected that the effective deflection increases with the CoB thickness, as long as the grow of torque outweighs the decrease in sensitivity. In order to confirm this, deflection measurements have not only been performed for the 100 nm CoB

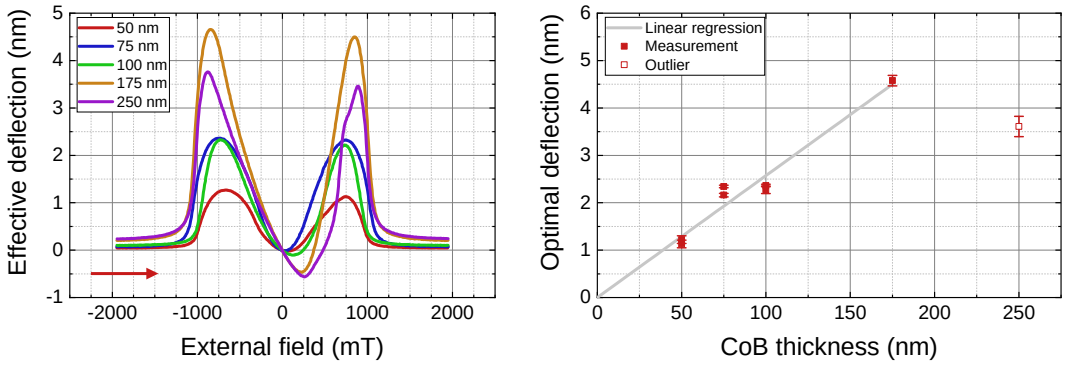


(a) (b)

Figure 5.9: (a) Perpendicular magnetic field strength sweeps for different CoB layer thicknesses. The arrow denotes the sweep direction. (b) The optimal effective deflection as function of the CoB layer thickness. The linear regression has its intercept set to zero and ignores the outlier at 250 nm. The error bars are determined from the standard deviation of the two peaks of (a).

layer, but also for a set of thicknesses within the range of 50 nm CoB to 250 nm CoB. This specific range was chosen for the deflection was expected to be measurable and, as explained in Section 3.1.3, thicker layers could not be produced because they led to electrical shorts of the sensor. Figure 5.9 shows measurement results of the effective deflection for different CoB thicknesses.

In previous sections it was shown that the effective deflection is enhanced for perpendicular magnetic fields, and is greatest at the peak-field strength. The perpendicular field measurements of the different CoB thicknesses are shown in Figure 5.9a. It is directly clear that the magnitude of the effective deflection is greatly influenced by the layer thickness. The graph also displays the stronger hysteresic effects and increase of peak-field for thicker films, which were discussed in Section 5.2.2. The effective deflection at the peak-fields is set out in Figure 5.9b, which is referred to as the optimal deflection for it is the greatest deflection measured for that sensor. Note that the optimal deflection measurement is not a one time occurrence, as some of the measurements were repeated after a few months and still showed the same optimal deflection.

In Figure 5.9b it is shown that the optimal deflection increases with CoB thickness, except for the 250 nm CoB film. Such a sharp decline in deflection at this thickness is not expected to be due to the sensitivity, and because it is only a single device it is taken to be an outlier. The largest deflection of 4.5 nm is measured for a 175 nm CoB layer. The graph also shows a linear regression of the measurement data with the intercept set to zero, which is valid because there is no magnetically-induced deflection when there is no magnetic layer. The linear regression fits astoundingly well to the measurement, even though the sensitivity ratio has not been compensated for.

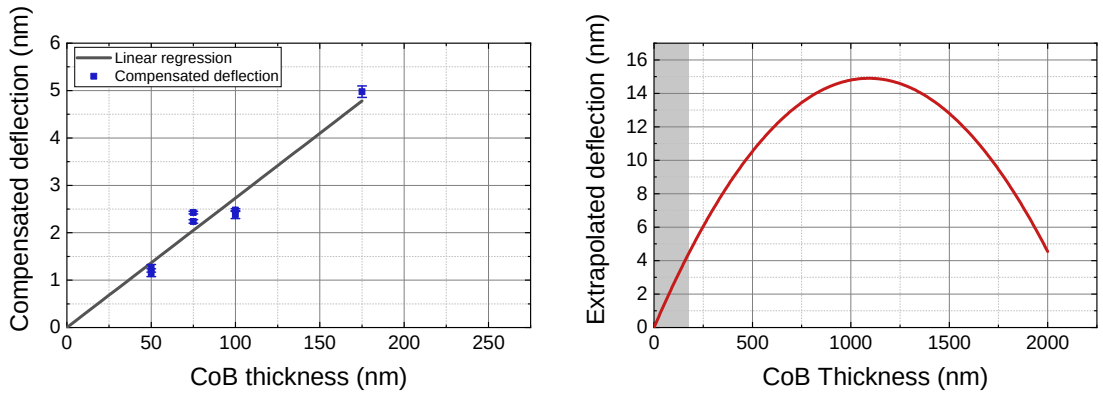


(a) (b)

Figure 5.10: (a) Optimal effective deflection of Figure 5.9b, where the sensitivity ratio has been compensated for. The linear regression has its intercept set to zero and fits very well to the data. (b) Extrapolation of the deflection using equation 5.1. The grey area denotes the range for which measurements were done. The extrapolated deflection peaks near 1100 nm, where it is estimated that the optimal deflection is 15 nm. Note that this value is far from the measurement range and thus unreliable, however, it demonstrates that the deflection does not increase indefinitely.

It is expected that at some CoB thickness the film becomes too stiff, such that the increasing torque no longer increases the optimal effective deflection. In order to investigate this, a rough extrapolation of the optimal deflection is made using the optimal deflection and the sensitivity ratio of the previous section. Figure 5.10a shows the sensitivity compensated optimal deflection, which qualitatively represents the torque and is an indication of how the deflection would grow if the stiffness of the membrane with magnetic layer was constant. Combining the slope of the compensated deflection and the slope of the sensitivity ratio results in an extrapolation of the following form:

$$D = (S_{comp} \cdot t) \cdot (1 + S_{sens} \cdot t), \tag{5.1}$$

where $D$ is the extrapolated deflection, $S_{comp}$ the slope of the compensated deflection, $t$ the CoB thickness and $S_{sens}$ the slope of the sensitivity ratio. The first term encapsulates the linear growth of the torque, while the second term describes the linear decrease of sensitivity of the previous section. The result is a quadratic relation, which is shown in Figure 5.10b. This rough extrapolation shows that the optimal deflection should peak around a 1100 nm thick CoB layer. For thicker layers the decrease in sensitivity would be greater than the increase in torque.

Note that this extrapolation only holds true while the decrease in sensitivity is linear and the overall behaviour of the system does not change, which is not verified by measurements. This is a simplified view of the actual physics at play and a more correct view would be to simulate a close to linearly increasing stiffness, instead of linearly decreasing sensitivity. Preliminary calculations and modelling on this are done in Appendix A.3, where the model still shows an optimal deflection that is limited by the stiffness. The ultimate deflection could thus be different and occur at another CoB thickness. However, it does illustrate that increasing the effective deflection by growing thicker CoB layers has its limits.

In addition, the shape anisotropy is also limited by the CoB thickness, as it increases the aspect ratio of the film. However, this should not be a problem yet, as the demagnetisation factor is still higher than 0.96 for a few microns thick CoB layer on a $700 \times 175$ $\mu m^2$ membrane, i.e. the out-of-plane demagnetisation field is still close to 1.38 T.

In short, the optimal effective deflection grows close to linear, where an optimal deflection of 4.5 nm is seen for the 175 nm thick CoB layer. A rough extrapolation is used to illustrate that the growth of optimal effective deflection is limited by the loss of sensitivity.

## 5.4 Magnetic resolution of the sensor

In order to gauge the quality of the film as magnetic field sensor, this section provides a rough estimation of the magnetic resolution that is achieved with this sensor. As stated before, the magnetic resolution is defined as the smallest resolvable magnetic field change. In terms of the sensor this is related to the smallest magnetic field change that results in a resolvable deflection change. The magnetic resolution will be estimated using a linear approximation as shown in Figure 5.11. These approximations are made for the 175 nm CoB layer, because the measured deflection is greatest for that thickness.

The approximation states that the effective deflection is zero at zero field and increases linearly to the optimal deflection at the peak-field, as indicated by the green arrow. From this the deflection per magnetic field strength is calculated to be 5.55 pm per mT. The magnetic resolution is then simply determined by looking at what field is necessary to induce a 3.5 pm deflection, which is the deflection resolution. The magnetic resolution of the 175 nm CoB layer is thus approximated to be 0.6 mT. This is astoundingly good, reaching a resolution that is on the same order as commercially available sensors, that are within the same size and price categories [1–5]. Note that in this approximation the magnetic field strength can

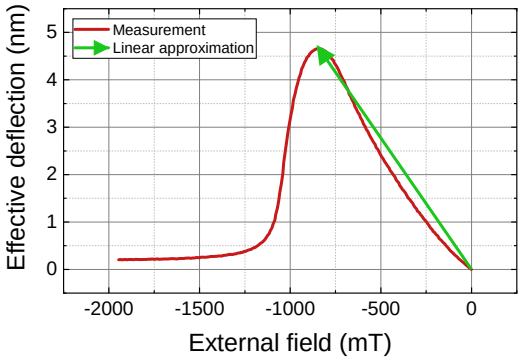


(a)

Figure 5.11: Deflection measurement of the 175 nm CoB film sensor. The green arrow denotes the linear approximation used to estimate the magnetic resolution.

only be measured for fields below the peak-field and is degenerate for positive or negative fields.

In short, the magnetic resolution of the best measured sensor is approximated to be 0.6 mT. This is close to commercially available sensors and shows that the flexible magnetic film sensor has the potential to be a competitive new kind of magnetic field sensor.

# 6
# Conclusion

In this thesis the capacitive pressure sensor of AMS Netherlands has been the foundation on which flexible magnetic thin films have been investigated. This was done to explore the behaviour of flexible magnetic thin films and the possibility of functionalising the pressure sensor as a magnetic field sensor. To this end, the effective deflection of flexible magnetic thin films in externally applied magnetic fields has been measured and modelled using a magnetic torque description and a finite-element model based on the Stoner–Wohlfarth model and Maxwell stress. This chapter will summarise the conclusions that were discussed in Chapter 5, following the four questions that were introduced in Section 1.3, and give a concise conclusion of the work as a whole.

**How does the deflection depend on the angle of the magnetic field?**
Both measurements and modelling of the magnetic field angle make it clear that the deflection is greatly enhanced for magnetic fields that are perpendicular to the membrane. The field angle is a strict parameter, where deviations of a few degrees away from perpendicular result in negligible effective deflection outputs. The angle dependence is well described by the magnetic film model, showing only minor differences.

**What is the relation between the deflection and the magnetic field strength?**
The measured effective deflections, as function of field strength, are well in line with the qualitative predictions of the torque and magnetic film model. It showed distinct peak-field and drop-field strengths that were predicted by the torque simulations and modelling. However, the field strengths at which these occur are approximately 0.75 times the expected values. The exact reason for this discrepancy is as of writing unknown, however, measurement data suggests that long time degradations, magnetostriction and hysteresis are not likely the cause.

**How does the magnetic layer thickness influence the deflection?**
Thickness dependent studies have shown that the sensitivity, the amount of deflection per applied force, decreases as the magnetic layer becomes thicker. For the investigated thicknesses between 50 nm and 250 nm this effect is still minor, where the sensitivity at 250 nm was 87% of its value without the magnetic layer. Measurements of the deflection as function of magnetic layer thickness show a close to linear grow. This is expected for the torque and further confirms that the change of

sensitivity only plays a minor role at these thicknesses. However, rough extrapolations indicate that the linear increase of the deflection is limited by the stiffness of the CoB layer, which might become a problem at thicknesses close to one micron.

**What is the best configuration, in order to use the flexible magnetic film as a magnetic field sensor?**
It has been shown that the magnetically-induced effective deflections are easily measurable by the sensor. From the previous three questions it can be concluded that the following configuration choices lead to a stronger deflection and thus a better magnetic resolution.

- Perpendicular magnetic fields greatly enhance the deflection, where the range of perpendicular angles is limited by the slope of the membrane. Increasing the slope would thus increase the angle tolerance of your perpendicular magnetic field.

- The usable magnetic field range is limited to field strengths below the saturation magnetisation of your material, as the deflection becomes minimal above the related drop-field. The optimal deflection is reached at the peak-field, which for the measured CoB samples occurs between 600 mT and 900 mT ($0.45M_S$ and $0.66M_S$).

- A thicker magnetic layer results in greater deflections and a better magnetic resolution. Diminishing effects due to an increased stiffness were not yet seen for CoB thicknesses below 175 nm. However, extrapolations suggest that there is an optimal thickness on the order of a few microns, after which the increased stiffness reduces the deflection.

Using these parameters it was shown that the 175 nm CoB sensor can achieve a resolution of approximately 0.6 mT, which is incredibly good. The sensor is able to reach a resolution that is on the same order as commercially available sensors, that are within the same size and price categories [1–5]. It should also be stated that this is an introductory study on flexible magnetic thin films, where the underlying capacitive pressure sensor was not designed to be a magnetic field sensor. Flexible magnetic thin films are thus a novel and competitive technology for magnetic field sensors, and with further optimisation of the sensor it has the potential to be superior to currently available sensors.

In conclusion, the behaviour of flexible magnetic thin films is well described by the torque and magnetic film model. There are still some open questions with regards to the peak- and drop-field, that need to be investigated further. The pressure sensor is functionalised as a magnetic field sensor, where the magnetic resolution is approximated to be 0.6 mT. This is an impressive first result, with the resolution being on the same order as commercially available sensors.

# 7
# Outlook

This work has provided an exploratory investigation of flexible magnetic films and how they deflect in the presence of a uniform magnetic field. This chapter will discuss possible future steps to take with this project, focussing on understanding flexible magnetic films and design choices that might improve its capability as a magnetic field sensor.

In this study the magnetically-induced deflections were investigated through measuring the effective deflection, which is an indirect measurement. It would of course be better to measure the deflections directly. However, it is hard to directly measure the deflection, because the deflections are either small or require large magnetic fields. Nevertheless, it should be possible to measure the deflections using a sub-nanometer resolution atomic force microscope (AFM) or laser interferometer, in combination with a strong electromagnet. The AFM and interferometer could also be used to make scans of the entire membrane, which could be used to confirm the antisymmetric deformations that are expected for non-perpendicular field angles. In addition, a magnetic force microscope (MFM) could be used to investigate the magnetic domain structure, which can verify the expected magnetic configuration for an out-of-plane magnetic field. All of this would justify the assumptions made in modelling.

In Section 2.3.2 the effect of a magnetic field gradient on a magnetic material was discussed. However, this was not measured for the flexible magnetic films due to time restrictions. It would be interesting to measure the effective deflection as function of the magnetic field gradient, as it would be another method for deflecting a flexible magnetic thin film and using it as a magnetic gradient sensor or current sensor. Measurements would be similar to the measurements performed with the uniform magnetic field set-up, but instead of varying the field strength, the gradient of the field would be varied (making it non-uniform).

A follow-up study on the peak- and drop-field would certainly be of interest. However, from the speculations it is not yet clear what might be the cause of the discrepancy between model and measurement. The first step into gaining more information would be to repeat the effective deflection measurements for sensors with different magnetic layer materials. In this work it was stated that similar measurements were done for a Permalloy magnetic layer. However, these were early measurements in which the parameters were not as precisely controlled as for the CoB measurements.

It would thus be good to do proper measurements on Permalloy and other possible materials to see what the relation between the drop-field and saturation magnetisation is for these different materials. If the relation between the drop-field and saturation field is linear, as is expected, one could then increase the drop-field by utilising magnetic materials with a greater saturation magnetisation.

The CoB alloy was chosen as magnetic material, among other things, for its lack of intrinsic anisotropy. In this sense only shape-induced anisotropy, in the form of a demagnetisation field, has been investigated. However, there are many different types of anisotropy that could be investigated, like crystalline anisotropy, perpendicular magnetic anisotropy and induced anisotropy. By engineering these anisotropies it would be possible to change the field angle dependence, because the magnetisation orientation strongly depends on the anisotropy. While altering the anisotropy is not likely to lead to stronger deflections, it might provide a wider angle range within which the deflection is enhanced. From theory one would also expect that the peak- and drop-field are related to the anisotropy field, which for shape-induced anisotropy scales with the saturation magnetisation. It would thus also be interesting to see if the peak- and drop-field could be increased by utilising different anisotropies.

In the same trend it would be interesting to look at circular membranes, where the shape anisotropy is circularly symmetric. Moreover, the deflection would no longer be hampered by the shortest axis of the membrane. For perpendicular magnetic fields this would mean that the torque can work on the entire membrane, not only on the edges as was drawn in Figure 2.8. In this manner you would get the most out of your torque, resulting in greater deflections.

Another venue to investigate would be partial coverage depositions, where for example only half of the membrane is covered with a magnetic layer. These measurements would be more similar to the embedded Permalloy strip studies [6, 7], as there only half of the membrane had strips embedded. It would be interesting to see how this affects the deflection in magnetic fields that are not perpendicular to the membrane, because there would not be an antisymmetric deflection if only half the membrane is covered.

For the purpose of a magnetic field sensor it would also be essential to look at membranes and magnetic materials that are more flexible. The amount of deflection per torque would be greater and more easily measured, which would result in a better magnetic resolution. For example, if it were possible to get deflections of 1 micron, at the same peak-field of 840 mT and with the same deflection resolution of 3.5 pm, the magnetic resolution would be on the order of microTeslas.

The modelling and measurements have thus shown that there are many parameters to tweak with flexible magnetic films, which have not yet been fully investigated. This gives confidence that there is still much to gain in understanding flexible magnetic films and that new applications might lie on the horizon.

# Bibliography


[1] Bosch Sensortec (2012). BMM150 [Magnetic field sensor]. Retrieved from https://www.digikey.com/product-detail/en/bosch-sensortec/BMM150/828-1044-1-ND/4196683.

[2] Memsic Inc. (2018). MMC5603NJ [Magnetic field sensor]. Retrieved from https://www.digikey.com/product-detail/en/memsic-inc/MMC5603NJ/1267-MMC5603NJTR-ND/10452796.

[3] Silicon Labs (2016). SI7213-B-00-IVR [Magnetic field sensor]. Retrieved from https://www.digikey.com/product-detail/en/silicon-labs/SI7213-B-00-IVR/336-4132-2-ND/7323122.

[4] Texas Instruments (2014). DRV5053VAQDBZR [Magnetic field sensor]. Retrieved from https://www.digikey.com/product-detail/en/texas-instruments/DRV5053VAQDBZR/296-38460-2-ND/5015738.

[5] AMS (2012). AS5510-DWLT [Magnetic field sensor]. Retrieved from https://www.digikey.com/product-detail/en/ams/AS5510-DWLT/AS5510-DWLTTR-ND/3464910.

[6] M. Khoo and C. Liu. A novel micromachined magnetic membrane microfluid pump. In *Proceedings of the 22nd Annual International Conference of the IEEE Engineering in Medicine and Biology Society (Cat. No.00CH37143)*, volume 3, pages 2394–2397 vol.3, July 2000.

[7] H. Chang, S. Hung, C. Tsou, W. Liu, C. Lai, and C. Jian. A novel electro-optical magnetic microsensor with reducing interference packaging. In *2007 8th International Conference on Electronic Packaging Technology*, pages 1–4, Aug 2007.

[8] ams AG. About AMS, November 2019.

[9] Rhodri Mansell, Tarun Vemulkar, Dorothée C. M. C. Petit, Yu Cheng, Jason Murphy, Maciej S. Lesniak, and Russell P. Cowburn. Magnetic particles with perpendicular anisotropy for mechanical cancer cell destruction. *Scientific Reports*, 2017.

[10] Eswaran P and Malarvizhi S. MEMS Capacitive Pressure Sensors: A Review on Recent Development and Prospective. *International Journal of Engineering and Technology*, 5(3):2734–2746, 2013.

[11] Pieter Zeeman. Over den invloed eener magnetisatie op den aard van het door een stof uitgezonden licht. *Versl. Kon. Akad. Wetensch. Amsterdam*, 5:181–184, 242–248, 1896.

[12] Pieter Zeeman. Over doubletten en tripletten in het spektrum, teweeggebracht door uitwendige magnetische krachten. *Versl. Kon. Akad. Wetensch. Amsterdam*, 6:13–18, 99–102, 260–262, 1897.

[13] J. M. D. Coey. *Magnetism and Magnetic Materials*. Cambridge University Press, 7th edition, 2010.

[14] E. C. Stoner and E. P. Wohlfarth. A mechanism of magnetic hysteresis in heterogeneous alloys. *Philosophical Transactions of the Royal Society of London A*, 240(826):599–642, 1948.

[15] M KonE, P Spibiik, P KolliIr, P SovAk, and T Reininger. Temperature Dependence of the Magnetization and of the other Physical Properties of Rapidly Quenched Amorphous COB Alloys. Technical Report 2, 1994.

[16] The Mathworks Inc. Matlab, 2019.

[17] David J. Griffiths. *Introduction to Electrodynamics*. Pearson, 4th edition, 1989.

[18] COMSOL Inc. COMSOL Multiphysics, November 2019.

[19] Cas van der Avoort. Calibration of the capacitive rectangular pressure sensor. Technical note nxp-tn-2015-0000, NXP Semiconductors, 2015.

[20] Wolfram Research, Inc. Mathematica, Version 12.0. ElementData function.

[21] A. Rinaldi, M.A. Correa-Duarte, V. Salgueirino-Maceira, S. Licoccia, E. Traversa, A.B. Dávila-Ibáñez, P. Peralta, and K. Sieradzki. Elastic properties of hard cobalt boride composite nanoparticles. *Acta Materialia*, 58(19):6474 – 6486, 2010.

[22] Tom Lichtenberg. Stabilising skyrmion bubbles in patterned nanostructures. Master's thesis, Eindhoven University of Technology, 3 2018.

[23] R. C. O'Handley and M. O. Sullivan. Magnetostriction of co80xtxb20 (t = fe, mn, cr, or v) glasses. *Journal of Applied Physics*, 52(3):1841–1843, 1981.

# A
# Study extensions

This appendix contains study extensions that are closely related to this work, but were left out because they either do not provide significant new insights or were performed after writing the main body of this thesis.

## A.1 Maxwell stress derivation

In this section the Maxwell stress is derived, following the book of Griffiths [17].

The Maxwell stress is derived from the Lorentz force, which has been rewritten to consist of only electromagnetic field components utilising three of the Maxwell equations. In this form the Lorentz force can be expressed in terms of the Maxwell stress tensor $\boldsymbol{T}$ and the Poynting vector $\boldsymbol{S}$.

$$\boldsymbol{T}_{ij} \equiv \epsilon_0(E_iE_j - \frac{1}{2}\delta_{ij}E^2) + \frac{1}{\mu_0}(B_iB_j - \frac{1}{2}\delta_{ij}B^2), \tag{A.1}$$

$$\boldsymbol{S} \equiv \frac{1}{\mu_0}(\boldsymbol{E} \times \boldsymbol{B}). \tag{A.2}$$

Here $\epsilon_0$ is the vacuum permittivity, $\boldsymbol{E}$ the electric field, $\delta_{ij}$ the Kronecker delta, $\mu_0$ the vacuum permeability and $\boldsymbol{B}$ the magnetic flux density. It should be noted that the Poynting vector $\boldsymbol{S}$ and electric field $\boldsymbol{E}$ are only included for the derivation, in the models they are both zero as there is no electric field.

The Lorentz force in integral form and its corresponding force density are given by:

$$\boldsymbol{F} = \int (\boldsymbol{E} + \boldsymbol{v} \times \boldsymbol{B})\rho \, dV, \tag{A.3}$$

$$\boldsymbol{f} = \rho\boldsymbol{E} + \boldsymbol{J} \times \boldsymbol{B}. \tag{A.4}$$

Here $\boldsymbol{v}$ denotes the velocity of a charge, $\rho$ the charge density, $V$ the volume and $\boldsymbol{J}$ the current density. The force density can be rewritten to include only electric and magnetic fields, using the following two Maxwell equations:

$$\boldsymbol{\nabla} \cdot \boldsymbol{E} = \frac{1}{\epsilon_0}\rho, \qquad \text{(Gauss's law)} \tag{A.5}$$

$$\boldsymbol{\nabla} \times \boldsymbol{B} = \mu_0\boldsymbol{J} + \mu_0\epsilon_0\frac{\partial \boldsymbol{E}}{\partial t}. \qquad \text{(Ampère's law)} \tag{A.6}$$

Here $\partial t$ denotes the time derivative. With these Maxwell equations the charge and current density can be replaced by their respective field representations:

$$\boldsymbol{f} = \epsilon_0(\boldsymbol{\nabla} \cdot \boldsymbol{E})\boldsymbol{E} + (\frac{1}{\mu_0}\boldsymbol{\nabla} \times \boldsymbol{B} - \epsilon_0\frac{\partial \boldsymbol{E}}{\partial t}) \times \boldsymbol{B}.$$

The cross product between the time derivative of $\boldsymbol{E}$ and $\boldsymbol{B}$ needs to be rewritten. This is done using the product rule of derivation and another Maxwell equation:

$$\frac{\partial}{\partial t}(\boldsymbol{E} \times \boldsymbol{B}) = (\frac{\partial \boldsymbol{E}}{\partial t} \times \boldsymbol{B}) + (\boldsymbol{E} \times \frac{\partial \boldsymbol{B}}{\partial t}), \tag{A.7}$$

$$\nabla \times \boldsymbol{E} = -\frac{\partial \boldsymbol{B}}{\partial t}. \qquad \text{(Faraday's law)} \tag{A.8}$$

Combining equation A.7 and A.8 results in:

$$\frac{\partial \boldsymbol{E}}{\partial t} \times \boldsymbol{B} = \frac{\partial}{\partial t}(\boldsymbol{E} \times \boldsymbol{B}) + \boldsymbol{E} \times (\boldsymbol{\nabla} \times \boldsymbol{E}).$$

Plugging this and the Poynting vector into the equation for the force density results in:

$$\boldsymbol{f} = \epsilon_0[(\boldsymbol{\nabla} \cdot \boldsymbol{E})\boldsymbol{E} - \boldsymbol{E} \times (\boldsymbol{\nabla} \times \boldsymbol{E})] - \frac{1}{\mu_0}[\boldsymbol{B} \times (\boldsymbol{\nabla} \times \boldsymbol{B})] - \epsilon_0\mu_0\frac{\partial \boldsymbol{S}}{\partial t}.$$

To make the equation more symmetrical the term $(\boldsymbol{\nabla} \cdot \boldsymbol{B})\boldsymbol{B}$ is added, which can be done since $\boldsymbol{\nabla} \cdot \boldsymbol{B} = 0$. The product rule, $\nabla(A^2) = 2(\boldsymbol{A} \cdot \boldsymbol{\nabla})\boldsymbol{A} + 2\boldsymbol{A} \times (\boldsymbol{\nabla} \times \boldsymbol{A})$, is also used for both $\boldsymbol{E}$ and $\boldsymbol{B}$ to get to the final result:

$$\begin{aligned}\boldsymbol{f} = \epsilon_0[(\boldsymbol{\nabla} \cdot \boldsymbol{E})\boldsymbol{E} + (\boldsymbol{E} \cdot \boldsymbol{\nabla})\boldsymbol{E}] + \frac{1}{\mu_0}[(\boldsymbol{\nabla} \cdot \boldsymbol{B})\boldsymbol{B} + (\boldsymbol{B} \cdot \boldsymbol{\nabla})\boldsymbol{B}] \\ - \frac{1}{2}\nabla(\epsilon_0 E^2 + \frac{1}{\mu_0}B^2) - \epsilon_0\mu_0\frac{\partial \boldsymbol{S}}{\partial t}.\end{aligned}$$

Looking at the j-th component of the divergence of the Maxwell stress tensors shows that it corresponds to the first terms of the force density:

$$\begin{aligned}(\boldsymbol{\nabla} \cdot \boldsymbol{T})_j = \epsilon_0[(\boldsymbol{\nabla} \cdot \boldsymbol{E})E_j + (\boldsymbol{E} \cdot \boldsymbol{\nabla})E_j - \frac{1}{2}\nabla_j E^2] \\ + \frac{1}{\mu_0}[(\boldsymbol{\nabla} \cdot \boldsymbol{B})B_j + (\boldsymbol{B} \cdot \boldsymbol{\nabla})B_j + \frac{1}{2}\nabla_j B^2].\end{aligned}$$

Substituting the Maxwell stress tensor into the equation of the force density gives the compact equation:

$$\boldsymbol{f} = \boldsymbol{\nabla} \cdot \boldsymbol{T} - \epsilon_0\mu_0\frac{\partial \boldsymbol{S}}{\partial t}. \tag{A.9}$$

For the total force the divergence theorem can be used to integrate over surface area, instead of volume:

$$\boldsymbol{F} = \oint \boldsymbol{T}\ dA - \epsilon_0\mu_0\frac{d}{dt}\int \boldsymbol{S}\ dV. \tag{A.10}$$

In this work, only the magnetic field is considered, which greatly reduces the equation as $\boldsymbol{E} = 0$ and $\boldsymbol{S} = 0$. The final result is the following compact equation:

$$\boldsymbol{F} = \oint \boldsymbol{T}\ dA. \tag{A.11}$$

## A.2 Magnetic field sweeps for non-perpendicular angles

The effective deflection behaviour at non-perpendicular field angles is further investigated using field strength sweeps, similar to Section 5.2.2. Figure A.1 shows an overview of several different angles. The behaviour is clearly different from the perpendicular magnetic field measurements and the effective deflection is greatly reduced. The effective deflection increases with external field strength and for the case of 75° it starts to saturate. This is in agreement with the torque picture of Section 4.1, where a maximum torque is expected at the saturation magnetisation for 75°. In Figure A.2 the effective deflection at different angles $\alpha$ is compared to the COMSOL magnetic film model and torque, which is re-scaled by a factor to be of similar order to the measured effective deflection. The overall behaviour of the effective deflection is well described by the model. The torque does not describe the system completely, as seen especially for 0°, where no torque is present. This is because the torque does not take the shape and deformation of the membrane into account, where there is no perfect 0° external field. Overall the COMSOL magnetic film model does well, but starts to grow stronger than the measurements at angles that approach 90°. This was also seen for the perpendicular field measurements, where the effective deflection of the COMSOL model was nearly twice as large as the measurements. It is not entirely clear why the model starts to deviate more, but it might be related to the difference in the peak- and drop-fields or slight tilting of the device, which were discussed in Section 5.2.2.

In short, the behaviour of the effective deflection at non-perpendicular fields is well described by the COMSOL model and torque description, with only small deviations.

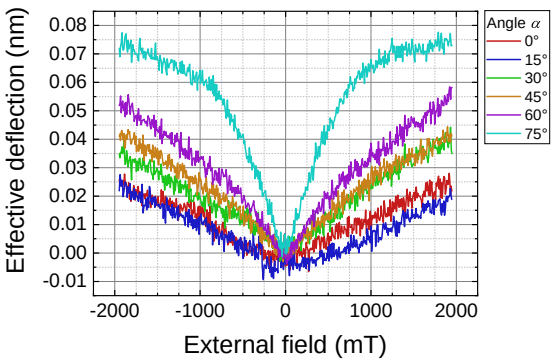


Figure A.1: External field sweeps for non-perpendicular fields. The effective deflection rises as the angle approaches 90°. At 75° the effective deflection starts to saturate after 1000 mT.

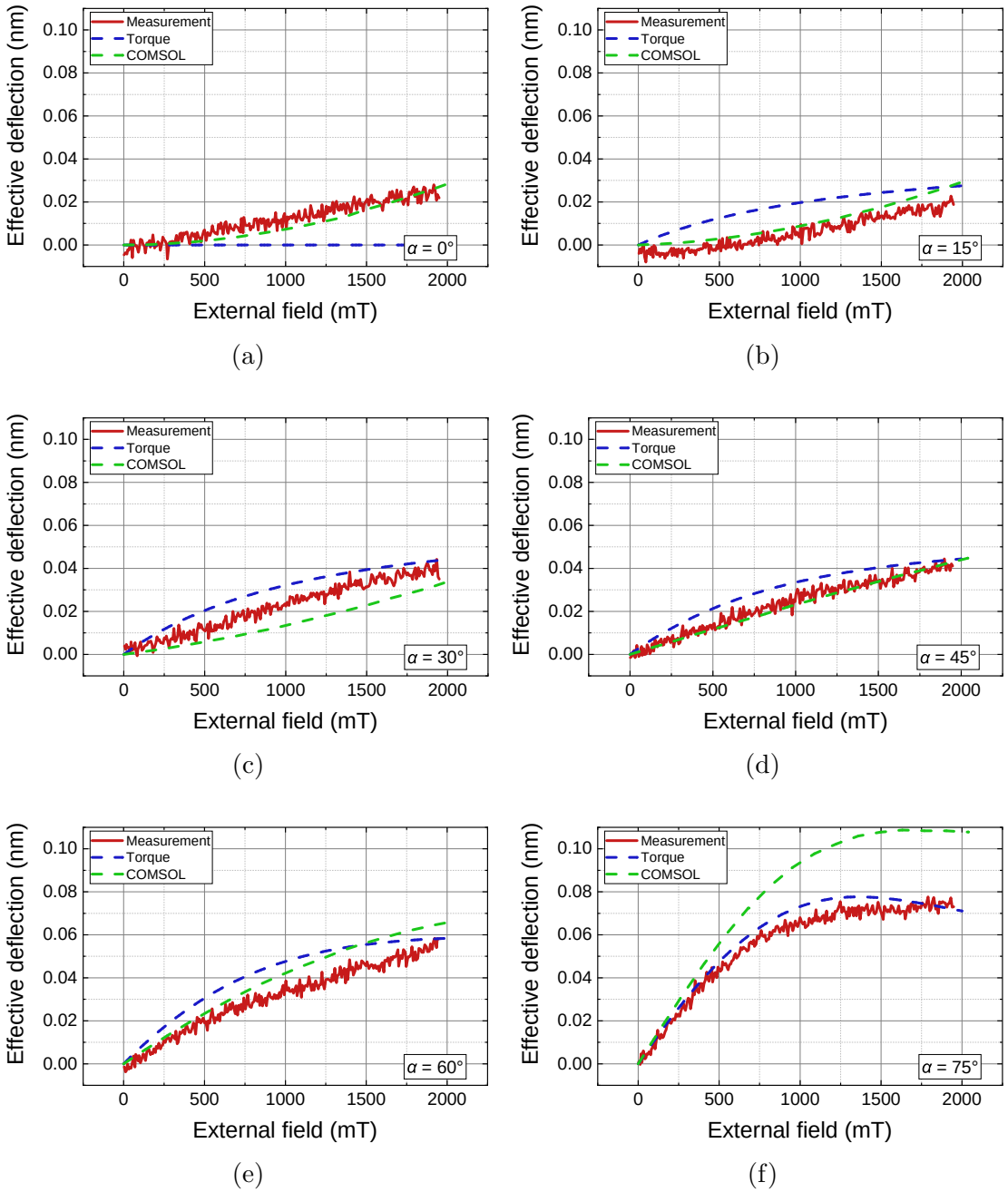


Figure A.2: Comparison of the external field sweep measurement with the COMSOL magnetic film model and re-scaled torque, for different external field angles $\alpha$. (a – f) External field angle $\alpha = 0° - 75°$.

## A.3 Stiffness and deflection extrapolation

The linear sensitivity and quadratic extrapolation of the optimal deflection from Section 5.3 depict a simplified view of the physics behind the deflection. This section provides another extrapolation, where instead of a linear sensitivity it is assumed that the stiffness of the membrane increases linearly. This is left to the appendix, as it was performed after writing the main thesis.

The same pressure output deviation measurements from Figure 5.8a are used to determine the stiffness of the membrane. This is shown in Figure A.3a, where the output deviation has been transformed to a deflection using the conversion factor and ambient pressure deflection, and the applied pressure has been transformed into a force using the area of the membrane. Note that the slope of this graph has the units m/N, i.e. the inverse of a stiffness or spring constant $K$. Figure A.3b shows the linearly extrapolated stiffness from the inverse slope of the data and model of Figure A.3a. In addition, it shows the stiffness directly calculated from the COMSOL pressure model. Note that the COMSOL model starts to grow more strongly than linear after a CoB thickness of 1 micron.

The magnetic deflection can be derived from the extrapolated stiffness in a similar manner to equation 5.1. The magnetic deflection is given by:

$$D = \frac{a \cdot t}{K(t)}, \tag{A.12}$$

where $a$ is a scaling constant such that the deflection corresponds to the measurements and has the units N/m, $t$ the CoB thickness, and $K(t)$ the thickness dependent stiffness. The derived and simulated magnetic deflections are shown in Figure A.3c.

For the linearly increasing stiffness the deflection increases slowly but indefinitely. However, in reality the stiffness should increase more strongly than linear, similar to what is seen in the COMSOL model. In this case the deflection is still limited by the stiffness of the CoB layer, but the turning point is likely higher than the 1 micron that was determined in Section 5.3.2.

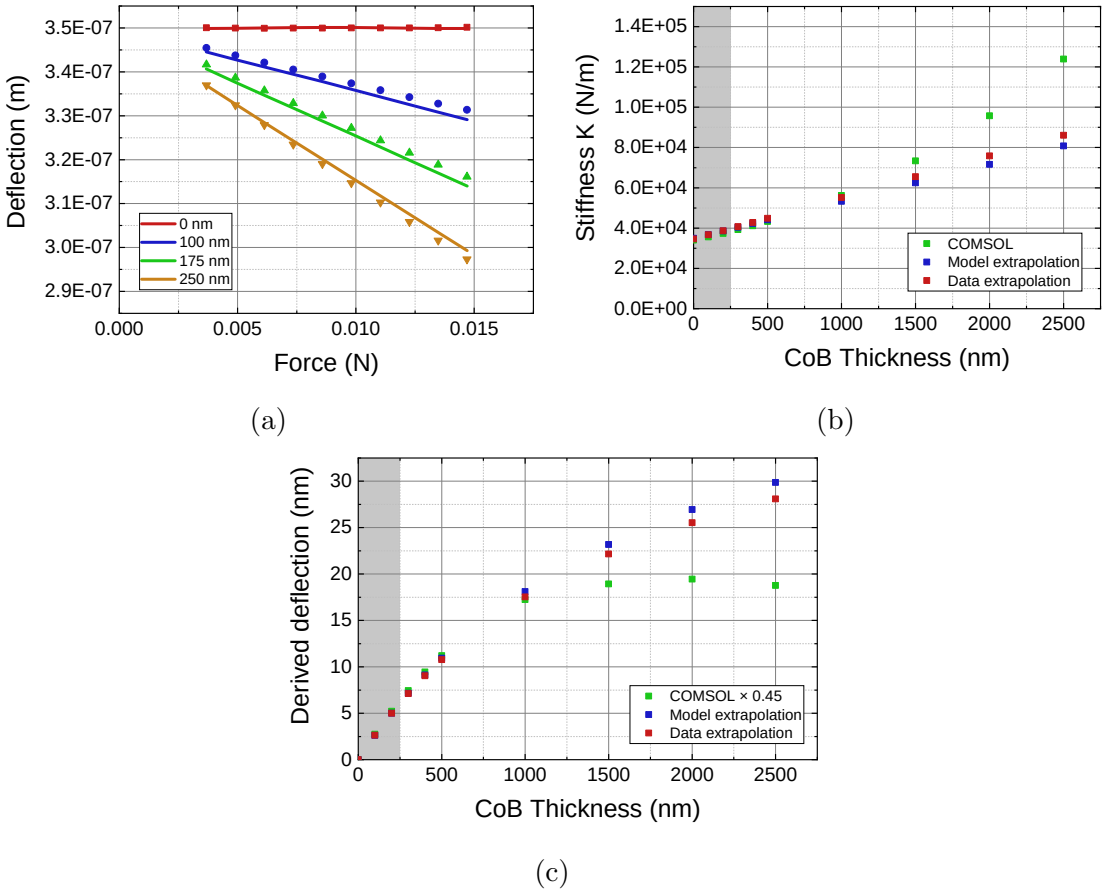


Figure A.3: Graphs depicting the extrapolated stiffness and deflection of the magnetic film. (a) The total deflection as function of applied force, for different CoB thicknesses. The markers denote measurements, while the lines consist of the corresponding modelling data. This is a simple conversion from Figure 5.8a. The grey areas denote the range in which measurements were done. (b) The derived and modelled stiffness of the membrane, as function of CoB thickness. The extrapolations are linear. The COMSOL model starts to grow more strongly than linear after 1 micron. (c) The stiffness derived deflection as function of CoB thickness. For a linear stiffness the deflection should increase indefinitely, however, the COMSOL model shows a optimum at 2 micron.

# B
# Model scripts

This appendix consists of MATLAB scripts that are used in modelling.

## B.1 Numerical magnetisation & torque simulation script

```
%% Initialisation

% Vacuum permeability
mu0 = 4 * pi * 10^(-7);
% CoB thickness
Thick = 100 * 10^(-9);
% Volume
V = 700 * 175 * Thick * (10^(-6))^2;

% Magnetisation saturation
Msat = 1.36 / mu0;
% External field
H = linspace(0.1,2/mu0,100);
% Angle in degrees
Alpha = [0 15 30 45 60 75 90];

%% Determine theta and the torque as function of H and alpha

% Symbol used in solver
syms x
% Initialise theta and torque solution arrays
Theta = zeros(size(Alpha,2),size(H,2));
t = zeros(size(Alpha,2),size(H,2));

for j = 1:size(Alpha,2)
    for i =1:size(H,2)
        % Numerically solve the equation for x (theta)
        T = vpasolve(sind(Alpha(j) - x) == Msat/H(i) * sind(x) *
            cosd(x), x);
        % Store theta
        Theta(j,i) = eval(T);
    end
```

```
32      % Determine the torque for specific theta
33      t(j,:) = mu0 * V * Msat^2 .* sind(Theta(j,:)) .* cosd(Theta(
            j,:));
34  end
```

## B.2 Magnetisation orientation lookup table script

```
1   clear all;
2   close all;
3
4   %% Initialisation
5
6   % Maximum field to apply, in ratio of anisotropy field
7   H0=2.0;
8   % Range of angles to sample from 0
9   Alpha0=360;
10
11  % Minimal field step (in anisotropy ratio)
12  Hmin = 0.01;
13  % Number of steps necessary for Hmin
14  Hsteps = ceil(H0/Hmin);
15
16  % Minimal alpha step (in degrees)
17  Amin = 0.05;
18  % Number of steps necessary for Amin
19  Asteps = ceil(361/Amin);
20  % Minimal theta step (in degrees)
21  Tmin = Amin;
22  % Number of steps necessary for Tmin
23  Tsteps = ceil(361/Tmin);
24
25  % Linearly spaced vector of H values
26  H=linspace(0,H0,Hsteps);
27  % Linearly spaced vector of Alpha values
28  Alpha=linspace(0,Alpha0,Asteps);
29  % Linearly spaced vector of H values
30  Theta = linspace(0,360,Tsteps);
31
32  % Initialisation of lookup table
33  I = zeros(Hsteps,Asteps);
34
35  %% Calculate optimal Theta for each Alpha and H combination
36  for i = 1:Hsteps
37      for j = 1:Asteps
38
39          % Determine the IP field component
40          H_IP = H(i)*cosd(Alpha(j));
41          % Determine the OOP field component
42          H_OOP = H(i)*sind(Alpha(j));
43
44          % Initialise the optimal energy as infinite
```

```
45          E0=inf;
46
47          for k = 1:Tsteps
48
49              % Calculate E as function of H, Alpha and Theta
50              E = sind(Theta(k)).^2 - 2*H_IP*cosd(Theta(k))...
51                  - 2*H_OOP*sind(Theta(k));
52
53              % If E is lower than the previous minimum set it
54              % as the new minimum and store Theta
55              if(E < E0)
56                  I(i,j)=Theta(k);
57                  E0=E;
58              end
59          end
60      end
61  end
62
63  %% Save Data in lookup table format
64  [Xout,Yout,Zout]=prepareSurfaceData(H,Alpha, I);
65  Data(:,1) = Xout;
66  Data(:,2) = Yout;
67  Data(:,3) = Zout;
68
69  fid = fopen('LookupTable.txt','wt');
70
71  for ii = 1:size(Data,1)
72      fprintf(fid,'%g\t',Data(ii,:));
73      fprintf(fid,'\n');
74  end
75
76  fclose(fid);
```